Treatment Planning for Immunomodulatory Radiopharmaceutical Therapy

By

Ian R. Marsh

A dissertation submitted in partial fulfillment of

the requirements for the degree of

Doctor of Philosophy

(Medical Physics)

at the

UNIVERSITY OF WISCONSIN-MADISON

2021

Date of final oral examination: 11/30/2021

The dissertation is approved by the following members of the Final Oral Committee:

Bryan P. Bednarz, Associate Professor, Medical Physics
Wesley S. Culberson, Assistant Professor, Medical Physics
Jonathan W. Engle, Assistant Professor, Medical Physics
Zachary S. Morris, MD, Associate Professor, Human Oncology
Jamey P. Weichert, Professor, Radiology

Abstract

Radiotherapy delivering immunomodulatory dose to localized disease has been shown to enhance tumor response to systemic and local immunotherapies. In metastatic disease, where conventional radiotherapy is limited, radiopharmaceutical therapy (RPT) with an alkylphosphocholine analog, ^{90}Y-NM600, can deliver immunomodulatory dose to all sites of disease. In preclinical models, cooperative therapeutic effect between immunotherapy and ^{90}Y-NM600 RPT delivering as little as 2 Gy to tumors has been observed. Work presented here describes the development and clinical translation of prospective theranostic dosimetry using pre-therapy imaging of ^{86}Y-NM600 for delivery of low-dose ^{90}Y-NM600 RPT.

Novel methodology for voxel and region level partial volume correction (PVC) of ^{86}Y-based ^{90}Y dosimetry was developed for this framework. Voxel-level PVC improved the recovery of ^{86}Y by up to 17.8% in small 0.5 ml lesions but demonstrated less utility in larger and more heterogeneous cases, necessitating region-based PVC. Region-level PVC increased dosimetry estimates by 45.6% ± 9.8% in preclinical tumors and 23-56% for 16-0.5 ml hot-spheres (10:1) in clinical phantom studies. In application to lung met dosimetry for canine patients, uncorrected dosimetry estimates were 38% ± 8.3% low compared to those with PVC.

Locoregional temporal coregistration approaches for multi-timepoint dosimetry were developed, automated, and validated in a deformable anthropomorphic phantom study. Target volume registration improved by 19.8-38.7% as measured by the dice similarity coefficient. With improved registration, the dosimetric impact of target volume definition was reduced by 30.6% to a difference of 4.4% ± 1.9% in D_{90} across all validation cases.

The developed framework was successfully implemented within a clinically reasonable timeframe (7.5 ± 2.3 days) for five canine patients. Low-dose ^{90}Y-NM600 at the ≥2 Gy level was administered as prescribed, with dosimetry indicating the potential for ≥4 Gy to all tumors. Notably, the constitution of canine patient immune function remained intact with little to no adverse events observed.

Acknowledgements

The road through which this thesis was written has been long and arduous. My greatest thanks are due to my advisor, Bryan Bednarz, whose support and enthusiasm for this work made it all possible. Your door has always been open, and you were always available to talk through crazy new ideas and help me understand unexpected results. Thank you for pushing me to reach my scientific and professional potential.

I would also like to thank the other members of my committee for providing their guidance, insight, and expertise these past six years: Wes Culberson, Jon Engle, Zach Morris, and Jamey Weichert.

To my collaborators, this work would not have been possible without the combined talents and perseverance of so many in medical physics, radiology, human oncology, and veterinary oncology. In particular, thank you to Joe Grudzinski, Reinier Hernandez, and Justin Jeffery for your advice and friendship these past six years. Thank you to The Ride and Paul Harari for recognizing the potential of this work. To all scientists in the Otto, Harari, Sondel, and Morris labs, your voracious appetite for mouse dosimetry helped populate a never ending to-do list during my time here and funded a great deal of this PhD. It has genuinely been a pleasure working each of you.

My time in graduate school at UW-Madison was made special by the people with whom I had the opportunity to spend it with. To my RED Lab mates, both past and present, your camaraderie has helped me through many difficult periods and your work ethic inspired me to test the boundaries of what I thought I was capable of. Thank you to my classmates and lifelong friends who helped me survive these past years with trips to badger games, sunsets at the terrace, ultimate frisbee games, and many late conversations fueled by Gumballhead and Spotted Cow. I'm honored to have been able to surround myself with so many high-character individuals who helped me to become a better man.

Thank you to my family, - Mom, Dad, and my sisters Erica and Kiara – your unconditional love and support through all these years of school have been invaluable. Much of this thesis is dedicated to my mother, Patty Marsh, who retired this year after working tirelessly for over 40 continuous years as a nurse for UW Health.

To my past teachers, Mr. Wallace, Mr. Kruger, Mrs. Howell, Mr. Strauss, and Mr. Guy, for supporting and encouraging a budding love affair with math, physics, chemistry, and all the other scientific black magics. Truly, the blame for many a late night spent at the library ultimately belongs with you. To the girl down the street, who convinced me I should probably try to go to college. To UW-Madison, for rejecting my application. To Shelly Lesher, my advisor at UW-La Crosse, who introduced me to the world of nuclear physics and helped me build the foundation upon which my research career rests. Thank you for making me who I am today.

"One of the most important ways to understand an imaging system is to understand it's artifacts and how to mitigate them."

The late Dr. Ed Jackson

Table of Contents

List of Figures

List of Tables

List of Abbreviations

AD – Absorbed dose

ADR – Absorbed dose rate

AUC – Area under curve

CT – Computed tomography

DVH – Dose volume histogram

EBRT – External beam radiotherapy

FBP – Filtered back projection

FoV – Frame of view

HU – Hounsfield unit

IT-IC – intratumoral immunocytokine (hu14.18-IL2)

LRR – Locoregional registration

MC – Monte Carlo

OSEM – Ordered subsets expectation maximization

PBMC – Peripheral blood mononuclear cells

PET – Positron emission tomography

PSF – Point Spread Function

PTV – Planning treatment volume

PVC – Partial volume correction

PVE – Partial volume effect

RAPID – Radiopharmaceutical Assessment Platform for Internal Dosimetry

ROI – Region of interest

RPT – Radiopharmaceutical therapy

Rx Dose – Prescription dose

SAF – Self-absorbed fraction

SPECT – Single photon emission computed tomography

SUV – Standard uptake value

TOF – Time of Flight

VPFX – (VUE Point FX, a 3D OSEM iterative reconstruction with TOF modeling)

VPHD – (VUE Point HD, a 3D OSEM iterative reconstruction for clinical PET)

VPHD-LR (VPHD with post-reconstruction PSF modeling by Lucy-Richardson deconvolution)

VPHD-S – (VPHD with a PSF modeling algorithm by GE, called SharpIR)

WBR – Whole body registration

Chapter 1

Introduction

Immunotherapies have emerged as an effective treatment approach for some patients with immunologically “hot” tumors, characterized by high T cell infiltration, but are less effective in against “cold” tumors that are largely devoid of immune cells (*1*). Concurrently, there has been a growing appreciation for the immunomodulatory role of radiotherapy to trigger a variety of mechanisms that increase tumor susceptibility to immune response (*2*,*3*). As such, considerable research efforts have been expended on the development of combination therapies leveraging the immunogenic capacity of radiation therapy to enhance the rate and depth of response to immunotherapies. Early results from these investigations are promising and more than 200 clinical trials have now been initiated to test combinations of immunotherapy and radiotherapy (*2*,*4*). Nearly all of these studies utilize external beam radiotherapy (EBRT), which is well suited to target individual tumor sites or regions.

In this context, focal EBRT is commonly intended to convert the targeted tumor into an "in situ vaccine", a nidus for presentation of tumor antigen for the purpose of priming a systemic anti-tumor immune response (*5*–*7*). However, preclinical and clinical studies have demonstrated that distant, untreated, tumors are unresponsive when localized immunotherapy and EBRT is delivered to primary disease sites (*8*,*9*). Early reports from clinical investigations of combinations of systemic immunotherapy and localized EBRT to primary tumors have also yet to demonstrate enhanced systemic response in the setting of metastatic disease (*10*). These results suggest that combination immunotherapies need to further address the suppressive immune microenvironment in distant tumors not targeted by EBRT. Yet, the risk for systemic lymphopenia from irradiation of large volumes in patients with widespread metastatic disease limits the utility of EBRT in this setting (*11*). Consequently, investigators at the University of Wisconsin-Madison have begun to investigate the use of radiopharmaceutical therapy (RPT) to deliver immunomodulatory dose to all tumor sites while sparing immune organs and circulating lymphocytes (*12*).

RPT is a systemic form of radiotherapy combining a tumor-selective vector with a therapeutic radioisotope. RPT has been used sparingly for nearly a century to treat cancer (*13*), but in recent years the oncology community has seen a renaissance of RPT applications and a growing number of RPT agents are being approved for clinical use (*14*,*15*). A recently developed alkylphosphocholine analog, NM600, developed by Weichert et al. has demonstrated selective uptake and retention in nearly all cancer models investigated, regardless of anatomic location (*16*–*19*). This includes syngeneic murine tumor models, companion canine tumors, human tumor lines, and patient derived xenografts. NM600 features a DOTA chelator that can be radiolabeled with a variety of metallic radionuclides for both diagnostic imaging (^{86}Y, ^{68}Ga, ^{64}Cu, ^{89}Zr) and therapeutic (^{90}Y, ^{177}Lu, ^{225}Ac) applications. This unique theranostic capacity of NM600 and select other RPT

agents can be exploited to optimize the delivery of immunomodulatory dose in combination with immunotherapy (*20*).

Over the past several years, the Bednarz lab has developed a patient-specific Monte Carlo internal dosimetry platform to facilitate the preclinical and clinical development of theranostic RPT-based cancer therapies with collaborators at UW-Madison and other partner institutions (*17*,*21–25*). With the pre-treatment acquisition of PET/CT or SPECT/CT scans of a theranostic analogue, it is possible to predict the biodistribution of an RPT agent in a given subject. This allows for not only better patient screening for RPT, but also prospective dosimetry to determine the biodistribution and timing of radiation dose delivered to tumor and normal organs per administered RPT activity.

This theranostic approach to RPT ensures that an appropriate amount of the RPT agent can be prescribed to limit toxicity and maximize treatment efficacy. In combination with immunotherapy, there appears to be a dose-dependent therapeutic window in which to achieve optimal response (*12*). Delivering too much absorbed dose may be unnecessary and could risk systemic immune suppression, whereas delivering too little absorbed dose may temper the immunogenic capacity of RPT. We hypothesize that the accurate patient- and tumor-specific administration of low-dose RPT will be critical for implementing this immune modulating strategy clinically.

1.1 Specific Aims

The purpose of this work is to establish a clinically translatable framework for theranostic dosimetry using pre-therapy PET-CT imaging of ^{86}Y-NM600 to facilitate the tumor-targeted delivery of low-dose ^{90}Y-NM600 RPT in combination with immunotherapy. Region and voxel level partial volume correction approaches will be developed to better account for the non-ideal PET imaging characteristics of ^{86}Y and better represent the 4D biodistribution of ^{86}Y-NM600. Here we will also develop a rigid locoregional registration approach paired with deformable image registration to improve the temporal coregistration of voxel level dose rate distributions. This framework is based on, and further develops, the well-validated Radiopharmaceutical Assessment Platform for Internal Dosimetry (RAPID) methodology previously established in the Bednarz Lab. Finally, the complete theranostic dosimetry workflow, including the developed methods, will be implemented for prospective dosimetry and treatment planning of low-dose ^{90}Y-NM600 RPT in combination with EBRT and immunotherapy in companion canine patients. The specific aims to be addressed are as follows:

1. *Develop a partial volume correction approach to improve quantitative ^{86}Y PET imaging of tumors for theranostic ^{86}Y/^{90}Y-NM600 dosimetry.*

2. *Develop an automated locoregionally rigid and deformable image registration approach to improve dose-rate accumulation and target definition in multi-timepoint theranostic ^{86}Y/^{90}Y-NM600 tumor dosimetry.*

3. *Evaluate the clinical impact of ^{86}Y-NM600 based treatment planning on immunomodulatory ^{90}Y-NM600 RPT in canine patients.*

1.2 Thesis Outline

To fulfill the aims of this project, this thesis is structured as follows:

- **Chapter 2** provides a comprehensive review of related literature as it pertains to the work presented in this thesis.
- **Chapter 3** describes the development and implementation of voxel- and ROI-level partial volume correction approaches in preclinical and clinical investigations. Within this context, the results from preclinical investigations into the pharmacokinetics and dosimetry of ^{86}Y/^{90}Y-NM600 in a variety of cancer models is presented.
- **Chapter 4** introduces a locoregional registration framework augmented with deformable image registration for tumor-specific multi-timepoint internal dosimetry. The impact of temporal coregistration and target definition on theranostic dosimetry is explored in an anthropomorphic deformable phantom.
- **Chapter 5** explores the implementation of the developed theranostic dosimetry workflow in companion canine patients as part of a comparative oncology trial investigating the trimodal combination of EBRT, ^{90}Y-NM600 RPT, and immunotherapy via IT-IC. The impact of the developed partial volume correction and registration approaches are presented herein.
- **Chapter 6** reviews the primary conclusions from this work and discusses potential future avenues of research.

Chapter 2

Personalized Dosimetry and Treatment Planning in Radiopharmaceutical Therapy

2.1 Radiopharmaceutical Therapy

The majority of cancer patient deaths are attributable to metastases (*26*) and patients presenting with distant metastases at diagnosis continue to face a grim prognosis (Table 1). Advances in the understanding of cancer biology have encouraged the development of molecularly targeted anticancer drugs with a particular focus on oncogenic drivers (*27*). However, clinical translation of targeted therapies has been hindered by the intrinsic evolutionary capacity of cancer cells to develop adaptive resistance under the selective pressure of targeted treatment (*28–30*). Investigators have thus directed focus on not only the combination of targeted therapies (*31*), but also the renewed development of molecularly targeted therapies delivering a more cytotoxic payload (*15*). The potent cytotoxic capacity of radiation has long been leveraged in cancer care with more than half of patients receiving radiotherapy either alone or in combination with other

modalities (*32*). The incorporation of radionuclides in molecularly targeted agents has been of particular interest with in vitro studies demonstrating cytotoxic effects 85-300 times that of comparable chemotherapeutic agents, based on a molar concentration (*33*).

Table 1: 5-year survival by staging at diagnosis†

Site	Localized	Distant
Lung and bronchus	70%	9%
Colorectal	93%	18%
Pancreas	49%	4%
Breast	99%	32%
Prostate	100%	40%
Melanoma	99%	38%

†SEER.cancer.gov, modeled rate for 2018

Radiopharmaceutical therapy (RPT) is a mode of radiation therapy defined as the delivery of therapeutic radionuclides to tumor-associated targets (*34*). This is most commonly achieved via radiolabeling with a tumor-targeting molecular agent but can also include the selective delivery of a radionuclides encapsulated in micro- or nano-particles. In contrast to more common radiotherapy approaches (e.g. external beam) where radiation is administered from outside the body, RPT delivers cytotoxic radiation directly to cancer cells or their microenvironment following selective accumulation of the RPT agent. Radiation-induced cytotoxicity is well understood from decades of EBRT use and is less sensitive to adaptive changes in cancer biology than that of targeted therapies (*35*). Without the need for advanced imaging and manual targeting of lesions sites to deliver radiation, RPT is a particularly capable treatment approach in the setting of widespread metastatic disease. Notably, when used in combination with other treatment modalities, RPT has demonstrated efficacy with minimal toxicity compared to nearly all other systemic treatment options (*36*).

The terms targeted radionuclide therapy (TRT), molecularly targeted radionuclide therapy (MTRT), and molecular radiotherapy (MRT) have similarly been used to describe radionuclide therapies. Henceforth, RPT will be used in this thesis.

The effectiveness of an RPT agent relies not only on tumor-specific molecular targeting mechanisms, but also the appropriate choice of radionuclide depending on tumor size, radiosensitivity, and heterogeneity. The primary physical characteristics of a therapeutic radionuclide relevant to RPT are the radioactive half-life, the type of emitted particles, and their range in tissue. The half-life of the radionuclide should be tailored to the pharmacokinetics of the agent. A short lived radionuclide paired with an agent that requires relatively long time to localize to tumors will achieve poor results as the majority of energy is released before the tumor-selective phase of biodistribution is reached. Similarly, too long of a radioactive half-life is disadvantageous as it necessitates excessive amounts of activity to achieve significant accumulation of dose before rapidly clearing and results in logistical challenges related to radiation safety and disposal of material waste. Of the radionuclides used in RPT agents that are commercially available or in late-stage stage development, all are either β-particle or α-particle emitters (*37*,*38*).

β-particles are electrons emitted from the nucleus that typically have a long range (1-5 mm, mean) over which they deposit energy at a relatively low density (~0.2 keV/μm) (*39*). β-emitting radionuclides are considered effective in the treatment of medium to large tumors with the far reaching tracks of emitted β-particles exposing neighboring cells in the tumor microenvironment to radiation (*39*,*40*). This cross-fire effect is essential for overcoming heterogeneous uptake in tumors (*41–43*) and effectively modulating the suppressive tumor immune microenvironment (*44–46*). The downside of the long reach of β-emitting particles is in increased cross-irradiation of

adjacent healthy tissues and poor self-absorption of radiation at sites of micro-metastatic disease where the pathlength of the β exceeds that of the size of the small cluster of cells.

β-emitters are the most common type of radionuclide in widely used RPT agents with ^{131}I ($t_{1/2}$ = 8.0 d), ^{90}Y ($t_{1/2}$ = 64.1 h), and ^{177}Lu ($t_{1/2}$ = 6.6 d) being employed the most frequently over the past 40 years (*37*). ^{131}I is by far the most utilized of the β-emitting radionuclides with a long history in the treatment of thyroid cancers and disorders (*47*,*48*). More recently, there has been significant success in the clinical translation of ^{177}Lu-DOTATATE for neuroendocrine tumors (*49*), ^{177}Lu labeled to prostate specific membrane antigen (PSMA) peptides in metastatic castration resistant prostate cancer (*50*), as well as ^{90}Y and ^{131}I labeled anti-CD20 monoclonal antibodies in follicular B-cell non-Hodgkin lymphoma (*51*). Radioembolization with ^{90}Y encapsulated in microspheres (^{90}Y-SIRT) for the treatment of hepatic metastases has also experienced substantial clinical utility (*52–54*). Notably, the emission of prompt gammas alongside β's in radioactive decay of ^{131}I (E_γ = 364 keV (81.7%)) and ^{177}Lu (E_γ = 113 keV (6.6%), 208 keV (11%)) allows for direct single photon emission computed tomography (SPECT) imaging of the RPT agents in vivo.

The development of RPT agents utilizing α-particle and Auger electron emitting radionuclides, taking advantage of shorter range and substantially higher LET radiation, is also a promising and rapidly evolving area of research in the RPT space (*55–58*). However, investigation and discussion of these radionuclides is beyond the scope of this thesis.

2.1.1 Theranostics

The term theranostics is a portmanteau describing the systemic integration of targeted therapeutics (thera-) with analogue diagnostic (-nostics) that has fueled a renaissance in the field of nuclear medicine and RPT over the past two decades (*14*,*59*). In application to RPT, this approach describes the use of a representative diagnostic biomarker, typically imaged with

SPECT-CT or PET-CT, to screen patients for a favorable therapeutic index (ratio of tumor to background and normal tissue) and facilitate the patient-specific delivery of the therapeutic agent. This personalized approach to the administration of RPT and other targeted therapies has coincided with the rise of precision medicine in oncology (*60*). The most apparent candidates for theranostic applications of RPT involve the pairing of biomechanically identical radioisotopes ^{123}I/^{124}I/^{131}I (*61*), ^{68}Ga/^{177}Lu (*62*), and ^{86}Y/^{90}Y (*63*). Another approach is to use a trace amount of a SPECT imaging capable RPT agent (e.g. ^{131}I and ^{177}Lu) prior to administration of the full course of RPT. In cases where RPT agents are administered in a series of fractions, retrospective dosimetry based on imaging of the first RPT cycle may be used to modulate subsequent fractions of RPT. Of particular interest in the work presented in this thesis is the theranostic pairing of ^{86}Y for diagnostic PET imaging and ^{90}Y for RPT (Table 2).

Table 2: Primary decay information for the yttrium isotopes ^{86}Y and ^{90}Y (*64*,*65*)

Radioisotope	$t_{1/2}$	Mode of decay†	$E_{\beta(max)}$ (keV)†	R_β max (mm)	E_γ (keV) †
^{90}Y	64.1 h	β^- (100)	2290 (100)	11.0	-
^{86}Y	14.7 h	EC (67) β^+ (33)	1033 (1.9) 1162 (1.3) 1221 (11.9) 1545 (5.6) 1736 (1.7) 1988 (3.6) 3114 (2.0)	4.4 5.0 5.6 7.1 8.3 9.7 15.0	443 (16.9) 515 (4.9) 581 (4.8) 628 (32.6) 646 (9.2) 703 (15.4) 778 (22.4) 1077 (82.5) 1153 (30.5) 1854 (17.2) 1921 (20.8)

†intensity of emission shown as a percentage in parenthesis

^{90}Y is an ideal radionuclide for RPT with a half-life of 64.1 h that matches up well with the pharmacokinetics of a wide variety of molecularly targeted agents (*66*). Additionally, nearly 100% of ^{90}Y decays via β-emission to the stable 0^+ state of ^{89}Zr with a maximum energy of 2.29 MeV (mean, 0.94 MeV) and maximum range in tissue of 11.0 mm (mean, 4.0 mm). Production of ^{90}Y is accomplished with a ^{90}Sr/^{90}Y generator or ^{90}Zr(n,p)^{90}Y and ^{89}Y(n,γ)^{90}Y reactions (*67–69*). ^{90}Y

also occasionally emits a positron (β^+) via internal pair production that can be imaged with positron emission tomography (PET), the branching ratio is so small (3.186×10^{-5}) that activities in excess of 300 MBq are necessary, limiting its potential utility to ^{90}Y-SIRT cases (*70*,*71*).

^{86}Y presents a comparatively complex decay scheme with a wide range of β^+ energies emitted (1.04-3.11 MeV, max) and an overall positron branching ratio of 31.9%. Decay of ^{86}Y also entails the emission of more than 11 prompt γ's ranging in energy between 0.4-1.92 MeV. PET imaging of ^{86}Y is made challenging by the abundance of prompt γ's emitted within the typical energy discrimination window (400-650 keV) intended to capture 511 keV annihilation photons. The high energy of the β^+ emitted from ^{86}Y also means there is a greater chance that annihilation occurs at a non-negligible energy and the coincident pair of 511 keV photons will be emitted at <180°, introducing further uncertainty in PET imaging (*72*). Production of ^{86}Y is performed with a cyclotron through proton bombardment (7-14 MeV) of $^{86}SrCO_3$ (>96.4% isotope purity) targets to facilitate ^{86}Sr(p,n)^{86}Y reactions. The high cost of enriched $^{86}SrCO_3$ targets necessitates recycling of the target material, an area of research where collaborators at the University of Wisconsin-Madison have pioneered novel separation strategies (*73*). With a short half-life of 14.7 h, the logistics behind the production, labeling, and use of ^{86}Y in imaging studies necessitates considerable planning and preparation. Notably, ^{89}Zr ($t_{1/2}$ = 78.4 h, $E_{\beta+(max)}$ = 902 keV (22.7%)) has been suggested as an alternative PET-avid radionuclide for use in diagnostic analogs of ^{90}Y labeled to monoclonal antibodies (*74*).

2.1.2 Alkylphosphocholine analogs

Early observations of the high concentration of alkylphospholipids in neoplastic cells relative to normal cells (*75*) led to the development of alkylphosphocholine (APC) analogs (*76*,*77*). The semi-selective accumulation and retention of these small molecule APCs is not mediated by

a specific receptor, but through the 6–10 times higher abundance of lipid rafts on the plasma membrane of cancer cells. The broad spectrum tumor-targeting capacity of APC analogs has been demonstrated in a variety of cancers with little regard for anatomic location or tumor type (*78–80*). Clearance of APC analogs occurs through hepatobiliary metabolism with considerable accumulation in the liver.

The APC analog 18-(p-iodophenyl)octadecyl phosphocholine (NM404 or CLR1404) and it's radioiodinated variants have been thoroughly investigated in the preclinical setting for diagnostic (^{124}I-NM404 or CLR 124) and RPT (^{125}I-NM404 or CLR 125 and ^{131}I-NM404 or CLR 131) applications (*23–25*,*81*,*82*). Clinical trial investigations of ^{131}I-NM404 in a spectrum of hematological and solid tumors are ongoing (NCT03478462, NCT04105543, NCT02952508, NCT02952508, and NCT01495663). Peak tumor uptake of NM404 is achieved at 72-96 h after injection and followed by prolonged retention. Notably, ^{131}I ($t_{1/2}$ = 8 d) labeled NM404 has exhibited minimal clearance from the blood when imaged out to 14 days after injection, indicating a long blood half-life (*83*).

The latest generation APC analog, 2-(trimethylammonio) ethyl(18-(4-(2-(4,7,10-tris(carboxymethyl)-1,4,7,10-tetraazacyclododecan-1-yl)acetamido)phenyl)octadecyl) phosphate (NM600), features a DOTA chelator for labeling with a variety of radiometals for diagnostic (^{86}Y, ^{68}Ga, ^{64}Cu, ^{89}Zr) and therapeutic (^{90}Y, ^{177}Lu, ^{225}Ac) applications. Preclinical investigations of NM600 affirmed the broad spectrum tumor-targeting capacity observed in other APC analogs (*17*). Additionally, ^{90}Y-NM600 has demonstrated synergy with a variety of immunotherapeutic approaches when used in a low-dose capacity (*12*,*18*,*19*,*84*). Compared to NM404, the biodistribution of NM600 and localization to tumors occurs more rapidly with peak uptake achieved as early as 24 h after injection.

2.2 Personalized Internal Dosimetry

Despite over 40 years of experience with external beam radiotherapy demonstrating patient-specific absorbed dose as an excellent predictor of treatment efficacy and toxicity, dosimetry guided delivery of RPT has not been widely adopted (*85*,*86*). This is due, in part, because the field has long employed a dosimetry methodology more appropriate for risk analysis in populations taking part in nuclear medicine imaging studies than the individual assessment of efficacy and toxicity (*87*). Early attempts to relate dosimetry to outcome were not successful and, as a result, RPT has followed a prescription approach akin to chemotherapy with fixed or body weight scaled dosing based on phase I dose escalation trials in a limited number of patients. As the popularity of theranostics and RPT agents has grown, recent clinical investigations have placed more focus on individual patient's absorbed dose and its relationship with toxicity and treatment response, providing strong evidence for the use of personalized dosimetry in RPT (*88*).

Absorbed dose is a well-defined physical quantity in radiation therapy defined as the energy absorbed per unit mass of tissue and is not to be confused with pharmacological dose. The extent to which dose delivered by RPT affects tumors and normal tissues depends on the localization of the agent in tumors and the duration of uptake. In the context of chemotherapeutics, the dosimetry process is akin to performing pharmacodynamic analysis in a patient in real time. In contrast to EBRT where a dose distribution is produced to conform to a given target volume, the underlying biodistribution of the agent and localization to the target region remains fixed, in a sense, and can only be scaled by the amount of administered activity. Dosimetry guided RPT may be performed using either a prospective or retrospective methodology.

In the prospective approach a diagnostic analog to the RPT agent, or a trace amount of the RPT agent itself, is administered and imaged prior to therapy. In fractionated RPT, retrospective

dosimetry based on imaging following administration of the first cycle may be used to escalate or reduce subsequent fractions of RPT. One key assumption underlying the prospective dosimetry approach is that the receptor mechanism through which molecular targeting is achieved is not modified by the delivery of the trace amount of RPT or it's diagnostic analog. Where trace amounts of the RPT agent are administered for pre-therapy imaging, the low-dose received by the targets may modulate the receptor mechanism or tumor microenvironment in manner that alters the biodistribution of subsequent fractions.

The tools available for performing dosimetry in nuclear medicine in either the prospective or retrospective capacity have evolved over time. The following section will describe the two fundamental methods through which these tools approach internal dosimetry.

2.2.1 The MIRD method

Early on, it was the risk assessment of diagnostic agents in nuclear medicine that motivated development of dosimetry tools. These early approaches, utilizing the colloquially termed medical internal radiation dose (MIRD) method (*89*), are characterized by the use of standardized phantoms to represent various categories of patients (e.g. 70 kg adult, 19 kg 5-yr-old, 3.4 kg newborn, etc.) (*90*). Monte Carlo modeling of reference phantoms is then used to pre-populate the cross- and self-irradiation factors (S-values) of organs in relation to each other for all radionuclides used in RPT:

$$D(r_T) = \sum_{r_S} \tilde{A}(r_S)\ S(r_T \leftarrow r_S) \qquad 1$$

Where r_T is the target region, r_S is the source region, $\tilde{A}(r_S)$ is the time integrated activity (i.e. total number of decays over time), and S is the S-value. The MIRD method has also been referred to as the absorbed fraction method. When compared to patient-specific MC, dosimetric errors of 20-60% have been observed due to deviations in organ anatomy (*91*). The sophistication of reference

phantoms has advanced over the years (*92*,*93*), but they remain impersonal and less than ideal in the context of patient-specific tumor dosimetry. Notably, because reference phantoms represent typical healthy patient anatomy, tumor dosimetry must be modeled separately using sphere-based models, independent of the context of surrounding tissue and anatomy. Sphere models have shown to systematically underestimate tumor dosimetry by 2-31% (*94*).

The utility of the MIRD method and reference phantoms remains significant in the emerging field of multi-scale dosimetry where the resolution of whole-body imaging is too low to characterize the radiation-induced cytotoxic effects of short range emitters. A macro-to-micro approach to α-particle (range of 50-100 μm) dosimetry has been investigated for bone marrow (*95*) and kidney models (*96*). For Auger electron emitters with an even shorter sub-cellular range (1-1000 nm), single-cell dosimetry approaches should be utilized to understand how the localization of the RPT agent in cells and around the nucleus effect their therapeutic potential (*97–99*). However, it is unclear what role, if any, microdosimetric cellular approaches can play in patient-specific RPT dosimetry.

2.2.2 Voxelwise dosimetry

Voxelwise dosimetry approaches, using a patient's own 3D PET/SPECT and CT images to model the distribution of dose at each timepoint, have become more popular in recent years (Table 3). Naturally, using patient imaging as the basis for dosimetry allows for more dosimetric accuracy than the MIRD method because it accounts for heterogeneous uptake and retention in normal tissues and tumors, tissue density, and the in vivo composition of patient anatomy with respect to tumors. There are two modeling approaches through which a 3D absorbed dose rate distribution may be calculated from the 3D activity distribution provided by PET/SPECT imaging: direct Monte Carlo and convolution.

Table 3: FDA-approved commercial software packages for internal dosimetry as of February 2020 (*100*)

Software	Date of approval	Dosimetry method
OLINDA/EXM 1.0	2004	MIRD
Hermes OLINDA/EXM 2.0	2017	MIRD
MIM SurePlan MRT	2019	Voxelwise, convolution
DOSIsoft PLANET Dose	2019	Voxelwise, convolution
Hermes Voxel Dosimetry	2019	Voxelwise, Monte Carlo

Direct Monte Carlo methods for solving the radiation transport equation have long been held as the gold standard for dosimetry. It is a statistical method through which a large number of individual particles are simulated based on random sampling of the well-known probability distributions describing physical decay properties of a radionuclide. The energy released from a particle is then tracked as it traverses through voxels of varying density and material composition in the patient anatomy, defined by the CT image, until its energy falls below a set energy threshold. The relative weight of the energy imparted by particles simulated from a given source voxel is defined based on the magnitude of the PET-based activity concentration. There are several Monte Carlo codes available for radiation transport in medical physics, namely Geant4 (*101*), MCNP (*102*), and EGS (*103*). A number of research groups have leveraged Monte Carlo methods to develop internal dosimetry toolkits, including 3D-RD (*104*), SIMDOS (*105*), DOSING (*106*), SCMS (*107*), MINERVA (*108*), OEDIPE (*109*), DPM (*110*), RAYDose (*111*), JADA (*112*), simDOSE (*113*), VIDA (*114*), and RAPID (*21*).

Convolution based approaches rely on the use of dose point kernels (DPK) representing the radial dose distribution resulting from the decay of a radionuclide at a point. The DPKs for a wide range of radionuclides relevant to RPT have been reported over the years (*115*) and can be presented in terms of Gy/(Bq/ml). Dosimetry with DPKs are performed by convolving the isotropic DPK with the PET-imaged activity distribution (*116*). In order to account for tissue

heterogeneities, the DPK can be scaled linearly based on the difference in density between the medium and water (*117*). Notably, the concept of collapsed cone convolution superposition, accounting for anisotropically heterogeneous media, has been applied for more accurate application of DPKs (*118*,*119*). To better represent voxel-defined distributions of activity, DPKs can be used to generate so called voxel s-values (VSV), which can then be easily implemented with convolution based algorithms. A number of research groups have developed VSV-based toolkits for RPT dosimetry applications (*120–124*). In cases where the range of the particles emitted by the radionuclide are small relative to the resolution of the voxel, VSV amount to a single-voxel local deposition factor (*125*). Fast fourier transforms may be used to rapidly convolve VSV in a voxelized geometry but rely on the assumption that the DPK is spatially invariant. In applications of VSV to dosimetry for ^{90}Y microspheres, dose differences between VSV and Monte Carlo can be up to 476% in low-density regions (*126*).

Notably, the resolution of voxelwise dosimetry approaches is fundamentally limited by the resolution of the imaging modalities used. While CT imaging is capable of achieving voxel-level resolution of approximately 1 mm, the spatial resolution of PET imaging with commercial clinical scanners is around 4 mm (*127*). Additionally, it is important to note that the dosimetric accuracy of individual voxels is further limited by spill in and spill out of observed activity from adjacent regions (e.g. partial volume effects) (*128*).

2.2.3 Temporal coregistration in multi-timepoint internal dosimetry

In part due to the long term use of the MIRD methodology and popularity of mean dose as a dosimetric endpoint in nuclear medicine, the impact of temporal coregistration on voxel-level dosimetry for multi-timepoint imaging studies has not been thoroughly investigated. For multi-timepoint internal dosimetry, a dose rate map is generated from the scans at each timepoint. The

cumulative absorbed dose in tissue is then calculated by integrating the time-dose-rate curve over time. In order to perform this final step at a voxel-level, the dose rate distributions at each timepoint must be coregistered prior to integration. Typically, molecular imaging studies do not employ immobilization devices, ubiquitous in conventional radiotherapy environments (*129–131*), to facilitate consistent patient positioning between scans, making registration of multiple scans all the more challenging (*100*). Access to advanced registration strategies is seen as one of the primary obstacles to the adoption of high quality RPT dosimetry in the clinic (*132*). To our knowledge, there are currently no

In recent years, multi-timepoint dosimetry investigations have utilized a combination of either whole-body or piecewise rigid registration followed by deformable image registration (*110*,*133*,*134*). These methods are either applied at the whole-body level or piecewise with a focus on accurate locoregional registration of each target. The concept of region-specific piecewise registration for analysis of biological images was initially proposed by Pitiot et al (*135*). Edwin et al reported that the application of B-spline based DIR in a computational phantom study improved the difference in liver mean dose estimates for ^{111}In Zevalin from -7.28% to -0.23%, based on a reference target volume definition (*136*). For smaller target lesions, however, temporal coregistration can be more difficult. Jackson et al. reported a registration success rate of 93.1-98.3% for normal tissues (e.g. kidney, liver, spleen), but only 74.1-86.9% for tumors and salivary glands (*134*).

2.2.4 Growing evidence for radiation dose-response in RPT

The cultivation of literature demonstrating a clear relationship between absorbed dose delivered by RPT and toxicity or response has been a long and arduous journey for the field of nuclear medicine. This has been in part due to the long term use of imaging and dosimetry

approaches in clinical investigations that are inaccurate (e.g. planar imaging), incomplete (e.g. not enough timepoints), or more catered to diagnostic risk assessment than therapeutic evaluation (only blood sampling performed). Technological advancements in emission imaging over the years, the emergence of new promising RPT agents, and a renewed focus on dosimetric analysis in the field have begun to remedy this situation.

A comprehensive review of the evidence supporting personalized dosimetry in nuclear medicine was performed by Strigari et al in 2014 (*88*), which that found a dose-response relationship was observed in 48 of 79 (60%) clinical trial studies where dosimetry was performed. This past year, a brief update to this literature review was provided by Graves and Hobbs (*100*) that found that 82% of clinical dosimetry investigations showed significant dose response relationships with respect to toxicity or treatment response.

In the treatment of neuroendocrine tumors with peptide receptor radionuclide therapy (PRRT), tumor dose-response relationships have been demonstrated for both ^{177}Lu-DOTATATE and ^{90}Y-DOTATOC (*137–139*). In both cases, personalized dosimetry has been shown to be important for reducing kidney and marrow toxicity. ^{177}Lu labeled PSMA-617 has also demonstrated tumor dose-response relationships in patients with metastatic prostate cancer (*140*). Additionally, EANM now requires personalized dosimetry in the development of ^{177}Lu labeled PSMA agents (*141*) because of the demonstrated potential for pre-therapeutic dosimetry toxicity to the kidneys, lacrimal glands, and salivary glands (*142–145*). Personalized dosimetry for patients undergoing therapeutic nuclear medicine studies is also mandated by European council directive 2013/59/EURATOM. In the US, the FDA currently only mandates dosimetry during clinical trials.

2.3 Quantitative Nuclear Imaging for RPT Dosimetry

Photon emissions from RPT agents or their theranostic analogs are a vital source of information for assessing the biodistribution of an agent and a prerequisite for performing theranostic dosimetry. In contrast to radiographic imaging modalities that rely on the projection of x-rays through a patient's anatomy, imaging in nuclear medicine relies on the principle of emission imaging where γ-rays and x-rays emitted from a radiopharmaceutical, in vivo, are measured within scintillation detectors. A wide range of photon energies (70-400 keV) may be imaged with planar or 3D SPECT, but the optimal photon energy for imaging ranges between 100-200 keV. For radionuclides that decay via positron-emission, PET imaging may be utilized. While PET imaging is considered natively quantitative with voxels reconstructed in units of Bq/ml, quantitative imaging with SPECT is more challenging. The default unit for reconstructed SPECT images is in terms of 'counts' and is typically not normalized for voxel volume, scan duration, and other essential imaging properties. Yet, the development of standards for quantitative SPECT imaging methods (*146–148*) and innovation in SPECT camera design remains an active area of research due to the popularity of ^{177}Lu and ^{131}I based therapies (*134*,*149*). While SPECT imaging is a necessary tool for the implementation of many popular theranostic RPT agents, the focus of quantitative imaging work in this thesis lies entirely in the domain of quantitative PET imaging.

2.3.1 Positron emission tomography with non-pure positron emitting radionuclides

PET imaging plays an important role in clinical oncology, allowing for non-invasive and quantitative assessment of regional tissue function, *in vivo* (*150*). PET imaging differs from SPECT in that it is specifically designed to detect the coincident pair of 511 keV photons (emitted 180° apart) that result from the annihilation of an emitted positron with a nearby electron (also

called a negatron). SPECT systems are similarly able to image these 511 keV photons, but the detection efficiency at this higher energy is lower and does not take full advantage of the localization potential of simultaneous detection of the pair of photons. SPECT imaging systems are typically designed with one or two gamma camera panels that rotate around a patient for tomographic imaging. In contrast, PET scanners utilize a ring of detectors to maximize the potential detection of coincident photons. Notably, whole-body PET systems constructed from a cylindrical arrangement of detectors, a design traditionally limited to preclinical systems, have recently come to market with the potential to achieve significantly greater image quality than ring-based systems (*151*).

For non-pure positron emitters commonly employed in the theranostic approach to dosimetry, such as ^{86}Y, quantitative imaging with PET is more challenging. The localization of the source of a given emission from these radionuclides is confounded by several of factors.

The range through which a positron may travel from its point of origin is a factor that fundamentally limits achievable resolution of a tracer (*152*,*153*). The positrons emitted by ^{86}Y range between 1.03-3.11 MeV with a maximum range of 15.0 mm (mean 6.9 mm). Comparatively, the maximum range of positrons emitted by ^{18}F is 2.4 mm (mean 0.6 mm). The impact of positron range on resolution has been characterized in high resolution PET scanners for preclinical and brain imaging (*154*,*155*). Although, the loss in resolution due to positron range is largely drowned out by other factors in clinical systems with a resolution around 4 mm (*127*). Given recent advances in whole-body PET, however, it is likely that positron range modeling will soon become more applicable in the clinical setting. Notably, large positron ranges can also result in particles escaping the body and annihilating in air, creating so called ‘shine-through’ or ‘ghost’ signal appearing outside the body. This effect has been observed in air cavities of patients imaged with ^{124}I (*156*).

Another factor impacting quantitative PET imaging is simultaneous emission of γ-rays and positrons during decay. When emitted at energies equal to or greater than the energy window defined for measurement of 511 keV (350–650 keV), prompt gammas can produce spurious coincidences. Prompt gammas that are emitted at energies higher than 650 keV also can scatter into lower energies and cause further spurious coincidence measurements. In the case of ^{86}Y, all positron decay branches arrive at an excited state of ^{86}Sr with a resulting cascade of prompt gamma emissions. Prompt gammas range in energy from 0.4-1.92 MeV. Note that prompt gammas above 1.022 MeV may interact via pair production with the electromagnetic field of a nearby charged particle, creating and negatron-positron pair, resulting in yet another pair of coincident 511 keV photons.

2.4 Compensating for Partial Volume Effects

The quantitative assessment of activity concentration in regions of interest in PET imaging is essential for calculating the radiation dose delivered to tumor and normal tissues in RPT. However, the limited spatial resolution of PET produces partial volume effects (PVEs) that make accurate quantification challenging. These effects are most significant in regions of steep activity concentration gradients, where the observed activity spills in and out of the lesser and greater activity regions, respectively. The magnitude of this error is largely dependent on the object size, contrast to surrounding tissues, and the intrinsic resolution of PET scanner (*157*,*158*). For large objects like the liver with generally uniform uptake of RPT agents, the impact of PVE is minimal. For small objects, a category that tumors often fall into, the impact of PVEs are more significant. Jentzen et al. (*159*) reportedly recovered only ~55% of ^{124}I activity in 12 ml spheres at a source to background ratio of 12:1. Notably, recovery of ^{18}F in this same study was 13% better than that of ^{124}I across all sphere volumes. For tumors with uniform uptake in cold background, the observed maximum activity concentration will begin underestimating the true value when the tumor is less than 2-3 times the size of the reconstructed image resolution (*160*).

Partial volume correction (PVC) has long been an area of interest in quantitative PET imaging (*161*). The focus of research has largely been in application to cardiac and neurological studies, where the biophysical behavior of anatomically defined compartments is well established (*162*). The approaches taken to partial volume correction typically fall into two categories: region-level or voxel-level. Region-level PVC generally relies on phantom studies to characterize the recovery of activity at a range of volumes and source-to-background ratios (*157*,*163*). Voxel-level PVC approaches typically rely on characterizing the ‘blur’ inherent to the system (i.e. the point

spread function (PSF)) in such a way that deconvolution-based approaches may be implemented, often with assumptions made about the underlying anatomy. (*164*,*165*). Application of region-based PVC is primarily useful for calculating more accurate region-level estimates of activity. However, because these region-level corrections effectively act as a rect function to boost the activity in a defined region, the resulting activity distribution is discontinuous and challenging to utilize in voxelwise dosimetry approaches.

Several different approaches for voxel-level PVC have been proposed to reduce or eliminate PVEs (*166*). The most accurate of these approaches incorporate anatomic segmentation information from a paired CT or MRI image. These approaches generally assume uniform activity in segmented regions and require strong correlation between tracer uptake and anatomic boundaries (*167*). However, this is rarely the case in oncology where anatomic boundaries between tumor and normal tissues are often ambiguous and heterogeneous uptake (e.g. necrosis) is observed in the activity distribution, but unapparent in anatomic images. PVC methods ignoring underlying anatomic features rely on blind iterative deconvolution, or deblurring of the image, with the imaging systems point spread function (PSF) to sharpen the input distribution. Several iterative strategies have been employed in this context, namely expectation maximization (*168*,*169*), Van Cittert's iterative method (*164*,*170*), and the Richardson Lucy algorithm (*170*) with varying degrees of success. A drawback of this method is that the deconvolution process significantly amplifies high-frequency noise in the input image. Notably, accurate voxel-level correction of PVE for the purpose of theranostic RPT dosimetry is an outstanding problem in the field (*100*).

2.4.1 Iterative deconvolution theory

Voxel-level PVC in this work is achieved through iterative deconvolution, or deblurring, of the PET imaged activity distribution (*171*,*172*). When modeled as a linear imaging system (Equation 2), the observed PET image, $g(\vec{r})$, is a result of the convolution ($\otimes$) of the true activity distribution, $f(\vec{r})$, with the imaging systems PSF, $h(\vec{r})$:

$$g(\vec{r}) = f(\vec{r}) \otimes h(\vec{r}) + \eta(\vec{r}) \quad 2$$

Here, the η term represents noise inherently added in a realistic imaging system. In Fourier space, this model can be represented by:

$$G(\vec{u}) = F(\vec{u})H(\vec{u}) + N(\vec{u}) \quad 3$$

where $G(\vec{u})$, $F(\vec{u})$, and $H(\vec{u})$ are the Fourier transforms of $g(\vec{r})$, $f(\vec{r})$, and $h(\vec{r})$. Note that the convolution operator becomes multiplicative. Here, we may naively solve for the true image, $F(\vec{u})$, by performing direct deconvolution and dividing both sides by $H(\vec{u})$:

$$\hat{F}(\vec{u}) = \frac{G(\vec{u})}{H(\vec{u})} + \frac{N(\vec{u})}{H(\vec{u})} \quad 4$$

In an ideal world without noise, direct deconvolution recovers the image perfectly (Figure 1). However, in the presence of noise, the final term in Equation 4 amplifies the noise present in the image and becomes the dominate term in the recovered image, $f'(\vec{r})$. As such, the application of direct deconvolution to realistic imaging problems, such as deblurring of PET images, has little utility.

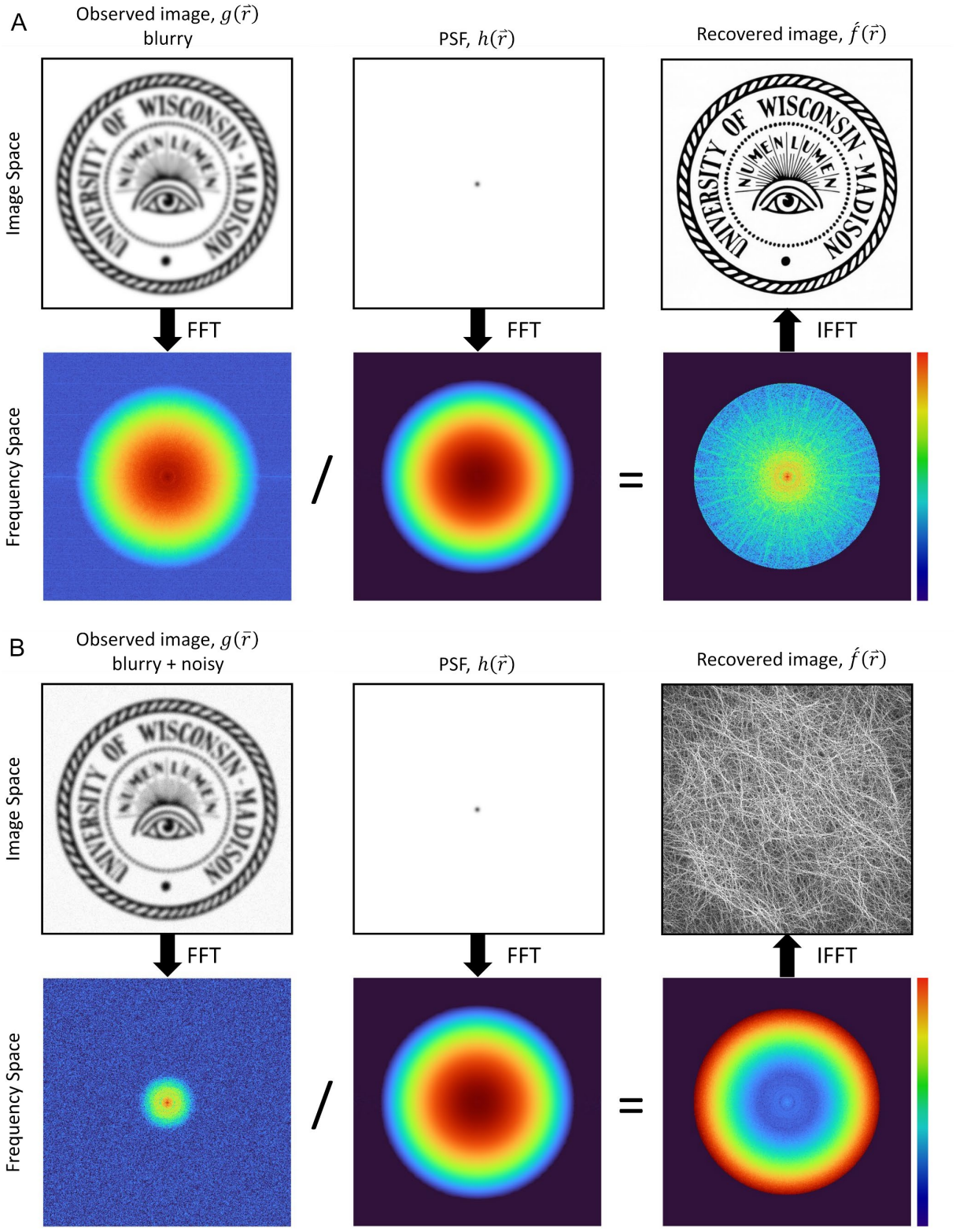

Figure 1: Example of direct deconvolution of blurry and noisy 2D images. Direct deconvolution in frequency space recovering an image that has had (A) gaussian blur or (B) gaussian blur and random noise added. FFT stands for Fast Fourier Transform and IFFT, inverse FFT

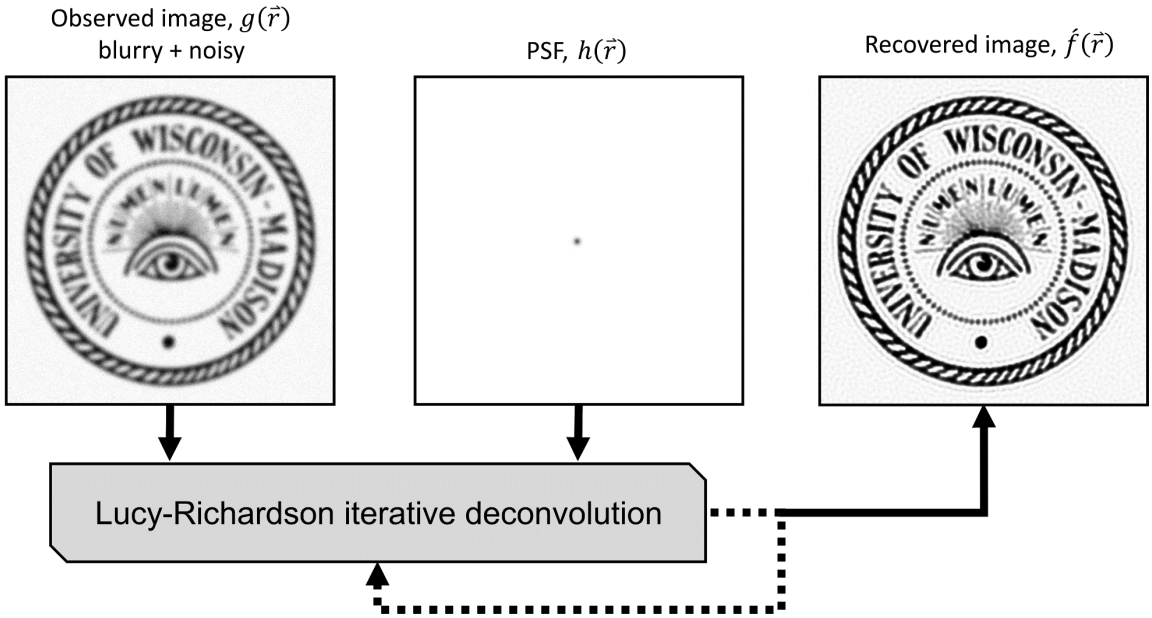

Figure 2: Demonstration of a 2D Lucy-Richardson iterative deconvolution case wherein blurry and noisy image data is restored (20 iterations) using as the PSF the gaussian kernel known to have blurred the image.

Alternative approaches to deconvolution involve iterative methods that minimize the amplification of high frequency noise. One such method that has become popular in nuclear medicine applications (*173–176*) is called the Lucy-Richardson (LR) approach, originally described independently by Leon B. Lucy (*177*) and William H. Richardson (*178*) in 1974 and 1972, respectively. LR deconvolution is an iterative expectation maximization algorithm based on a Bayesian framework that takes as input a distorted image and the PSF assumed to have generated the distortion. The algorithm then iteratively attempts to generate a recovered image that, when convolved with the input PSF, will produce the distorted input image (Figure 2). Computationally this is modeled with a multiplicative correction matrix, $c_i(\vec{r})$, where $f'_{i+1}(\vec{r})$ represents the recovered image generated from the i^{th} iteration (*179*):

$$f'_{i+1}(\vec{r}) = f'_i(\vec{r})c_i(\vec{r}) \quad 5$$

$$c_i(\vec{r}) = \left[h(\vec{r}) \otimes \frac{g(\vec{r})}{h(\vec{r}) \otimes f'_i(\vec{r})}\right] \quad 6$$

2.5 The Role of Radiotherapy in Immunomodulation

Historically, accumulation of radiation-induced DNA damage, leading to tumor cell death via apoptosis and mitotic catastrophe, is considered to be the primary mechanism by which most solid tumors respond to clinical radiotherapy (*180*,*181*). However, the amount of dose required to induce complete tumor regression is often less than what is expected to kill all targeted cells, suggesting that radiotherapy activates other tumoricidal mechanisms. In comparatively rare cases, first described over 65 years ago, radiotherapy induces an abscopal response upon where tumor regression occurs at metastatic sites distant from the irradiated region (*182*). It has since been recognized that the therapeutic anti-tumor effects of radiotherapy are modulated by host immunity (*183–185*). More recently, it has become clear that the tumor cell death elicited by radiotherapy is immunogenic and that RT triggers a variety of mechanisms that increase tumor susceptibility to immune response (*2*,*183*). The dose and dose rate of RT influences these effects (*186*).

The extent to which immunogenic cell death of cancer cells is driven by radiation follows the traditional linear-quadradic model (*187*,*188*). In surviving cancer cells, a type I interferon (IFN) response is activated through the cGAS-STING (cyclic guanosine monophosphate–adenosine monophosphate synthase – stimulator of IFN genes) pathway (*189–191*). The cGAS-STING pathway provides a mechanism through which the immune system is activated to defend against a wide variety of DNA-containing pathogens. As such, the cGAS-STING pathway is thought to be a key mechanism through which deviant tumor-derived DNA is detected and antitumor immune response activated. Notably, activation of the cGAS-STING pathway can also result in targeting of normal DNA and drive autoimmune responses. Type I IFN response appears to be the primary means through which the in situ vaccination effect of EBRT is activated.

Remarkably, the type I IFN response appears to be optimally activated at moderate dose levels (8-12 Gy) and hypo-fractionated radiotherapy regimens (e.g. 8 Gy x 3) (*191*).

At low doses (2-5 Gy), radiotherapy is also capable of modulating the immunogenicity of the tumor immune microenvironment (TME). Of all mammalian cells, lymphocytes are among the most radiosensitive with apoptosis triggered in 90% of naïve lymphocytes 2-8 h following 3 Gy irradiation (*192*). However, activated circulating T-effector cells and immunosuppressive regulatory T cells (Tregs) are more robust than naïve lymphocytes when exposed to radiation (*193*,*194*). Notably, most tumor cells are more also more radioresistant than T-effector and Tregs (*195*). Within the TME, infiltrating T cells and tissue resident memory T cells have demonstrated radioresistance that is influence by the TME (*196*). At low doses, radiation can also trigger the local release of tumor-specific antigens and inflammatory cytokines that elicit a response from the immune system, increasing immune cell trafficking (*186*,*197*). With the immune system activated by inflammatory cytokines and radiation having knocked out the vast majority of immunosuppressive Tregs and exhausted T effector cells, the TME can be reconstituted in manner that makes the tumor more susceptible to detection and anti-tumor immune responses. Interestingly, the immunomodulatory effects of low-dose radiation seem to be unmoved by the rate at which radiation dose is delivered (*186*,*197–199*).

Chapter 3

Partial Volume Correction in ^{86}Y PET Imaging and Theranostic Tumor Dosimetry

PET imaging is the most quantitative means of characterizing the in vivo functional behavior of molecular biomarkers in nuclear medicine. The greatest obstacle to obtaining high quality and quantitative PET imaging is considered to be that of PVEs (*160*). Generally, this effect is described as the spill in and out of activity between adjacent regions with high or low activity, resulting in the observation of activity in PET images that is not representative of the true distribution. A number of sources contribute to the magnitude of PVEs, but in the case of non-ideal tracers with non-negligible positron range (e.g. the most commonly emitted positrons from ^{86}Y have a maximum range of 5.6 mm) and significant prompt gamma contamination, PVEs make quantitative imaging more challenging (*200*). Given the accuracy of theranostic dosimetry depends on the resolution and quantitative accuracy of the PET imaging it is based on, the use of PVC is essential to achieving accurate dosimetry estimates. In this chapter, the use of region and voxel-

level approaches to partial volume correction and their impact on quantitative imaging of ^{86}Y and theranostic ^{86}Y/^{90}Y dosimetry estimates is investigated. First, the impact of PVEs on imaging and dosimetry of ^{86}Y-NM600 in preclinical tumor models is explored and the means through which these effects can be mitigated using PVC is demonstrated. Then, the PVE in ^{86}Y imaging is characterized in a clinical scanner and PVC methods are developed to improve the dosimetric accuracy of subsequent companion canine studies.

3.1 Methods and Materials

3.1.1 Radiosynthesis of $^{86/90}$Y-NM600

The production of ^{86}Y and radiolabeling of NM600 has been described in detail elsewhere (*17*,*73*). Briefly, ^{86}Y was produced in a GE PETrace biomedical cyclotron via proton bombardment (14.1-7.1 MeV) of enriched ^{86}Sr-$SrCO_3$ (96.4% ± 0.1%) targets. Following irradiation, targets were dissolved in 6N HCl, loaded onto an extraction resin functionalized with N,N,N',N'-tetrakis-2-ethylhexyldiglycolamide (branched DGA, Eichrom), and washed with diluted H_3NO_3 (0.01 M), and ^{86}Y was quantitatively eluted from the column in less than 600 µL of 0.1 M HCl. $^{90}YCl_3$ was purchased from Perkin Elmer and used without further purification. Radiolabeling of NM600 with ^{86}Y and ^{90}Y was performed at the same specific activity by buffering 185–370 MBq (5-10 mCi) of ^{86}Y/^{90}Y with 0.1 M NaOAc (pH 5.5) and adding 296 nmol/GBq (10 µg/mCi) of NM600. ^{86}/^{90}Y-NM600 was purified via a solid-phase extraction cartridge (HLB; Waters) and eluted in 2 mL of 200-proof ethanol. The eluate was then evaporated under a nitrogen stream, and ^{86}Y/^{90}Y-NM600 was reconstituted in excipient (saline containing 0.4% v/v polysorbate 20). Radiolabeling yield and radiochemical purity were assessed by instant thin-layer chromatography. Instant thin-layer chromatography chromatograms were developed using a cyclone phosphor-plate imager and analyzed with Optiquant software (Perkin Elmer).

3.1.2 Mice and tumor models

All animal studies were conducted under National Institutes of Health guidelines and University of Wisconsin Institutional Animal Care and Use Committee–approved protocols as previously described (*17*). Male or female C57Bl/6 (B6), Balb/c, FVB, or NOD.Cg-Prkdc^{scid}

Il2rg^{tm1Wjl}/SzJ (NSG) mice were purchased from either Taconic or Jackson Labs and used at 8-12 weeks of age. In vivo uptake of ^{86}Y-NM600 and theranostic $^{86/90}$Y-NM600 tumor dosimetry was studied in seven different cancer cell lines: B78 melanoma (*201*), Panc-02 pancreatic adenocarcinoma (*202*), LLC Lewis lung carcinoma (ATCC CRL-1642), MyC-Cap prostate cancer (*203*), EL-4 murine T-cell lymphoma (ATCC TIB-39), Hut-102 human T-cell lymphoma (*204*), and HCT-116 colon cancer (ATCC CCL-247). Flank tumors were engrafted via subcutaneous injection of 0.5-2×10^6 cells. Tumor size was monitored twice weekly, and volume calculated using digital caliper measurements and the ellipsoid volume formula:

$$V = L \times \frac{W^2}{2} \qquad 7$$

where L and W are the maximum and minimum tumor dimensions, respectively. In vivo imaging studies were commenced once tumor volumes reached at least 200 mm^3.

3.1.3 MicroPET/CT imaging and biodistribution

Mice bearing flank tumor xenografts (n= 3-4 per tumor model) were administered 9.25 MBq of ^{86}Y-NM600 via tail lateral vein injection. Sequential PET/CT scans were acquired in an Inveon® micro-PET/CT scanner (Siemens Medical Solutions USA, Inc, Malvern, PA) at 2, 24, 48, and 72 hrs after injection. Prior to each scan, mice were anesthetized with isoflurane (4% induction, 2% maintenance) and placed in a prone position on the scanner bed. CT scans (80 kVp; 1000 mAs; 275 ms; 220 angles) were reconstructed via filtered back projection using the system software with a Shepp-Logan filter to a 0.2 x 0.2 x 0.2 mm^3 resolution. List mode PET scans consisting of 80 million coincidence events per mouse (time window, 3.432 ns; energy window, 350–650 keV) were reconstructed using a three-dimensional ordered subset expectation maximization (OSEM-3D) algorithm with 16 subsets and 4 iterations, attenuation correction, and

no scatter correction to a 0.8 x 0.8 x 0.8 mm^3 resolution. The resulting PET and CT image volumes were coregistered and corrections for attenuation, normalization, and dead time were made using the system software. Region of interest (ROI) analysis and quantification was performed with contours drawn on the anatomic CT image volumes. Quantitative in vivo data is expressed as percent injected activity per gram (%IA/g), assuming unit density of tissue. Following the final 72 h timepoint, mice were sacrificed, and tumor tissue was collected to corroborate the accuracy of in vivo PET-based measurements. Tumors were weighed and activity was counted in a Wizard 2 automated γ-counter (Perking Elmer) to calculate the %IA/g ex vivo. For large tumors with observable necrotic regions, only viable tumor tissue was resected for measurement in the gamma counter.

3.1.4 Preclinical PVC phantom study

We assessed the impact of PVE on ^{86}Y PET-based tumor uptake and dosimetry in this work with a 3D printed partial volume correction phantom (Phantech, Madison, WI). The phantom contains a single-channel series of 9 spherical voids ranging from 3.7 to 24.8 mm in diameter and surrounded on one side by a half-cylindrical void for filling with background activity. Connected in series with the spherical voids is a large 41 mm diameter cylindrical reference region (Figure 3). The phantom was filled with ^{86}Y solution buffered to 0.01 M HCL at 104.6 kBq/ml and 27.3 kBq/ml (1:4) in the hot sphere and warm background regions, respectively. PET images were reconstructed with the same parameters used in animal imaging studies (OSEM-3D, 16 subsets, 4 iterations, attenuation correction, no scatter correction). Resulting PET and CT images were rigidly registered using normalized mutual information and contours were drawn on the CT image volume to measure observed activity concentration. Spherical ROIs were adjusted to match the known volume of each void. The recovery coefficient (RC) at each sphere volume was calculated using:

$$RC = \frac{AC_{PET}}{AC_{true}} \quad (8)$$

where AC_{true} represents the mean activity concentration observed in the reference chamber. The relationship between RC and sphere diameter was then fit to a sigmoidal function to allow for calculation of RC at any sphere diameter (d) corresponding to measured tumor volume delineated in imaging studies:

$$RC = \frac{1}{1 + \left(\frac{a}{d}\right)^{b}} \quad (9)$$

Holding the numerator to one ensures that RC approaches 100% as sphere size goes to infinity.

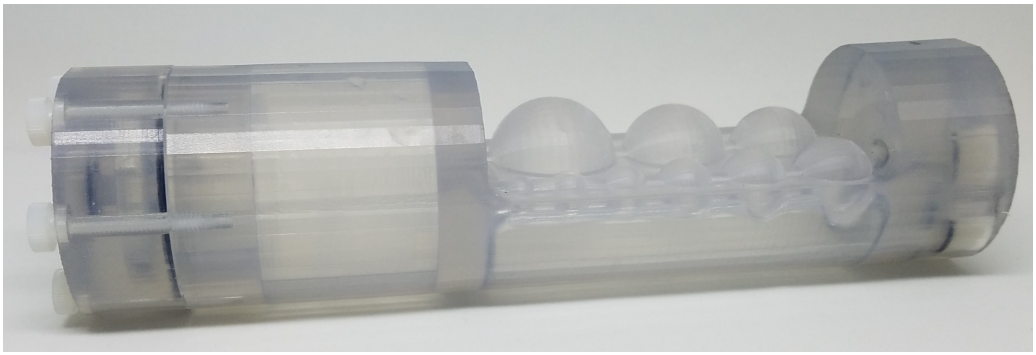

Figure 3: Photo of PVC phantom showing reference region, hot spheres, and surrounding warm background half-cylinder.

Partial volume corrected in vivo tumor uptake measures can be calculated in the following way using the measured RC for ^{86}Y:

$$A_{PVC} = \left(A - A_{bkgd}\right)\left(\frac{1}{RC}\right) + A_{bkgd} \quad (10)$$

where A_{bkgd} represents background activity from an ROI drawn on adjacent nonspecific tissue (*158*,*205*). Subtracting background activity prior to applying RC allows for correction of spill-in and spill-out effects with varying degrees of background activity. In the setting where tumor uptake

is identical to adjacent nonspecific uptake, as is often the case at early timepoints in an imaging series, no PVC be applied.

3.1.5 Theranostic ^{86}Y/^{90}Y-NM600 dosimetry in preclinical tumor models

Dosimetry for ^{90}Y-NM600 in this preclinical work was assessed using in vivo ^{86}Y-NM600 PET/CT imaging and the Radiopharmaceutical Assessment Platform for Internal Dosimetry (RAPID) (*206*). ^{86}Y-NM600 PET image volumes (resolution, 0.78 x 0.78 x 0.80 mm) are rigidly registered to the corresponding CT image volume (resolution, 0.21 x 0.21 x 0.21 mm) at each scan timepoint using normalized mutual information and resampled to an intermediate resolution (resolution, 0.42, 0.42, 0.42 mm) for dosimetry analysis. PET image volumes representing ^{86}Y-NM600 are decay corrected to represent ^{90}Y-NM600 and absorbed dose rate (ADR) distributions are generated at each timepoint using Geant4 (version 9.6) Monte Carlo simulations. The CT and PET image volumes from each timepoint are used to define the geometry and source distribution, respectively. Decay of ^{90}Y is simulated uniformly throughout each source voxel using the G4RadioactiveDecay module that obtains decay information from ENSDF database (*207*,*208*). Over 10,000 decays of ^{90}Y were simulated in each source voxel, or approximately 3.6E+09 decays per PET/CT image, to achieve less than 1% relative error in tumor ROIs. Tumor and normal tissues were manually drawn at each timepoint using on the anatomical CT images for reference. The mean cumulative absorbed dose (AD) delivered to the tumor was then calculated via temporal integration of the mean ADR in the tumor ROI at each timepoint. The time-dose rate curve was modeled with a trapezoidal-exponential fit, assuming purely exponential radioactive decay of ^{90}Y from the time timepoint to $t = \infty$. Final dosimetry estimates for preclinical tumor models were corrected for PVE using RC measured in the preclinical PVC phantom study. For the preclinical

tumor dosimetry presented in this work, estimates of Rx Dose were corrected for PVE using RC alone.

3.1.6 Iterative deconvolution

While LR deconvolution assumes a spatially invariant PSF, it is known that the PSF of a PET imaging system is spatially varying in dimension throughout the frame of view of the scanner, with locations distal to the center of the FoV producing a more spread-out PSF. To compensate for this phenomenon, the application of LR deconvolution has been locally limited to designated regions defined by physician drawn contours. A margin of 2 cm is added to target ROIs to generate a 3D binary mask that designates which voxels will be subject to LR deconvolution. The margin also helps account for poorly defined contours where high uptake voxels are present adjacent to the tumor ROI. The centroid of this mask, relative to the center of the FoV, defines a radial vector, $\vec{r}$, which is used to generate a 3D anisotropic gaussian modeled PSF based on experimental point source measurements. Following LR deconvolution, the binary mask is edge-tapered, and the locally recovered PET distribution is superimposed into the original PET distribution.

In this work, the accuracy of LR deconvolution using experimentally validated ^{86}Y PSF modeling will be primarily compared against the established PSF modeling option available for the GE Discover MI scanner (GE Healthcare, Waukesha, WI). SharpIR is GE's solution for incorporating PSF modeling into PET reconstruction and this proprietary approach utilizes their inhouse PSF model for the scanner (*209–211*). However, this PSF modeling is intended for ideal PET tracers and is potentially inadequate in accounting for the unique characteristics of ^{86}Y in PET imaging. As such, the results from the post-reconstruction LR deconvolution approach developed in this work (shown as VPHD-LR) will be compared the GE's SharpIR PSF modeling solution (shown as VPHD-S).

3.1.7 Establishing a stopping criterion

The primary drawback of LR deconvolution is that it can require a relatively large number of iterations to arrive at a stable recovered image. Furthermore, excessive iterations can introduce unnecessary ringing artifacts as high frequency noise in the image is amplified while the correction matrix forces voxel values to oscillate about their stable solutions. Therefore, it's essential to establish an appropriate stopping criterion to achieve high quality deconvolved PET distributions. The progression of LR deconvolution between iterations can be most directly observed by the rate of change of the multiplicative correction matrix, $c_i(\vec{r})$. Since this correction matrix is made up of multiplicative correction factors for each voxel centered about 1.0, the average sum of square differences between the correction matrix and a matrix of ones can be calculated to quantify the absolute magnitude of multiplicative correction at each iteration:

$$C_{err,i} = \frac{1}{N}\sum_{n=1}^{N}(c_n - 1)^2 \qquad 11$$

where N is the total number of voxels in the tumor mask. As the number of iterations increase, C_i will approach zero. Further, the rate of change of C_i between iterations, $\Delta C_{err,i}$, can help identify the point at which the LR iterative deconvolution begins oscillating about a stable solution:

$$\Delta C_{err,i} = \frac{C_{err,i} - C_{err,i-1}}{C_{err,i-1}} \qquad 12$$

This metric is used to establish the stropping criterion based on phantom studies.

Of more important relevance to this work is the impact that LR deconvolution has on the accuracy of the recovered activity distribution. In this work, clinical phantom studies (discussed below) using known activity concentrations were used to benchmark the implemented LR

deconvolution approach. With the true activity distribution underlying the PET image, the average voxel-level accuracy of the recovered PET image, PVC_{err}, is calculated for each iteration using:

$$PVC_{err,i} = \frac{1}{N}\sum_{n=1}^{N}\left|f_{true,n} - f'_n\right| \quad 13$$

Here, $f_{true,n}$ represents the true reference activity at each voxel index, n. The rate of change of $PVC_{err,i}$ can then be similarly determined to $\Delta C_{err,i}$ using:

$$\Delta PVC_{err,i} = \frac{PVC_{err,i} - PVC_{err,i-1}}{PVC_{err,i-1}} \quad 14$$

3.1.8 Characterizing the spatially variant PSF

The PSF of ^{86}Y was determined in the GE Discovery MI scanner using a point source with an axial extent of less than 1.2 mm that was prepared in a glass capillary tube (McKesson capillary tube, SKU 177-51602). A microdroplet of ^{86}Y solution at an activity concentration of 15.7 MBq/ml was prepared on a hydrophobic surface, captured in the end of the capillary tube, and hermetically sealed with wax sealant. The longitudinal extent of the point source was approximately 2 mm. The point source was then mounted at the end of a custom designed arm installed on the Washington University 4D Motion Stage and aligned to the central plane of the FOV (Figure 4). The point source was then aligned to the isocenter of the FoV using in-room lasers and scanned at varying radial distances from the center of the FoV. Sixteen scans were performed as the point source was stepped horizontally to a radial distance of 20 cm using increments of 4 x 2.5 mm, 2 x 5 mm,

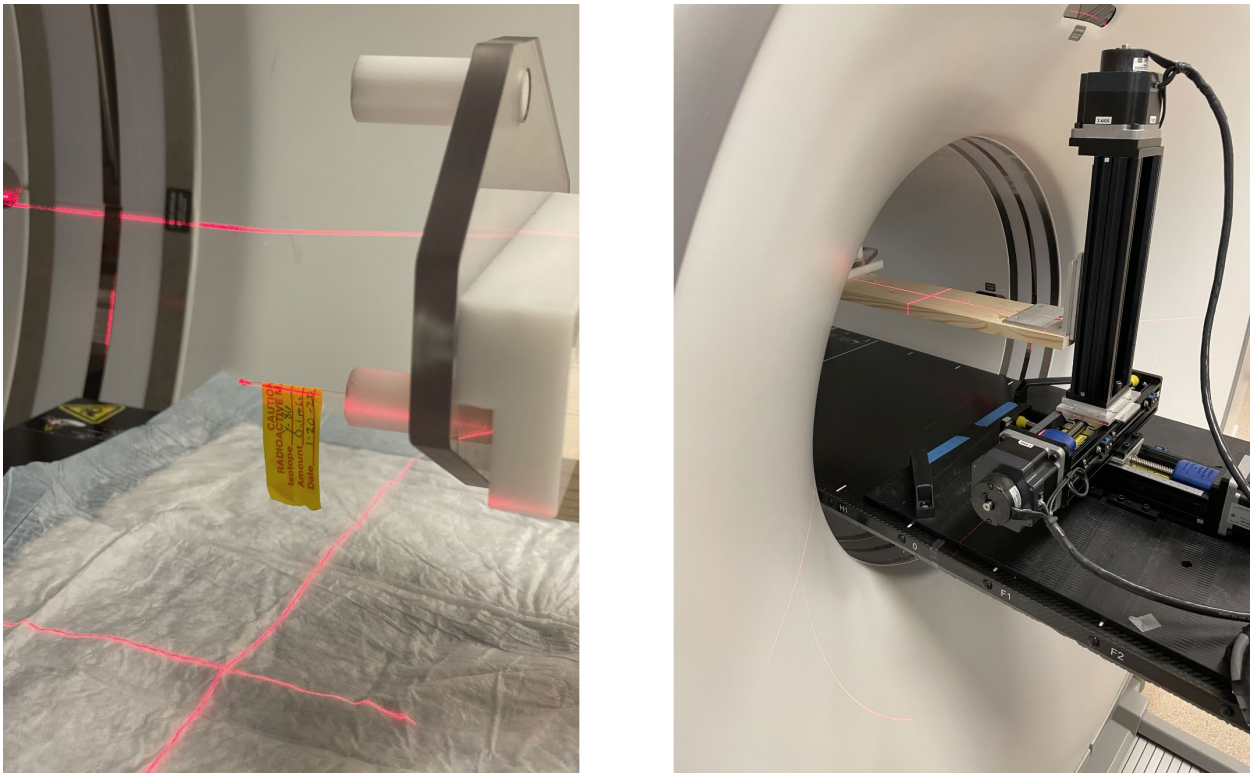

Figure 4: Experimental setup for characterizing the PSF of ^{86}Y using a point source mounted on a 4D motion stage.

3 x 10 mm, and 6 x 25 mm. Scanning at each position lasted from 74 to 82 seconds, accumulating a total of 5.0 x 10^5 prompts.

Point source PET images of the point source were reconstructed using the VPHD (OSEM-3D, 16 subsets and 4 iterations) reconstruction algorithm in a 384 x 384 x 71 matrix at a high resolution of 1.30 x 1.30 x 2.79 mm. Data was corrected for random coincidences, normalization, dead-time- losses, and scatter. No gaussian filtering was used to preserve PSF acuity.

The resulting images were then fit to a three-dimensional gaussian function using a least squares method. The full width at half maximum (FWHM) in the radial (ρ), tangential (θ), and axial (z) dimensions was characterized at each position (Figure 5). The resulting gaussian FWHM parameters were plotted against radial distance from the center of the FoV and fit to a second order polynomial.

$$h(\vec{r}\,) = \frac{1}{b_\rho(\vec{r}\,')\; b_\theta(\vec{r}\,')\; b_z(\vec{r}\,')}\; exp\left(-\pi\left(\left(\frac{\vec{r}\cdot\hat{\rho}}{b_\rho(\vec{r}\,')}\right)^2 + \left(\frac{\vec{r}\cdot\hat{\theta}}{b_\theta(\vec{r}\,')}\right)^2 + \left(\frac{\vec{r}\cdot\hat{z}}{b_z(\vec{r}\,')}\right)^2\right)\right) \qquad (15)$$

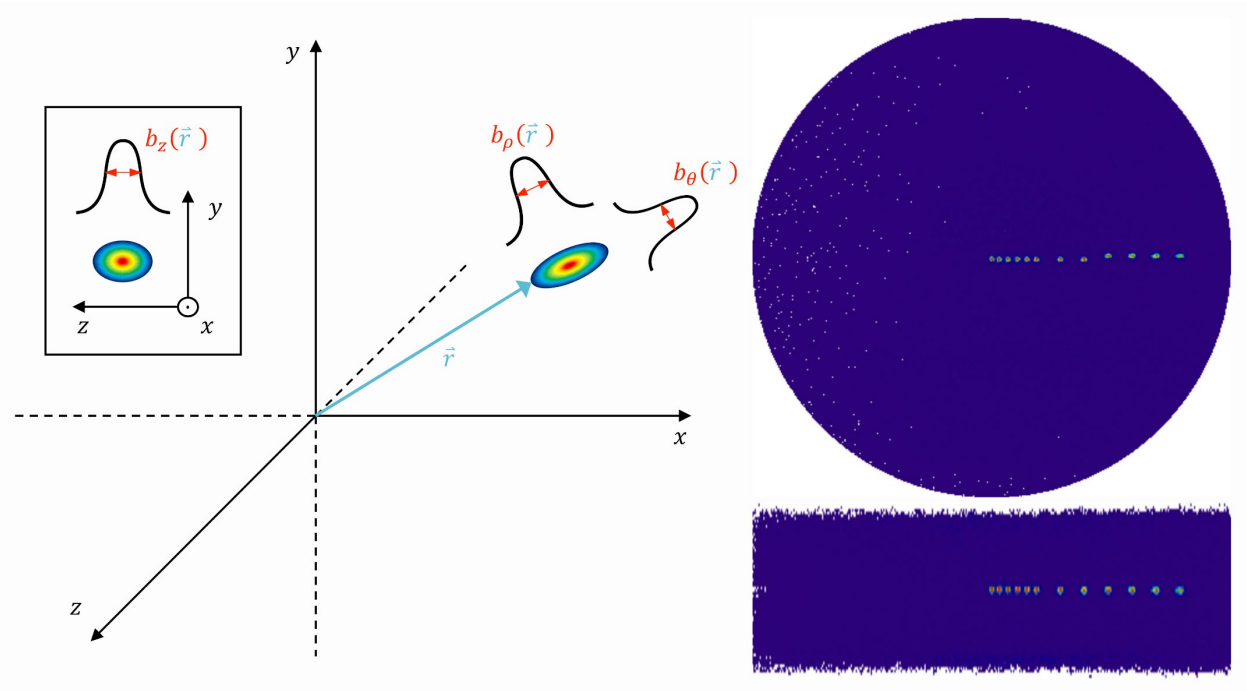

Figure 5: Diagram depicting measurements of the ^{86}Y PSF in cylindrical coordinate space and fit to 3D gaussian distribution (left). PSF measurements acquired along a horizontal line beginning at the center of the scanner frame of view. Selected superimposed PSF images shown in axial (top right) and coronal (bottom right) projections.

3.1.9 Clinical phantom studies

Two phantom studies were performed to assess PVC methods and validate quantitative ^{86}Y PET imaging on the GE Discovery MI PET/CT scanner. The first phantom was a Jaszczak Flangeless Deluxe PET and SPECT phantom with a set of 6 hollow spheres (Figure 6). The main cylindrical compartment of the phantom was 20.4 cm in diameter and 18.6 cm in height (6.4 L in volume). The base of the cylinder contained six equally distanced threaded holes for mounting solid or hollow spheres on 12.7 cm rods. In this work, we utilized hollow spheres with volumes ranging from 0.5 to 16 ml (9.8 to 31.3 mm diameter). Hollow spheres were filled with approximately 75.6 kBq/ml of ^{86}Y ($t_{1/2}$ = 14.7 h) in solution while the primary compartment of the phantom was filled with a background activity concentration of 7.9 kBq/ml of ^{86}Y. Solutions of ^{86}Y contained DI water buffered to 0.01 M HCL (pH of 2.0) to prevent ^{86}Y from precipitating and sticking to the plastic walls of the phantom. Prior to phantom filling, three samples of the hot sphere solution were gathered in vials, individually weighed prior to filling, to quantify activity

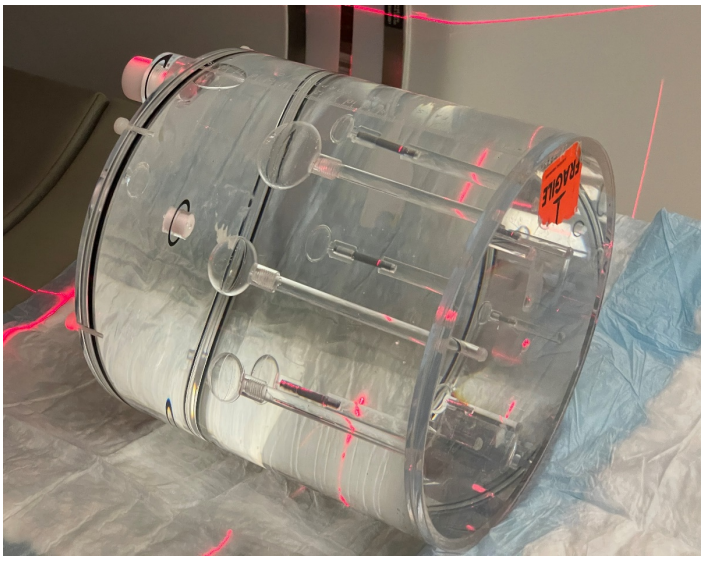

Figure 6: Jaszczak Flangeless Deluxe PET and SPECT phantom with a set of 6 hollow spheres.

concentration using an automated gamma counter (Wizard 2, Perking Elmer). Following imaging, the background solution was sampled and measured as well.

The second phantom was a spherical gradient phantom consisting of four fillable concentric voids of equal radial thickness (Figure 7). The phantom is 8.9 cm in diameter (369 ml) with a radial distance between shells of 1 cm. The thickness of the 3D printed shells between voids was approximately 2 mm. The volume of each fillable region was 5.1, 35.8, 94.9, and 185.7 ml. For this study, the two outermost and innermost shells were filled with an activity concentration of 37.2 and 18.7 kBq/ml, respectively, to represent a tumor with a necrotic core. Activity concentration was chosen based on observations from ^{86}Y-NM600 companion canine studies on the same scanner. Both hot and cold solutions of ^{86}Y contained DI water buffered to 0.01M HCL to prevent precipitation of ^{86}Y.

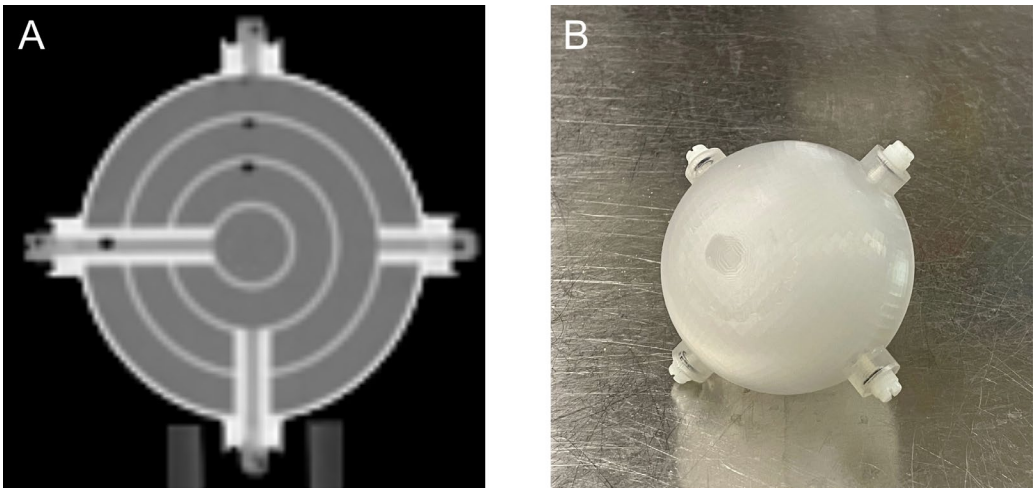

Figure 7: Spherical gradient phantom with four isolated concentric voids. (A) Axial slice from CT scan of filled phantom showing each concentric void. (B) Photograph of phantom prior to scan.

For all clinical phantom studies, PET images were reconstructed using the VPHD (OSEM-3D, 16 subsets and 4 iterations) image reconstruction algorithm in a 192 x 192 x 125 matrix (192 x 192 x 71 for the gradient phantom study) at a resolution of 3.65 x 3.65 x 2.79 mm. Data was

corrected for random coincidences, normalization, dead-time losses, and scatter. A standard z-axis gaussian filter was used during reconstruction.

The activity concentration of ^{86}Y solution within clinical phantoms was measured using either the Capintec CRC-25R dose calibrator (Mirion Technologies) or the Wizard 2 automated γ-counter (Perking Elmer). Calibration of both well counters for measurement of ^{86}Y was performed based on measurements of ^{86}Y with the high purity germanium detector in the Cyclotron lab. Notably, the calibration factor of 850/2 determined through this process for the Capintec dose calibrator differed from the calibration setting of 711/2 suggested by the manufacturer. The manufacturer recommended calibration factor for ^{86}Y resulted in activity measurements 17.8% higher than that that of the in-house calibration. For this work, a calibration factor of 850/2 was used based on the in-house calibration.

3.1.10 Incorporating RC-based PVC into theranostic ^{86}Y/^{90}Y-NM600 tumor dosimetry

The application of RC-based PVC to theranostic dosimetry estimates requires careful consideration of several factors. The recovery of PET-imaged ^{86}Y activity in tumors is modeled with a uniform distribution of activity in a spherical geometry. As the anatomical and functional characteristics of the tumors deviate from that definition, as with aspherical heterogeneous distributions of activity, RC-based PVC should then be applied carefully. Differences between the dose distribution generated from a rect-defined true activity distribution and that of the PET imaged activity distribution must be accounted for when these ideal conditions are assumed. In this work, the following equation is used to account for these differences:

$$D_{PVC} = \left(D - D_{spill\ out} - D_{bkgd}\right)\left(\frac{1}{RC}\right)\left(\frac{SAF}{SAF_{PET}}\right) + D_{bkgd} \qquad 16$$

First, the application of the inverse RC factor ensures recovery of the true mean activity within the tumor ROI and, thus, dose to that ROI from activity within the ROI. However, the dose distribution within the ROI includes dose contributions from both a uniform background activity (D_{bkgd}) and spill-out activity ($D_{spill\ out}$) outside the defined target ROI. As such, the mean dose contributions from these factors must be subtracted from the observed mean dose present in the PET imaged ROI. Second, the difference between the self-absorbed fraction (SAF) observed in the true, uniform, activity distribution and the heterogeneous PET imaged distribution must be considered. Although cumulative activity is conserved in the PET imaged distribution with application of the inverse RC factor, the sloped edges (at times gaussian shaped) PET distribution preferentially localizes activity, and dose, to the center of the ROI. This results in less energy being deposited outside the ROI and an overall higher SAF, and higher mean dose, than should be present. Multiplying by the ratio of *SAF* to SAF_{PET} accounts for this discrepancy. While these factors can be directly assessed in clinical phantom studies, their application requires more generalizable model to be defined from phantom studies. In this work, $D_{spill\text{-}out}$, D_{bkgd}, and SAF/SAF_{PET} are characterized against RC and sphere volume for each reconstruction approach used.

3.2 Results

3.2.1 ^{86}Y-NM600 in preclinical mouse models

Longitudinal PET/CT imaging studies were performed over the course of 72 hours after administration of ^{86}Y-NM600 to seven groups of mice (n = 3-4 each) bearing flank tumor models of B78, Panc-02, LLC, MyC-Cap, EL-4, Hut-102, and HCT-116. 3D renderings of the PET/CT images of representative mice from each cohort at 72 hours can be seen in Figure 8. Here, preferential tumor uptake was observed in all tumor models, with B78 showing the least uptake. The high concentration of ^{86}Y-NM600 in the liver of each model is indicative of the hepatobiliary clearance of the agent. In vivo uptake of ^{86}Y-NM600 in the tumor, liver, kidneys, and bone marrow (femur) across all imaging timepoints is shown in Figure 9. Kidney and marrow uptake is shown averaged across both left and right ROIs. The kidneys exhibit rapid initial uptake (6.70 ± 1.80 %IA/g at 2 h) followed by progressive clearance of ^{86}Y-NM600 by 72 h (3.78 ± 0.91 %IA/g). The liver also demonstrates clearance of ^{86}Y-NM600 by 72 h, but the peak uptake of (11.03 ± 3.34 %IA/g) is delayed until 24 h, which is expected given the slower metabolism rate of hepatobiliary clearance. The marrow exhibits little to no uptake of ^{86}Y-NM600 with 1.95 ± 0.75 %IA/g at 72 h. In contrast to normal tissues, a profile of prolonged uptake and retention of ^{86}Y-NM600 is observed in all tumor models with varying degrees of intensity ranging between 3.11 to 7.04 %IA/g at 48 h post injection. Peak tumor uptake is observed between 24 to 72 h post-injection, with 48 h being the most common time of peak uptake. Panc-02 and EL-4 cohorts exhibited the highest uptake of ^{86}Y-NM600 at 7.04 ± 1.81 %IA/g and 6.25 ± 0.09 %IA/g, respectively, 48 h after injection and prior to PVC.

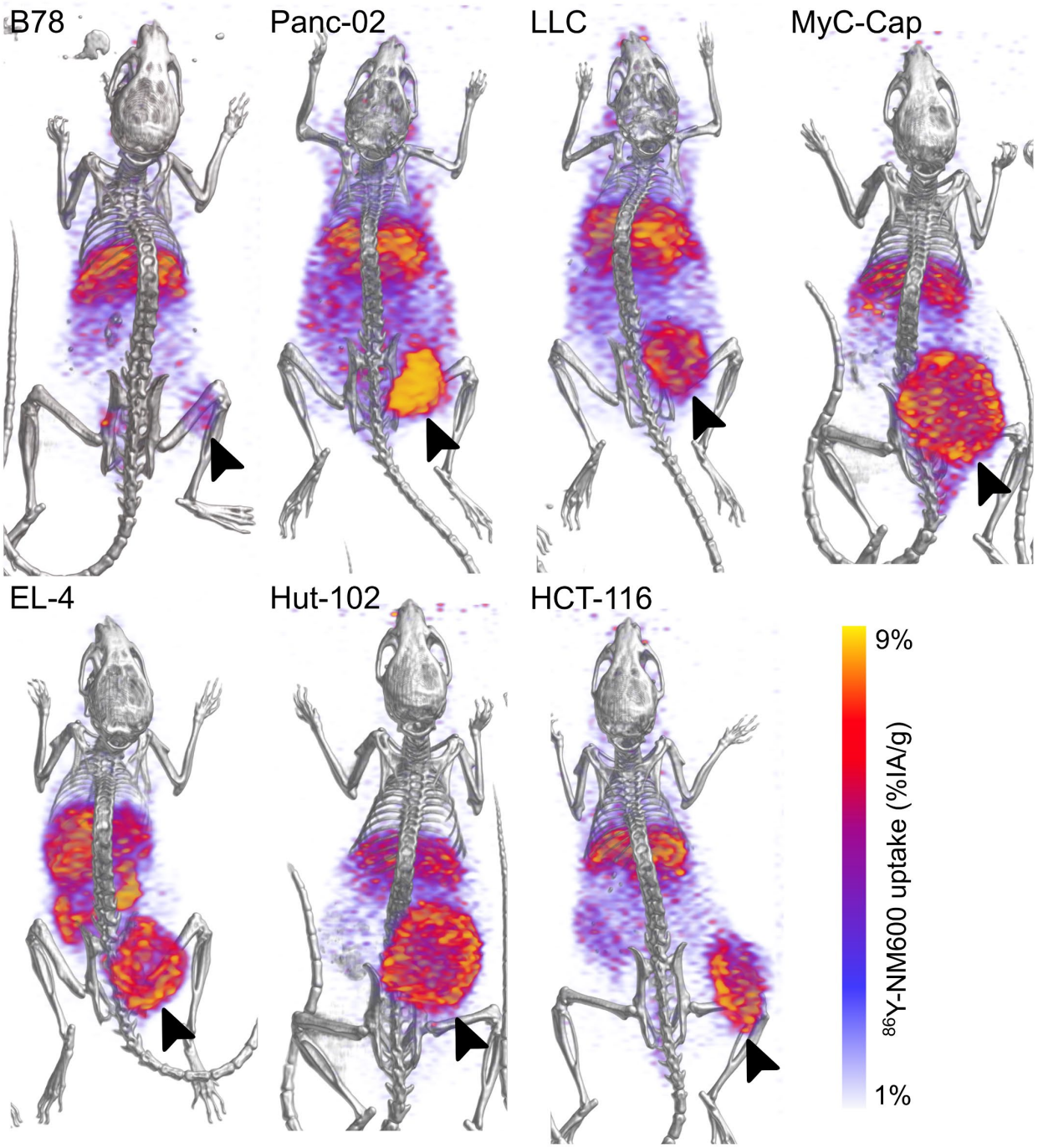

Figure 8: 3D renderings of fused PET/CT image volumes of representative mice bearing flank tumors (arrows) 72 h after intravenous injection of ^{86}Y-NM600.

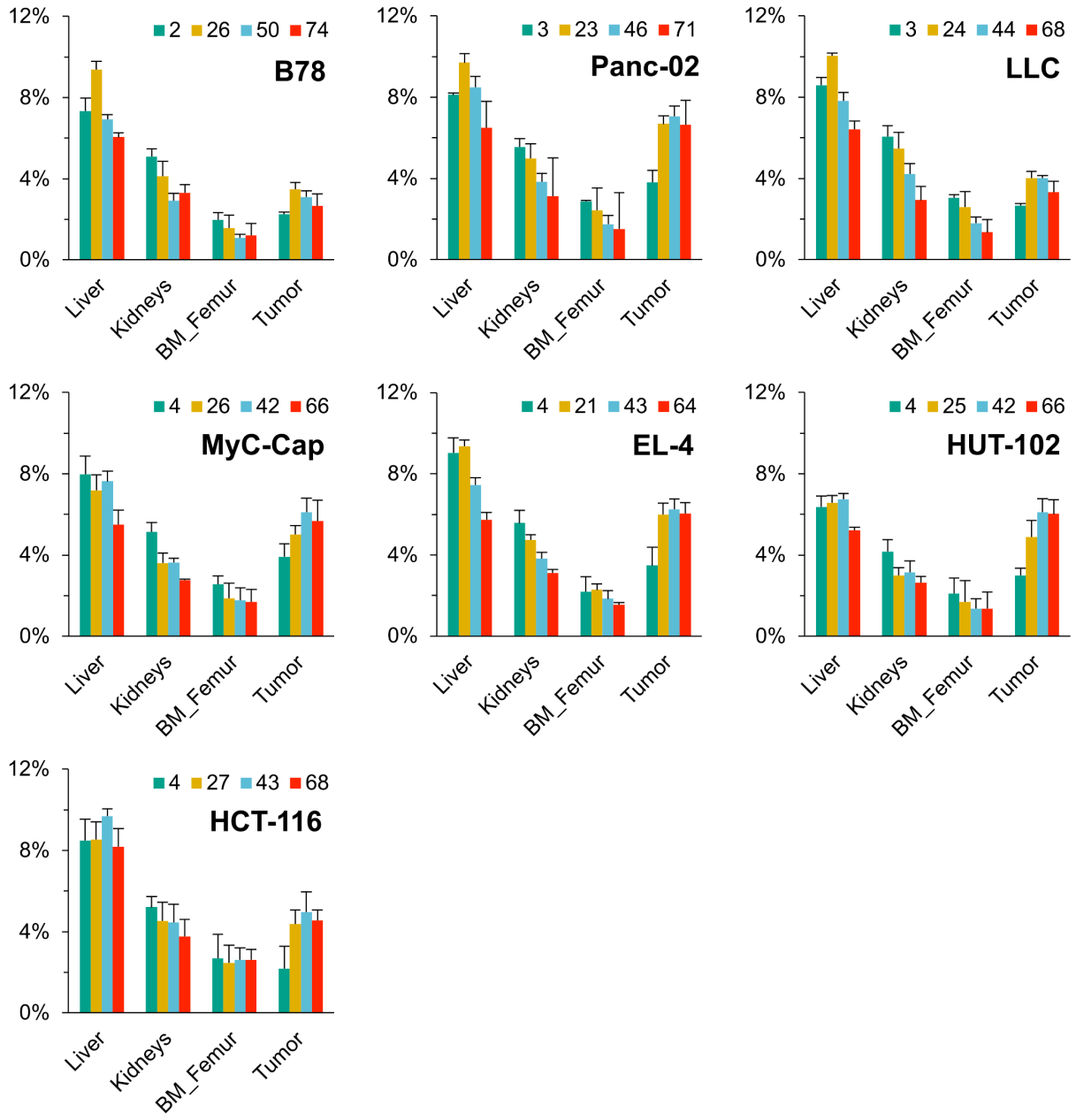

Figure 9: In vivo biodistribution of ^{86}Y-NM600 in tumor models of B78, Panc-02, LLC, MyC-Cap, EL-4, Hut-102, HCT-116 as determined by ROI analysis of PET/CT imaging. %IA/g for each ROI is shown as mean ± SD for each tumor model (n=3-4).

Blood activity over the course of the imaging series was also assessed based on a heart contour (blood pool) at each timepoint. The time activity curve of blood activity concentration was fit to a mono-exponential function and the biological half-life was separated from the decay rate constant. Table 4 reports the biological half-life of ^{86}Y-NM600 in blood as determined from each tumor model cohort. The mean biological half-life across all tumor models was 33.1 ± 5.8 h (n = 22).

Table 4: Biological half-life of ^{86}Y-NM600 in blood of tumor bearing mice (n = 3-4) based on a mono-exponential fit.

Cell line	**$t_{1/2}$ (h)**
B78	28.6
Panc-02	38.8
LLC	33.1
MyC-Cap	27.6
El-4	26.7
HUT-102	29.7
HCT-116	40.5
Mean	33.1 ± 5.8

3.2.2 Phantom-based PVC improves accuracy of in vivo uptake

MicroPET/CT scans of the preclinical PVC phantom filled with ^{86}Y were acquired at two bed positions centered on the large normalization chamber and the hot sphere segments of the phantom (Figure 10). The activity concentration measured in the uniform normalization chamber on the PET image was 104.49 kBq/ml, which compared well with the gamma counter measured activity concentration of 104.58 kBq/ml. For scans reconstructed with filtered back projection and OSEM-2D, the observed activity concentration was 107.25 and 107.49 kBq/ml, respectively. PET images were reconstructed using attenuation correction and no scatter correction. As can be seen in the coronal slices of the OSEM-3D PET images, prompt gamma contamination and scatter generate considerable activity seen in air outside the phantom (mean, 9.04 kBq/ml). However, scatter correction in microPET/CT imaging in this work was not performed due to perceived variability and poor implementation of scatter correction algorithm in the manufacture's reconstruction software. Imaging and reconstruction parameters were matched to those used in ^{86}Y-NM600 tumor mouse model studies.

The recovery of ^{86}Y activity in the spheres was determined via ROI analysis of the fused PET/CT images. Contours of each sphere were drawn on the CT image and ROI volumes were adjusted to match known sphere volume from the 3D phantom model with a mean difference of 0.6 ± 4.6%. Recovery coefficients (RC) were calculated for each sphere volume and fit to a sigmoidal function (Equation 9) against sphere diameter and volume (Figure 11). RC values are normalized to 100% of the activity concentration observed in the normalization chamber. At the largest sphere size, 24.8 mm in diameter, recovery of ^{86}Y reaches 80%. Recovery of ^{86}Y begins to drop appreciably at or below 10 mm in diameter.

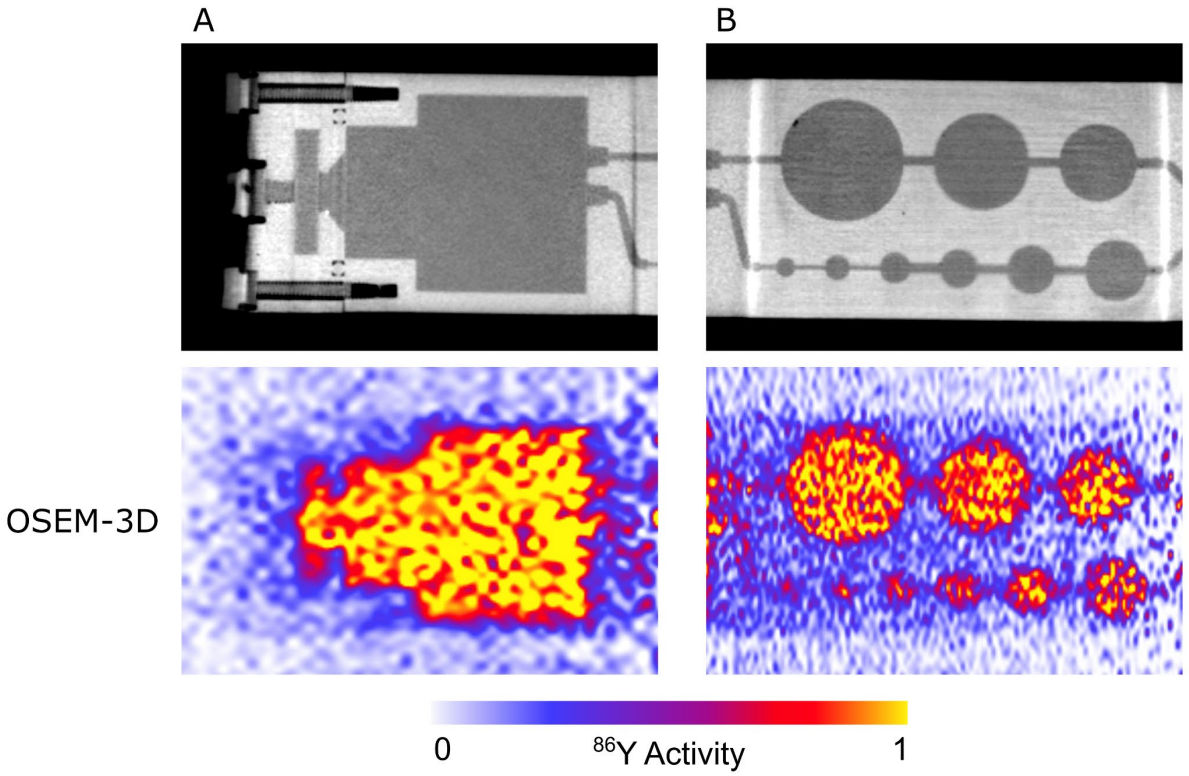

Figure 10: Coronal slices of PET images of the preclinical PVC phantom (A) normalization chamber and (B) hot sphere segments. PET images reconstructed using 3D-OSEM and shown normalized to the mean activity observed in the normalization chamber. Coronal slice of the PVC phantom CT scan shown (top) for context.

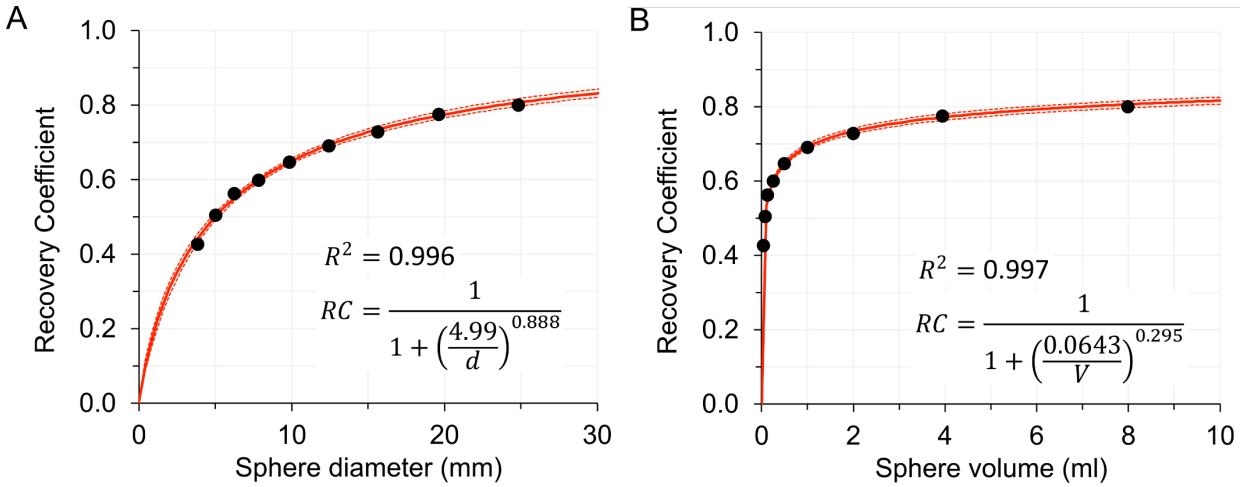

Figure 11: Recovery of ^{86}Y in hot spheres ranging from 3.8 to 24.8 mm in diameter and imaged with preclinical microPET/CT using OSEM-3D reconstruction. Sigmoidal fit shown with 95% confidence intervals against sphere (A) diameter and (B) volume.

For a subset of mice used in ^{86}Y-NM600 imaging and dosimetry studies (n = 22), tumor tissue was excised following the final imaging timepoint (72 h) and an additional ex vivo biodistribution measure of update was acquired. PVC using phantom measured RC was applied to in vivo uptake based on the mean segmented tumor volume observed over the course of the imaging study using Equation 10. Tumor volumes in mice ranged between 6.0 and 17.8 mm in diameter, assuming spherical geometry. The accuracy of in vivo uptake improved significantly following PVC (Figure 12) with the absolute differences between in vivo and ex vivo measurements reduced from -36.0% ± 10.1% to -9.4% ± 14.4%. While the paired t-test p-value ($p < 0.0001$) suggests evidence of systemic bias between the initial in vivo and ex vivo measurements, following PVC, the p-value increased ($p = 0.0028$), indicating a lack of evidence for systemic bias once PVC is applied. The Intraclass correlation (ICC) between in vivo and ex vivo uptake increased from 0.44 to 0.84 after PVC, with a larger ICC (closer to one) representing smaller error

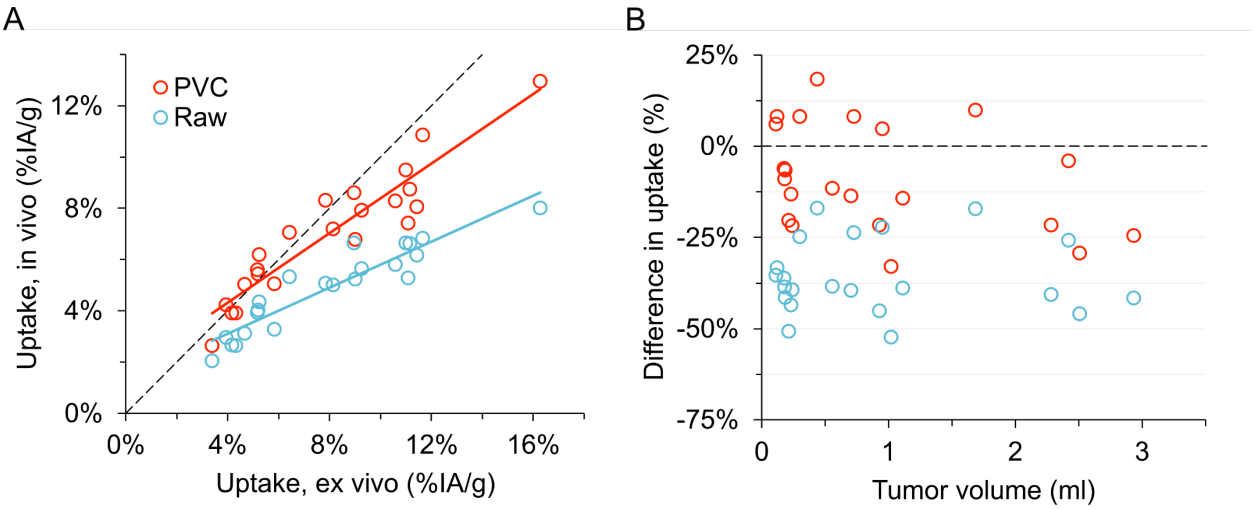

Figure 12: Impact of PVC on in vivo uptake measures relative to ex vivo. (A) Tumor uptake of ^{86}Y-NM600 approximately 72 h after injection as measured in vivo and ex vivo. In vivo uptake is shown without (blue) and with (red) PVC. The black-dashed line represents 1:1 measure of in vivo and ex vivo uptake. (B) The difference between in vivo and ex vivo uptake for raw and PVC relative to tumor volume.

between in vivo and ex vivo measurements. These two metrics combined provide evidence of increased reproducibility of this PVC approach.

Notably, the PVC in vivo uptake of the 7 largest tumors (> 1 ml) were -18.0 ± 15.0% different from ex vivo measurements, compared to -5.0 ± 12.7% for the remaining 15 tumors. Given the visible presence of local necrotic regions in some of these larger tumors, the distribution of ^{86}Y-NM600 uptake was more heterogeneous than that of the tumors less than 1 ml. This was partially accounted for by excluding visible necrotic regions in the contours drawn for in vivo analysis, but it was impossible to completely correct for these regions. As such, measured volume in contours for these large tumors is likely overestimated, leading to application of lower RC factors, and the heterogeneous activity distribution deviates from the assumed uniform uptake in the RC model.

3.2.3 Impact of RC-based PVC on preclinical tumor dosimetry

Accounting for the PVE in ^{86}Y recovery in theranostic dosimetry for ^{90}Y is detailed in Figure 13. As the ratio of background activity to tumor activity varies over the course of the imaging series, the amplitude of PVC is shown to vary over the course of the imaging series. The peak PVC is exhibited at the time of peak uptake, 48 h, before plateauing and/or decreasing thereafter (Figure 13B). The difference between the cumulative absorbed Rx dose of each approach primarily varies in the first 72 hours before following a purely radioactive decay from the final timepoint to infinity. For this representative case, the maximum dose rate is observed on day 2 at 0.319 Gy/MBq/d (or 0.53 Gy/MBq/d with PVC).

The two tumors with the highest uptake, Panc-02 and EL-4, were estimated to receive a mean Rx dose from ^{90}Y-NM600 of 1.85 ± 0.42 Gy/MBq and 2.09 ± 0.05 Gy/MBq, respectively (Table 5). However, the tumor experiencing the highest Rx dose was HUT-102 at 2.18 ± 0.16 Gy/MBq. Given the mean tumor volumes of 2.58 ± 0.50 ml for HUT-102, 0.17 ± 0.07 ml for Panc-02, and 0.91 ± 0.20 ml EL-4, this behavior is to be expected since larger tumor volumes will have a higher SAF for ^{90}Y than smaller tumor volumes. Accounting for PVC, Panc-02 and EL-4 tumors were again estimated to receive the highest Rx doses at 3.00 ± 0.69 Gy/MBq (+62.8%) and 3.07 ± 0.11 Gy/MBq (+47.3%), respectively. HUT-102 continued to receive a high dose following PVC (2.91 ± 0.24), but the impact of PVC was more subdued with an increase of only 33.7%. Overall, the increase in predicted Rx dose from PVC ranged between 33.7% to 62.8%.

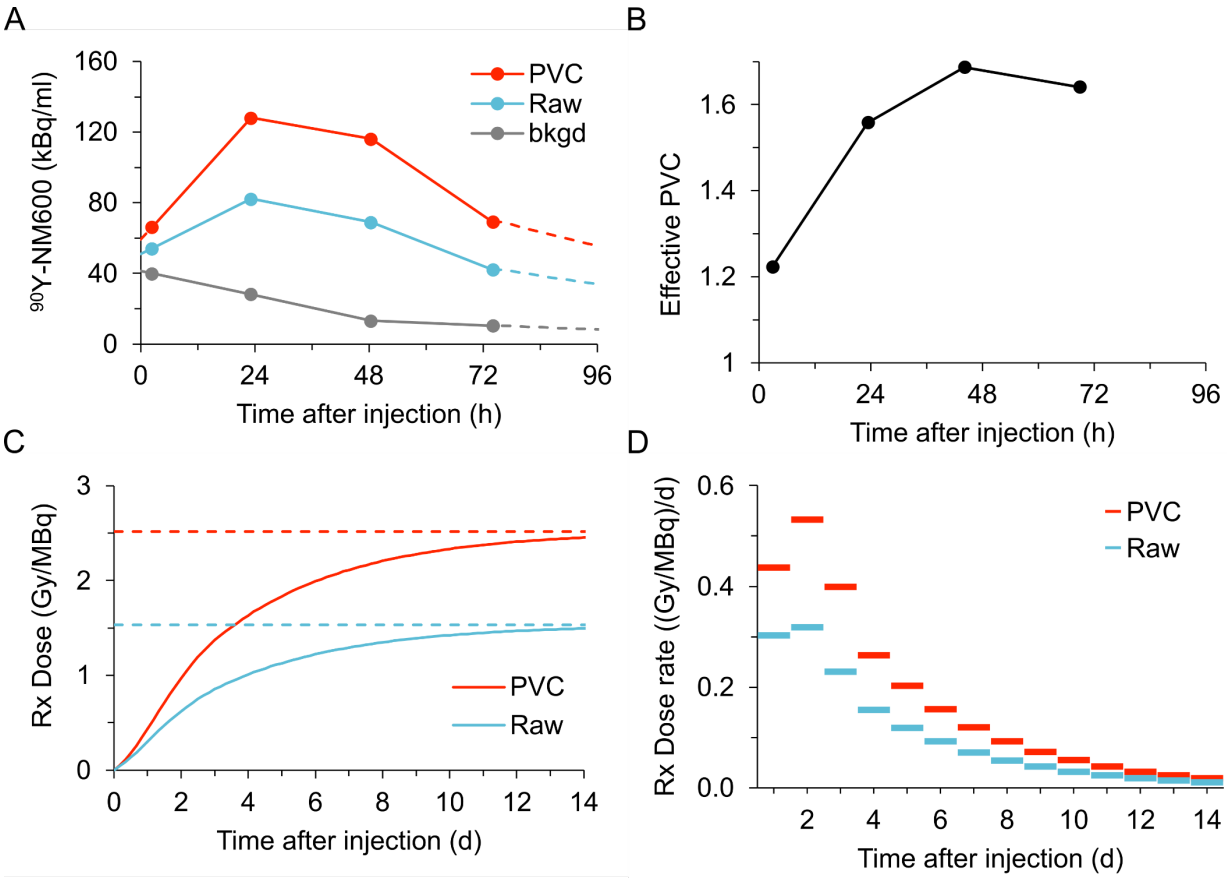

Figure 13: Application of PVC to tumor dosimetry for a single subject from the Panc-02. (A) Projected uptake of ^{90}Y-NM600 with and without PVC. Uptake in adjacent nonspecific tissue shown for context. (B) Effective PVC factor applied at each imaging timepoint. (C) Cumulative Rx dose over the course of 2 weeks post-injection. Dashed lines represent Cumulative Rx dose calculated out to $t = \infty$. (D) Cumulative Rx dose delivered over the course of each day post-injection.

Table 5: Subject specific tumor dosimetry for ^{90}Y-NM600 in tumor bearing mice with and without RC-based PVC applied.

Cell line	Rx Dose, raw (Gy/MBq)	Rx Dose, PVC (Gy/MBq)	Difference
B78	0.97 ± 0.20	1.43 ± 0.36	47.2%
Panc-02	1.85 ± 0.42	3.00 ± 0.69	62.8%
LLC	1.22 ± 0.35	1.79 ± 0.46	47.0%
MyC-Cap	2.04 ± 0.26	2.82 ± 0.22	38.1%
El-4	2.09 ± 0.05	3.07 ± 0.11	47.3%
HUT-102	2.18 ± 0.16	2.91 ± 0.24	33.7%
HCT-116	1.61 ± 0.19	2.29 ± 0.32	42.7%

The underestimation of Rx dose due to PVEs leads to overestimation of dose-response and, in the context of prospective dosimetry and treatment planning, over-dosing of tumors in low-dose ^{90}Y-NM600. The overdosing of tumors in low-dose ^{90}Y-NM600 RPT is further compounded by the fact that small metastatic lesions, with stereotypically low SAF, are overtly impacted by PVEs and most likely to be the least-dosed tumor target in a patient. As such, the translation of PVC in clinical applications of theranostic ^{86}Y/^{90}Y-NM600 dosimetry is essential for accurate delivery of low-dose ^{90}Y-NM600 RPT.

3.2.4 Characterizing the spatially varying ^{86}Y PSF in a GE Discovery MI scanner

The FWHM values resulting from 3D gaussian fitting of the point source measurements at each position are shown in Figure 14 plotted against radial distance from the center of the scanner FoV. Axial and tangential resolution maintains relative constancy over the FoV with gradual increases towards the distal edge at 20 cm (4.57 to 4.74 mm and 3.89 to 4.49 mm, respectively) while the radial resolution increases significantly towards the edge of the FoV (3.83 to 8.43 mm). The magnitude and respective trends shown here compare well to results reported by Chicheportiche et al. who assessed the FWHM of an ^{18}F point source response in the Discovery MI scanner across multiple institutions (*212*). At the center of the FoV, the FWHM dimensions of the measured ^{86}Y PSF were 1.8%, 3.7%, and 11.5% greater than that of ^{18}F in the radial, tangential, and axial dimensions. Further on the periphery of the FoV at a radial distance of 20 cm, the radial and tangential FWHM dimensions increased to 10.1% and 7.6% greater than that of F-18. Notably, the difference between axial dimensions of the ^{86}Y and ^{18}F PSF decreased from 11.5% to 3.8%.

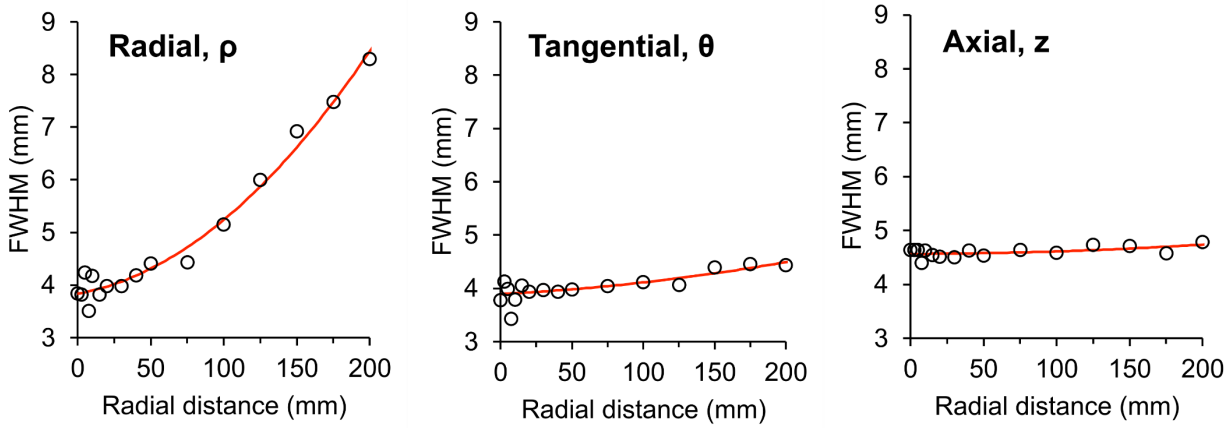

Figure 14: FWHM of the 3D gaussian representation of the ^{86}Y PSF as a function of radial distance from the center of the FoV. Red line depicts 2nd order polynomial fit.

3.2.5 Optimization of iterative deconvolution PVC

The VPHD-LR approach was applied to the clinical Jaszczak phantom study and results analyzed through 30 iterations, using the six hot-spheres (0.5 to 16 ml) as tumor models. The impact of progressive iterations was assessed using C_{err}, ΔC_{err}, PVC_{err}, and ΔPVC_{err} as previously defined and is shown in Figure 15. C_{err} drops significantly in the first few iterations before settling into a quasi-stable plateau. For the three smallest sphere sizes, 0.5 to 2 ml, C_{err} begins to increase after 15-20 iterations as the image becomes increasingly distorted due to excessive deconvolution. The rate of change of this factor, ΔC_{err}, shows this behavior more clearly with pixel values beginning to oscillate about stable pixel values after 10-12 iterations. Further iterative deconvolution beyond this point is unnecessary and, as such, a stopping criterion of $\Delta C_{err} < 20\%$ was chosen. This is supported by analysis of the PVC_{err} which begins to plateau after 5-8 iterations, beyond which ΔPVC_{err} decreases to than 0.5%. Beyond 8-12 iterations, ΔPVC_{err} falls below 0.1%.

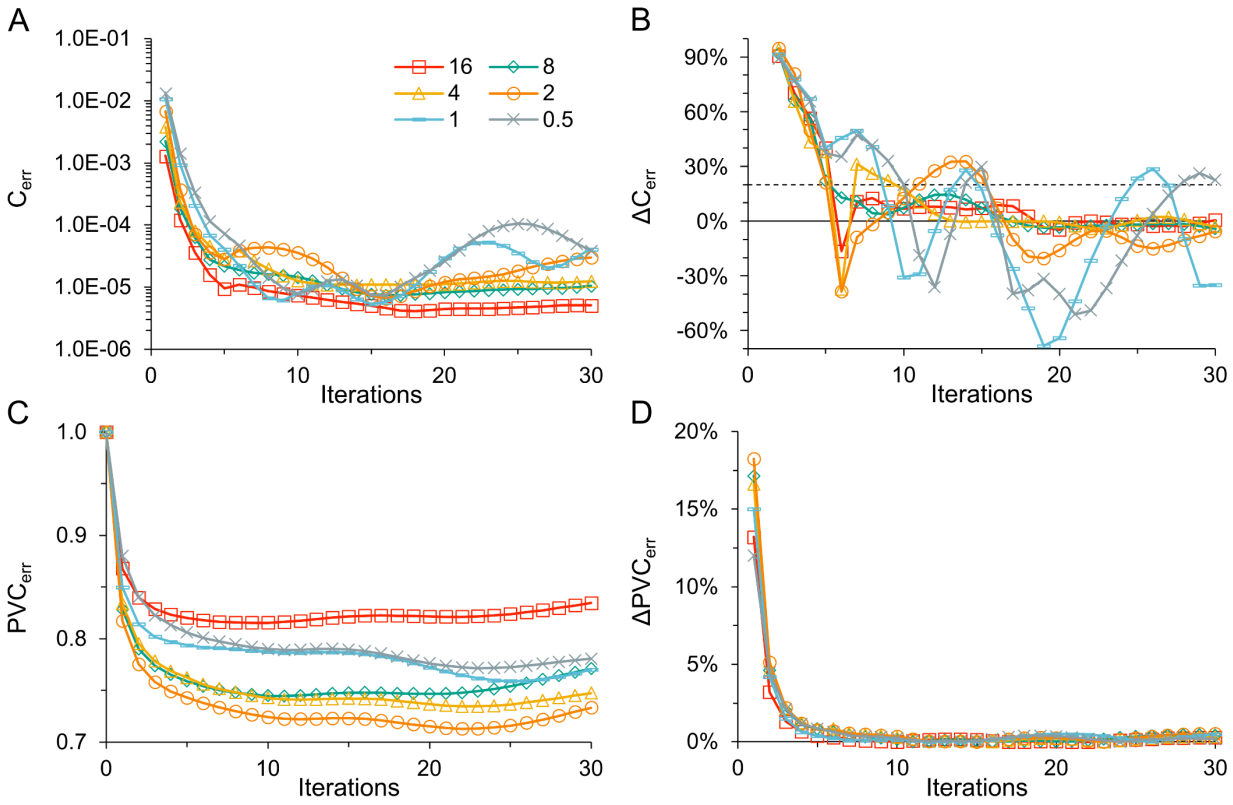

Figure 15: Analysis of LR iterative deconvolution on Jaszczak hot sphere phantom study (volumes 0.5 to 16 ml) and establishment of a stopping criterion. (A) Sum of square differences between a matrix of ones and the multiplicative correction matrix applied at each iteration. (B) The rate of change of C_{err} between each iteration. Dashed line shows stopping criterion at $\Delta C_{err} < 20\%$. (C) Normalized sum of square differences between the deconvolved PET image and a reference image with known activity concentrations as well as the (D) rate of change of this error. All metrics determined from voxels within the tumor ROI.

3.2.6 Clinical implementation of iterative deconvolution-based PVC for small lesions.

The impact of the developed VPHD-LR approach on quantitative PET evaluation of tumor models was assessed against VPHD and VPHD-S models in two phantom studies. Figure 16 shows a comparison of the PET imaged Jaszczak phantom with and without PSF modeling using VPHD-S or VPH-LR. For large spheres, the VPHD-S approach exhibits a pronounced ringing effect where signal near high gradient edge of the sphere is amplified while signal in the center of the sphere remains cold. The effect is somewhat apparent in the original VPHD reconstruction at the largest sphere volume, but the VPHD-S and, to a lesser extent, VPHD-LR amplify this characteristic. Notably, the VPHD-LR approach performs significantly better than VPHD or VPHD-S in sphere volumes less than 2 ml (15.6 mm in diameter). The locoregional approach of VPHD-LR can be seen here as well with the difference between the original VPHD and VPHD-LR image being zero outside of the 2 cm margin expanded ROIs.

Recovery of ^{86}Y activity in uniform hot spheres in the Jaszczak phantom was assessed for each PVC approach using contours drawn on the CT image. Contours were adjusted to match known sphere volume with the averaged difference between ROI volume and sphere volume being -6.6 ± 2.1%. The activity concentrations measured from samples of the hot sphere and background solutions of ^{86}Y were 59.40 ± 0.29 kBq/ml and 5.85 ± 0.03 kBq/ml, respectively (ratio of 10.1:1). Figure 17 shows RC for each approach plotted against sphere size. The highest RC factors are observed for the largest sphere volumes with 0.688 for VPHD, 0.703 for VPHD-S, and 0.716 for VPHD-LR. At smaller sphere volumes, VPHD-LR outperforms reconstruction via VPHD and VPHD-S with a RC of 0.389 being over 17.8 % greater than that of VPHD and VPHD-S. As can be seen in Figure 17B, VPHD-LR outperforms VPHD-S across all sphere volumes with VPHD-S demonstrating recovery of ^{86}Y equal to or less than that achieved with VPHD at 1 ml sphere

volumes (12.4 mm in diameter). The parameters of the sigmoidal best fit line to the RC curves for each reconstruction approach in Figure 17 are shown in the Table 6 below.

Table 6: Parameters from Equations 9 describing the best fit line of RC against sphere diameter (mm).

Fitting parameter	VPHD	VPHD-S	VPHD-LR
a	15.58	14.81	13.10
b	1.316	1.379	1.226

The dosimetric impact of the PSF modeling approaches were investigated by performing theranostic dosimetry to predict the dose distribution of ^{90}Y in the Jaszczak phantom. Line profiles through each sphere showing the difference between activity concentration and dose are shown in Figure 18. The difference between the true and PET-imaged mean dose estimates ranged between -25.2% to -56.0% for VPHD, -23.6% to 56.1% for VPHD-S, and -22.6% to -49.7% for VPHD-LR in spheres ranging in volume from 16 to 0.5 ml. The improvement in dose attained with VPHD-LR and VPHD-S reflected that of Figure 17B with VPHD-LR ranging between 3.5% to 11.9% and VPHD-S 2.1% to 4.8% for sphere of size 1 ml to 16 ml. At 0.5ml, VPHD-LR was 14.2% greater than that of VPHD while VPHD-S returned results similar to that of VPHD (-0.4%).

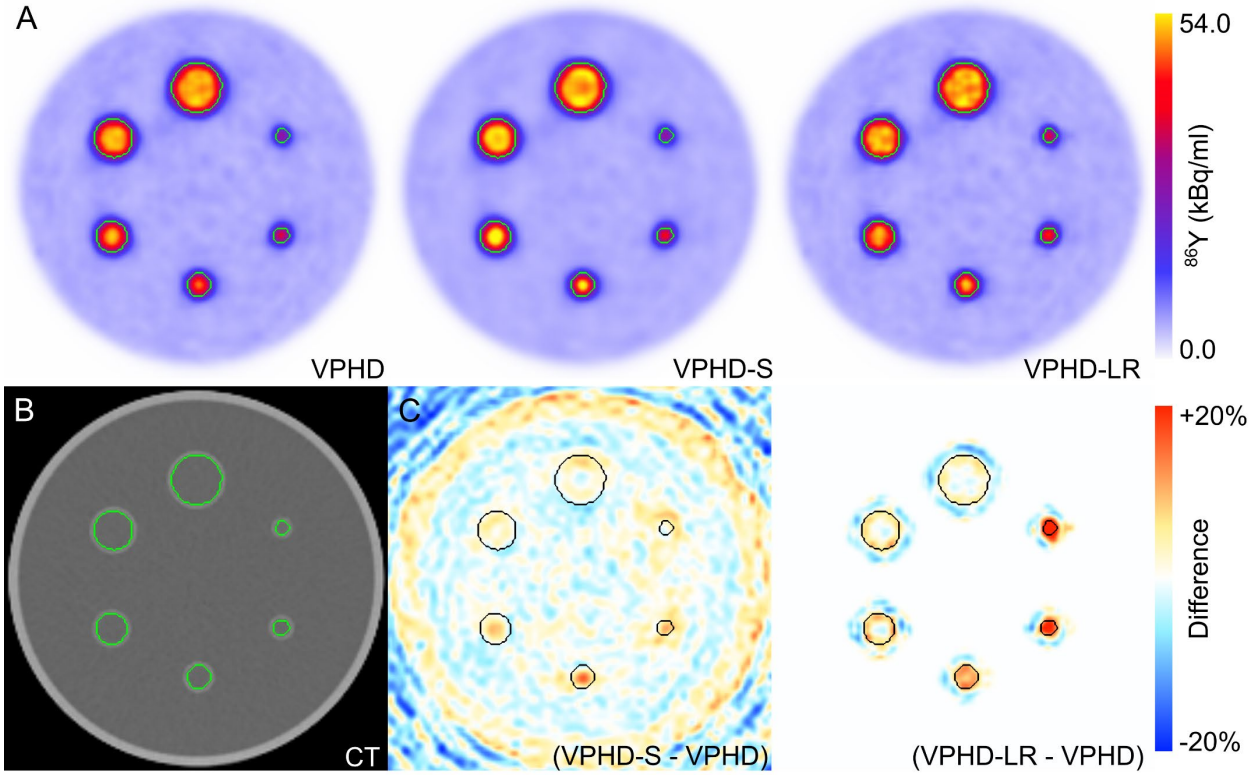

Figure 16: (A) Axial slices of PET images from Jaszczak phantom study shown with (VPHD) and without (VPHD-S and VPHD-LR) PSF modeling. Source to background ratio was 10:1. (B) CT image with contours (green) shown for each individual sphere. (C) Difference maps between PET images showing the impact of VPHD-S and VPHD-LR on the hot sphere recovery.

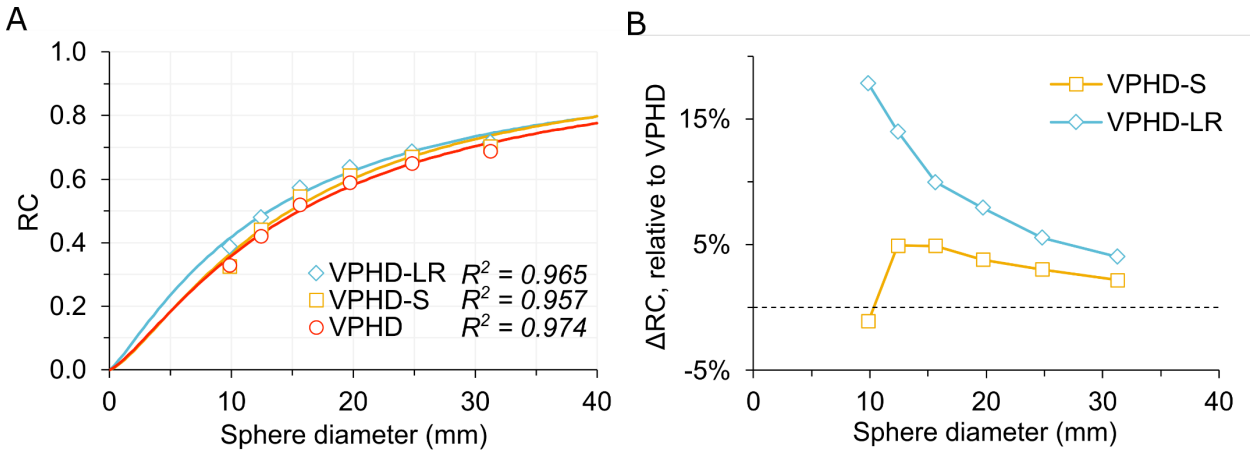

Figure 17: Recovery of ^{86}Y in hot spheres with a 10:1 source to background ratio. (A) VPHD, VPHD-S, and VPHD-LR approaches are shown with each datapoint representing a sphere measurement as well as a best fit line to a sigmoidal function. (B) Relative improvement in calculated RC for PSF modeling approaches VPHD-S and VPHD-LR relative to VPHD. Dashed line shows 0% difference.

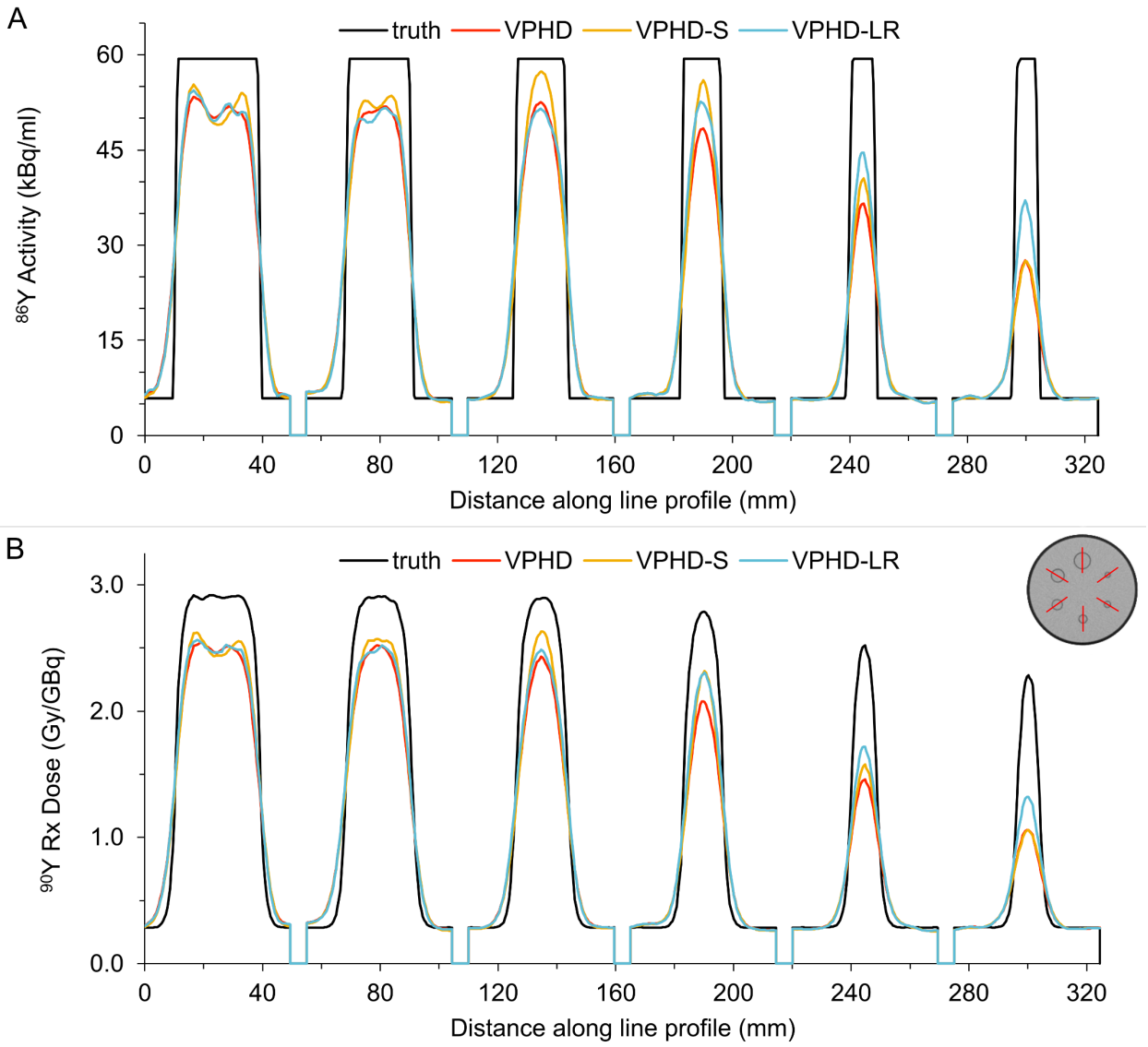

Figure 18: Line profiles over each sphere showing the difference between VPHD, VPHD-S, VPHD-LR, and the true distribution for (A) ^{86}Y activity concentration and (B) ^{90}Y Rx Dose. Axial slice of CT image with red lines depicting line profiles through spheres is shown middle-right of the figure for reference.

Following Monte Carlo simulations, the functional differences between the true distribution and PET imaged distributions are reduced. For the largest sphere, the ratio of the VPHD PET imaged distribution to the true distribution (i.e. the RC for activity) within the 16 ml sphere is 0.688 for activity and 0.748 for dose, an 8.7% difference. At a sphere size of 0.5 ml, this difference increases to 33.3%. Thus, while the application of the RC factor will correct the mean activity concentration in the ROI of a PET image, that same factor will overcorrect the mean dose from that same PET imaged activity distribution. In this work we've characterized three key factors that, when corrected for, account for these discrepancies.

The three factors that contribute to the recovery of dose for theranostic $^{86}Y/^{90}Y$ dosimetry estimates (Equation 16) are summarized in Figure 19. The contribution from background activity surrounding the sphere is purely dependent on geometry and is plotted against sphere volume. The factor calculated in Figure 19A is normalized by $1.47x10^{-10}$ (Gy/s)/(Bq/ml), which is the dose conversion factor for a uniform distribution of ^{90}Y. To determine the contribution to a mean dose estimate in a tumor, a sample of the background activity, in (Bq/ml), surrounding the target volume must be acquired to apply this factor. The second factor contributing dose to a spherical tumor in a PET imaged activity distribution is sourced from the spill out activity from the ROI. As the tumor volume becomes smaller, this factor becomes more dominate as a percentage of the total dose (D) in the ROI. While it is true that different tumor volumes produce different RC factors for a given tumor volume, the spill out activity for a given RC factor is approximately the same between VPHD, VPHD-S, and VPHD-LR. As such, a single best fit line was determined based on the collection of all reconstruction approaches as a factor of the total mean dose to the ROI in the phantom study. The third and final factor accounts for the differences in self-absorbed fraction (SAF) from a uniform and PET-imaged activity distribution. Compared to a uniform activity

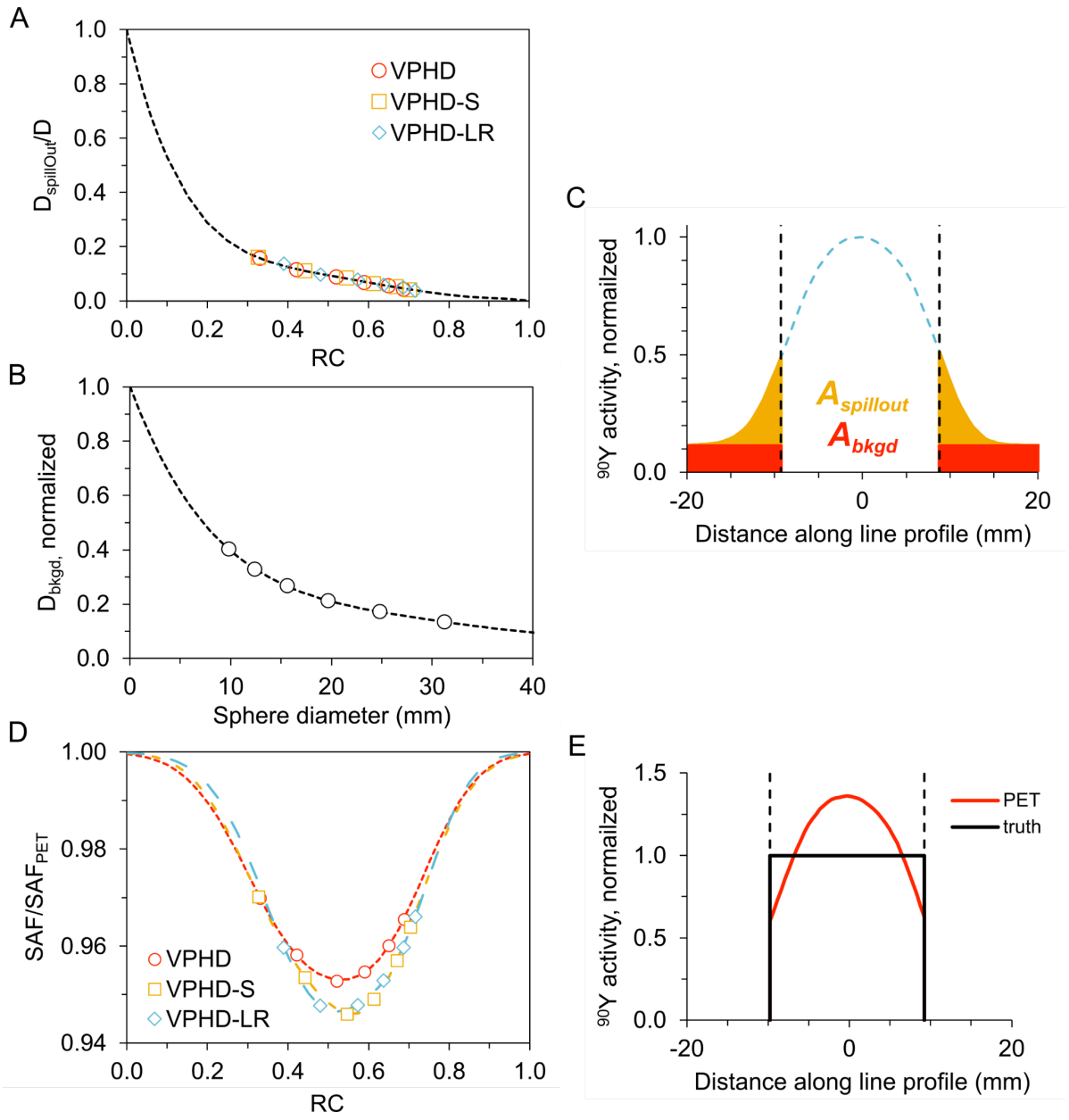

Figure 19: Contributions to the mean dose in a spherical tumor volume from a PET imaged activity distribution. (A) Dose contribution from spill-out activity that appears outside of the sphere volume plotted against RC and normalized by D, the total dose in the sphere. (B) Dose from background activity is plotted against sphere diameter because it is independent of PET image reconstruction. Dashed line represents a 5th order polynomial fit. (C) Profile of PET-imaged activity in a spherical tumor volume where spill out and background activity, as modeled in these correction factors, are highlighted. (D) The ratio of self-absorbed fractions produced from the true (homogeneous) and PET imaged activity distribution within the ROI. Dashed line represents a two-term gaussian best fit line to each reconstruction approach. (E) Profile of uniform and PET-imaged activity distributions of equal cumulative activity within the defined sphere volume.

distribution, a PET-imaged activity distribution with the same mean dose will have activity preferentially located central to the sphere volume. As such, less dose will be deposited from the decay of ^{90}Y outside of the sphere. Therefore, the SAF for a PET imaged activity distribution will be higher than that of the true uniform distribution. The impact of this SAF heterogeneity correction factor is maximal at the point where dose uniformity is lost at the center of the sphere (i.e. maximum dose in the sphere no longer plateaus and begins to decrease).

The difference in mean dose to sphere volumes from the true and PET-imaged activity distributions is shown in Figure 20. Without any correction, the dose difference between the PET imaged activity distribution and the true activity distribution ranged between -22.6% to -56.2% with the difference growing as sphere volume decreased. The overcorrection of mean dose from simple multiplicative application of the inverse of the RC factor is shown in Figure 20B. The difference at the largest tumor volume, 16 ml, was <10% but grew up to 34.2% at a sphere size of 0.5 ml. The dose difference between mean dose to spheres following full application of correction factors (Equation 16) is shown in Figure 20C. Across all sphere sizes, the difference in mean dose ranged between -0.08% and 0.16%. Considering that the standard deviation of the mean voxel-level difference ranged between 3.5% and 9.3%, the proposed methodology serves as a good template for achieving accurate theranostic ^{86}Y/^{90}Y dosimetry estimates in small lesions.

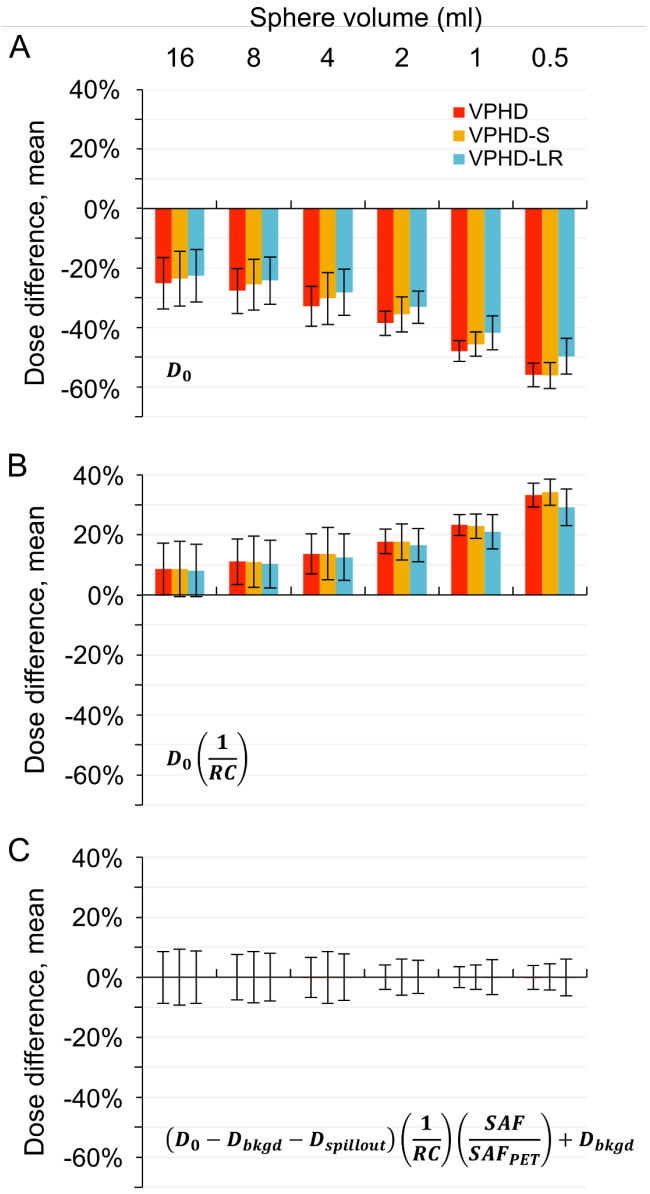

Figure 20: The difference between the true and PET imaged mean ^{90}Y dose to spheres in the Jaszczak phantom study. (A) Dose difference of the raw, uncorrected, PET imaged dose distribution (D_0). (B) Dose difference after correcting for the RC of each sphere volume. (C) Dose difference following full correction of the mean dose using Equation 16. Error bars shown in all plots represent standard deviation of the mean of voxel-level dose-differences.

3.2.7 Iterative deconvolution-based PVC in heterogeneous PET

The developed iterative deconvolution approach was also evaluated in the setting of heterogeneous PET uptake in a necrotic tumor model using a novel gradient phantom. Figure 21 shows an axial slice of the gradient phantom using VPHD, VPHD-S, and VPHD-LR reconstruction approaches. A comparison of the VPHD-S and VPHD-LR approaches in this setting showcases the limitations of each approach. The VPHD-S approach provides a conformal uniform boost in activity near the high gradient distal edge of the phantom. In contrast, the post-reconstruction VPHD-LR approach amplifies the signal present in the VPHD image, leading to less conformal distribution along the edge of the phantom. This can be attributed to the advantages afforded to the VPHD-S algorithm performing PSF modeling within the reconstruction process. However, the differences between the VPHD-S and VPHD-LR approaches are still evident. In the difference map between the VPHD and VPHD-S images, the boost in signal is preferentially skewed towards the high gradient outside edge of the phantom rather than the center of the compartment, as would be expected. This behavior is indicative of a mismatched PSF model that is smaller than the true PSF. As such, the PSF modeling in this setting underestimates the extent of the spill-in/out effect and is unable to sufficiently restore signal distant to the high gradient edge of activity. This can most clearly be observed when comparing the difference maps of VPHD-S and VPHD-LR at the intersection of the necrotic core and hot outer shell of the phantom. Here, the VPHD-LR approach outperforms VPHD-S in boosting activity in regions of spill-out and dampening activity where spill-in occurs. Because the gradient between these two regions is smaller, the VPHD-S approach is unable to adequately recognize the discontinuity in the underlying activity distribution.

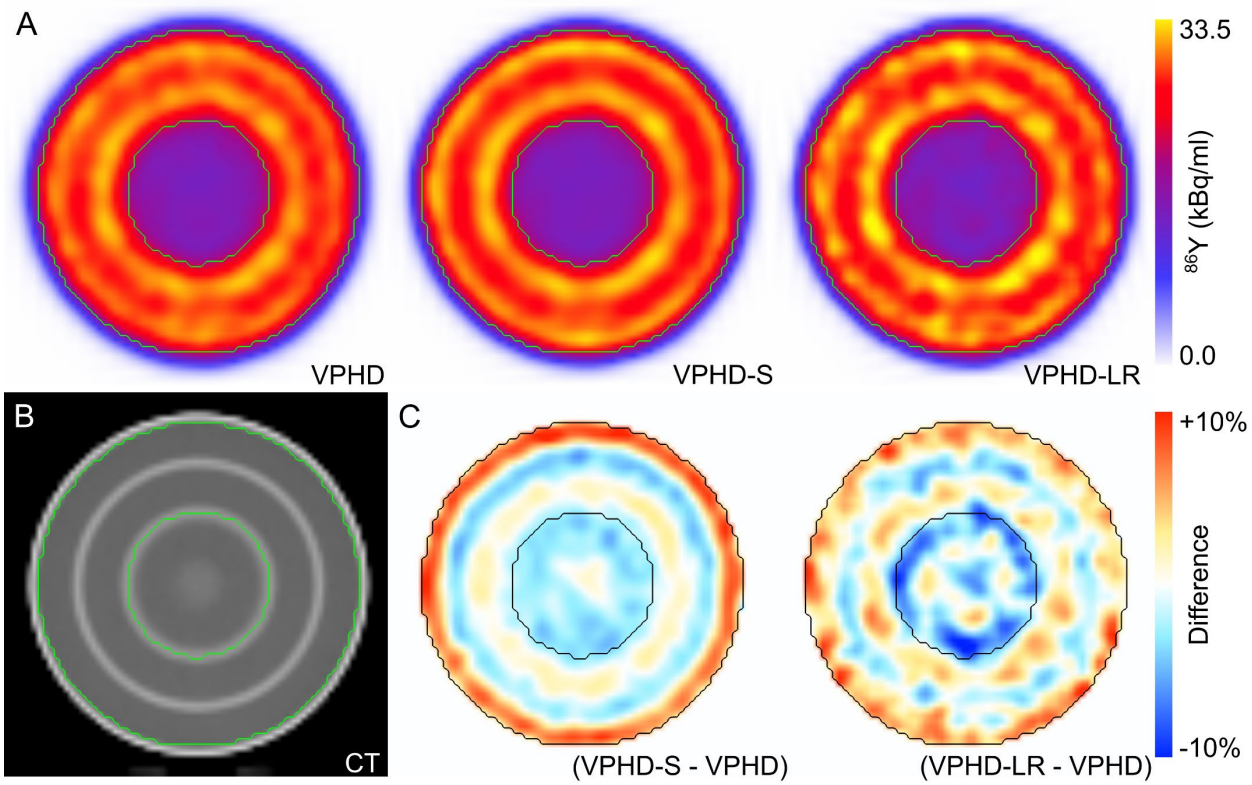

Figure 21: (A) Axial slices of PET images from gradient phantom study shown with (VPHD) and without (VPHD-S and VPHD-LR) PSF modeling. The ratio of activity between the two innermost and outermost shells was 2:1. (B) CT image with contours (green) shown delineating the two innermost and outermost active regions. (C) Difference maps between PET images showing the impact of VPHD-S and VPHD-LR on the hot sphere recovery.

The mean voxel-level difference between the true and PET imaged activity distributions within an ROI encompassing all shells was -22.8 ± 11.1% for VPHD, -22.0 ± 10.6% for VPHD-S, and -21.6 ± 10.8% for VPHD-LR. The improvement made by VPHD-S and VPHD-LR over VPHD was 3.2% and 5.0%, respectively. Relative to VPHD, the cumulative activity observed within the PET-imaged gradient phantom was improved by 1.2% with VPHD-S and 1.8% with VPHD-LR.

Further analysis of the dosimetric impact of the developed approaches is shown in Figure 22. A comparison of the PET image-based dose distributions are shown relative to a distribution of the true dose, normalized for the total activity observed in the VPHD PET image of the gradient phantom. In this case, the total activity measured in the gradient phantom was 11.02 MBq whereas

the total activity observed within a whole-phantom mask of the gradient phantom was 9.19 MBq. For comparison, the true activity distribution is also shown normalized by a factor of 0.834 to match the measured activity within the phantom. In a comparison of the dose volume histograms of the PET imaged distributions, the variations become more apparent. Compared to the normalized true results, the PET image-based dose distributions exhibit similar trends but produce a more sloped penumbra, indicative of a heterogeneous dose distribution, in the high dose regions. The cumulative DVH shows that the developed VPHD-LR approach produces more accurate estimates of voxel level dose in low- and high-dose regions within the phantom. Notably, D_{50} for all PET image-based approaches arrive at similar values despite the variation observed elsewhere in the curve. As observed in the PET images, the VPHD-S approach differs significantly from the VPHD-LR results. The cumulative DVH for VPHD-S and VPHD-LR follow identical paths through moderate dose but begin to deviate at high doses with VPHD-S failing to boost high dose voxels in the tail of the DVH. The mean voxel-level dose difference between VPHD, VPHD-S, and VPHD-LR was -20.2%, -19.4%, and -19.0%, respectively. The improvement achieved over VPHD was 3.7% for VPHD-S and 5.7% for VPHD-LR. At an ROI-mean dose level, the difference relative VPHD was 1.0% and 1.5% for VPHD-S and VPHD-LR, respectively.

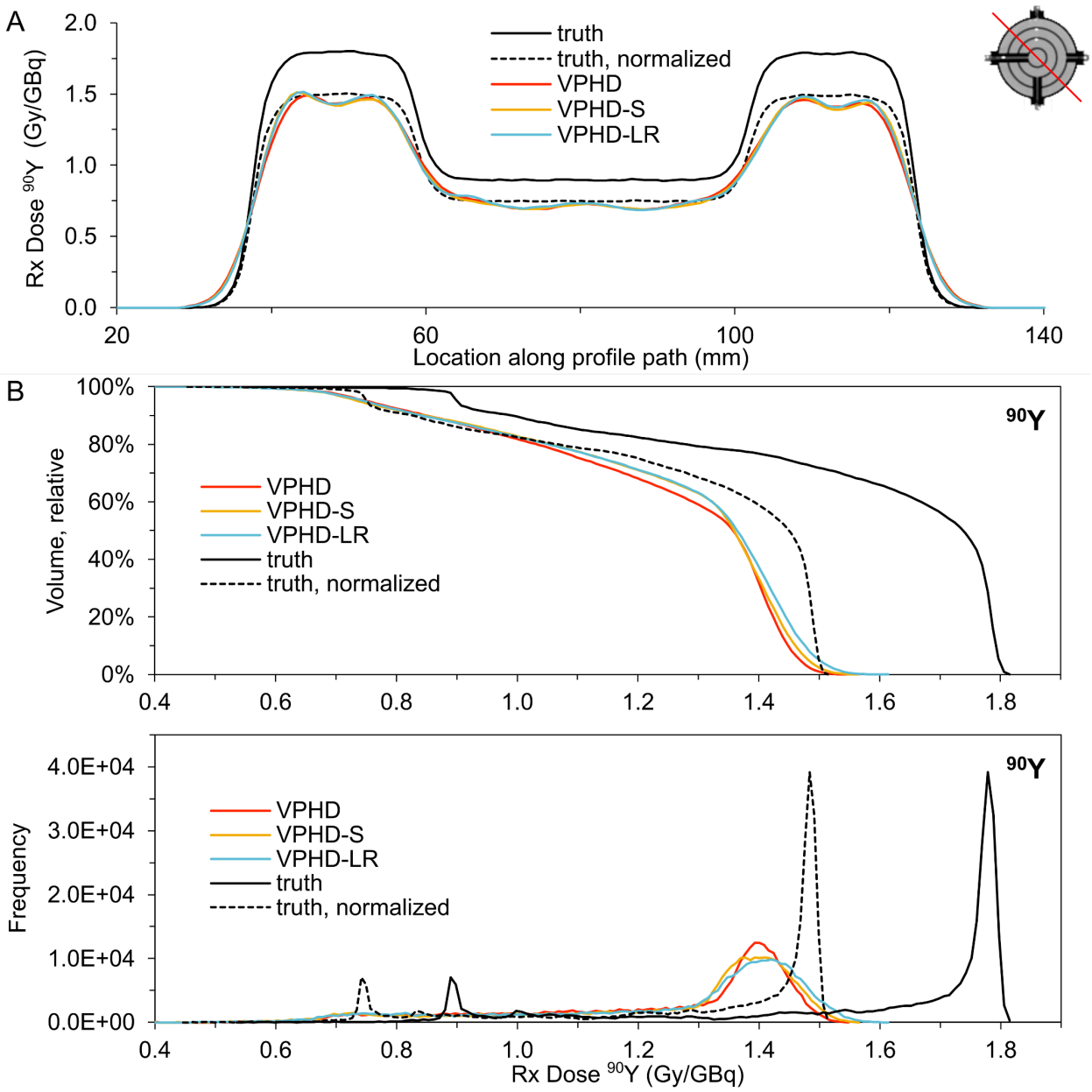

Figure 22: Comparison of the ^{90}Y dose distributions resulting from the true and PET imaged activity distributions of ^{86}Y. (A) Line profile through the center of the gradient phantom. Axial slice from CT image shown with line profile (red) at top right. (B) Cumulative and differential dose volume histograms of the dose distributions. Dashed line represents results from the true activity distribution normalized for the total activity observed in the VPHD PET activity distribution within the phantom.

3.3 Discussion

PVEs in PET imaging have a cascading impact on the quantitative imaging of biomarkers and subsequent theranostic dosimetry. The PVC approaches investigated in this work set out to model this effect and establish region and voxel level corrections to account for these errors. The iterative deconvolution approach developed here is primarily designed to correct heterogeneous PET distributions, but it also works in tandem with region-based RC corrections for small lesion dosimetry. The approach itself, combined with the correction matrix-based stopping criterion, is generalizable to any scanner if the PSF is appropriately modeled for that scanner.

In preclinical tumor models, ^{86}Y-NM600 is shown to target a broad spectrum of cancers with tumor specific uptake and retention alongside primarily hepatobiliary clearance of the agent. However, PVE leads to a significant underestimation of PET-based in vivo uptake with estimates of %IA/g being an average of -36.0% ± 10.1% lower than that of direct ex vivo measurements. Using PVC based on RC measurements from a preclinical PVC phantom study, the error due to PVE was reduced to -9.4% ± 14.4%. These results align with those of Knowles et al (*205*) as well as our previous work with ^{124}I-NM404 (manuscript in-preparation). As a result of these corrections, Rx dose estimates for ^{90}Y-NM600 based on ^{86}Y-NM600 PET imaging increased by an average of 45.6 ± 9.8%. For tumor dose driven efficacy studies, this work suggests that the incorporation of RC for quantitative in vivo uptake measures and dosimetry should be strongly considered.

For heterogenous PET distributions, the applications of region-based RC factors are limited and require robust assumptions about the underlying anatomy and biological functions. Tran-Gia et al. demonstrated the application and dosimetric impact of a multi-compartment PVC model in

a kidney phantom model taking as separate compartments the cortex and medulla (*128*). The application of such models to tumor dosimetry is more difficult given uncertainties in the anatomic extent and underlying physiological uptake behavior for a given agent in a tumor. No reliable assumptions can be made of either characteristic in tumors, which limits voxel-level PVC to PET-based iterative deconvolution approaches. The results observed in the gradient phantom study in this work showcase the limitations of iterative deconvolutions approaches relative to region-based PVC. The VPHD-LR approach developed in this work improved the accuracy of activity and dosimetry estimates by 5% and 5.7%, respectively, compared to VPHD but remained an average of -19.0 ± 6.0% low compared to the true underlying distributions. Notably, the presence of cold walls in the gradient phantom was observable in the PET imaged activity distributions. Berthon et al. suggested that the use of 0.1-0.2 mm diameter walls in phantoms with plastic inserts to improve the quantification of uptake in nuclear medicine studies (*213*). However, the limitations enforced by 3D printing and modeling capabilities required the utilization of a 2 mm wall thickness for this phantom.

The impact of iterative deconvolution approaches still make a substantial impact on the recovery of ^{86}Y in quantitative PET imaging of small lesions. Here, the accuracy of mean ROI-level activity is increased by as much as 17.8% for lesions around 0.5 ml is size (9.85 mm in diameter). However, the analysis of sub-centimeter lesions in PET with PSF modeling is controversial. Munk et al. (*214*) argued that the variable behavior of ^{18}F imaged lesions reconstructed with SharpIR PET reconstruction (VPHD-S) at this size range require substantial post-filtering to be considered quantitative. An example of this behavior can be seen in the line profiles of Figure 18 where VPHD-S produced PET distributions overcorrect PET activity beyond what is observed as the maximum activity in larger spheres. However, this behavior is not observed

with the developed VPHD-LR approach. This is the case despite the VPHD-LR approach outperforming VPHD-S at smaller lesions sizes. However, care should still be taken with analysis of small lesions, as corrections from RC begin to more than double the signal observed in the PET activity. In this work, failure to recover the maximum PET signal in spheres occurs at 2 ml (15.6 mm diameter) for VPHD and 1 ml (12.4 mm diameter) for VPHD-S and VPHD-LR. This coincides with the general rule of thumb that suggests that lesions less than 2-3 times the FWHM of the spatial resolution of the scanner are dominated by PVEs (*160*). Based on PSF measurements in this work, that theoretical limit occurs for ^{86}Y between 7.8 to 11.7 mm at the center of the FoV.

3.4 Acknowledgements

As part of a rich collaborative research environment, I would be remiss to not acknowledge those who assisted in the completion of the aforementioned work. Eduardo Aluicio-Sarduy and committee member Jonathan Engle of the Cyclotron Gang performed the on-site production of ^{86}Y for use in ^{86}Y-NM600 and phantom studies. Reinier Hernandez and committee member Jamey Weichert provided radiolabeled ^{86}Y-NM600 and ^{90}Y-NM600 for use in preclinical and clinical investigations. Ravi Patel and Peter Carlson of committee member Zach Morris's and Paul Sondel's Labs assisted with mouse handling and data collection. I would like to thank the Small Animal Imaging and Radiotherapy Facility (SAIRF) for its assistance in preclinical investigations. Justin Jeffery designed the 3D printed PVC and gradient phantoms used in this work and assisted with preclinical PET-CT imaging. Tyler Bradshaw, Reinier Hernandez, and Justin Jeffery assisted with phantom preparation. Joe Grudzinski assisted with the implementation of RAPID in preclinical mouse models and development of ROI-level PVC methodology. Paul Harari and The Ride Student Scholar award provided funding and support in the initial development of ROI-level PVC in preclinical tumor models. Finally, committee member and advisor Bryan Bednarz provided guidance, funding, and discussion towards the completion of this work. Methodology pertinent to ROI-level PVC in this chapter has been edited slightly from a manuscript regarding the application of PVC in theranostic dosimetry of ^{124}I/^{131}I-NM404 in preclinical models of head and neck cancer that has recently been submitted for publication*. Additionally, methodology and results relating to preclinical investigations of ^{86}Y-NM600 in tumor bearing mice has been edited slightly from a recent co-authored publication (*17*).

*Marsh IR, Li C, Grudzinski J, Jeffery J, Longhurst C, Adam DP Hernandez R, Weichert JP, Harari PM, Bednarz BP. Partial volume correction improves theranostic ^{124}I/^{131}I-CLR1404 tumor dosimetry in xenograft models of head and neck cancer. Submitted 2021.

Chapter 4

Temporal Coregistration in Multi-Timepoint Internal Dosimetry

The spatial information gained from 3D imaging approaches in nuclear medicine such as PET and SPECT has proven invaluable for characterizing the localization of molecular imaging agents in vivo (*215*,*216*). For multi-timepoint imaging involved with theranostic dosimetry, the biggest challenge lies in finding a way to leverage both the temporal and spatial information offered by serial PET-CT or SPECT-CT imaging. Therefore, accurate coregistration of each voxel in a target region over the course of serial imaging is imperative for accurate dosimetry. Unlike conventional radiotherapy where approaches for consistent patient setup and positioning between imaging and radiation delivery is well established and the use of immobilization devices are commonplace to ensure that dosimetry is representative of the delivered dose (*129–131*), these patient positioning and immobilization strategies are rarely used in molecular imaging. As a result, more advanced

registration strategies are needed to achieve accurate characterization of tracer uptake for theranostic dosimetry. Specifically, targeted temporal coregistration strategies need to be employed to ensure spatiotemporal accuracy of dosimetry estimates in select regions of interest. In this chapter we explore the impact that different coregistration strategies have on theranostic $^{86}Y/^{90}Y$-NM600 tumor dosimetry. Within this context we will also investigate the influence of target volume definition, as defined from the overlap of coregistered ROIs, on prospective dosimetry estimates.

4.1 Methods and Materials

4.1.1 Multi-timepoint internal dosimetry approaches

The theranostic dosimetry approach employed in the RAPID workflow is described for preclinical tumor dosimetry in section 3.1.5. The same approach is employed in the clinical setting but with extensions to produce 3D absorbed dose distributions. In both preclinical and clinical dosimetry applications, 3D ADR distributions are produced using the CT and PET images to define the geometry and source distributions, respectively, in Monte Carlo simulations. For preclinical dosimetry where the applications incorporating analysis of 3D absorbed dose distributions are more limited, mean-ADR integrated dosimetry estimates of mean Rx Dose (Gy per injected activity) are provided. In the mean-ADR integral approach, temporal coregistration of the ROIs is not performed. For theranostic dosimetry in clinical applications of this work, the RAPID workflow is extended with automated temporal co-registration approaches to allow for the generation of 3D absorbed dose distributions in a clinically applicable framework.

4.1.2 Locoregional registration

For whole body (WBR) and locoregional (LRR) registration approaches implemented in this work, image volumes from each moving timepoint (t_{mov}) are registered and resampled to the image matrix defined by a single reference timepoint (t_{ref}). The final imaging timepoint was chosen as the reference timepoint due to the superior tumor-specific uptake observed with ^{86}Y-NM600 at late timepoints. Higher specificity in tumor uptake assists physicians in the delineation of the tumor. Additionally, the activity distribution at the final timepoint strongly influences the final dose distribution due to the contributions from the assumed exponential radioactive decay

from the final imaging timepoint. It is therefore advantageous to hold this image frame and associated contour static in the temporal registration process. Once registered to the same image matrix, the ADR distributions within a target ROI are integrated on a voxel level to produce a 3D absorbed dose distribution.

The LRR framework described in Figure 23 is piecewise in nature (*217*). First, the full-size CT image volume at t_{mov} (CT_{mov}) is registered to the CT image volume at t_{ref} (CT_{ref}). CT_{mov} is then cropped down to encompass the maximum extent of a binary mask defined by the target ROI expanded by a set margin size. This cropped version of CT_{mov} is registered to the full size CT_{ref}. The cumulative transformation matrix representing the final LRR result for CT_{mov} is then copied and applied to the binary ROI mask and ADR distribution at t_{mov}. The CT, ROI, and ADR image volumes at t_{mov} are then resampled to the image matrix defined by the cropped version of CT_{ref}. This process is then repeated for each remaining t_{mov} image set. The final product of the LRR framework is then a series of uniquely cropped and registered CT, ROI, and ADR image volumes for each target ROI. For all registration steps, an iterative rigid-affine algorithm based on the correlation between CT image volumes is used. Interpolation for resampling of CT and ADR image volumes employed a Mitchell filter (*218*) while the ROI volumes were resampled using a box filter.

Resampling the final registered image volumes to the cropped version of CT_{ref} reduces the storage required for the LRR framework and increases computational speed in later analysis and implementation of deformable image registration. Additionally, since the unique cropping parameters for each LRR target volume is saved, the final AD distribution within each target ROI can be un-cropped and merged into a single full-size AD image volume for visualization and analysis. For the purposes of visualization, the LRR derived AD distributions are superimposed

into a WBR-derived AD image volume that was produced using the whole-body mask as the target ROI. Note that in cases where abutting ROIs undergo LRR, a final target volume defined by the union of registered ROIs may result in overlap. In order to avoid this, a target volume defined by either the intersection of registered ROIs or simply the ROI at t_{ref}.

In cases where LRR fails, the user has three options to regulate the LRR framework. Firstly, the margin size for a single ROI can be increased or decreased to modulate the impact of surrounding tissue in LRR. As margin size increases, LR registration will produce results similar to that of the WBR. Secondly, the initial step size for the iterative optimization of spatial position in affine LRR may be decreased. This modification can be useful if there is a nearby local minimum that the registration algorithm latches onto, resulting in poor registration of the desired target region. Finally, if CT-CT registration persistently fails, the user has the option to employ ROI-ROI registration that optimizes correlation of ROI_{mov} with ROI_{ref}. While this method discards the wealth of anatomic information from the CT scan, it is extremely useful in cases where significant displacement is observed in the local anatomy. In this approach, a resampled LRR CT_{mov} image volume is still generated and available if further application of DIR is performed.

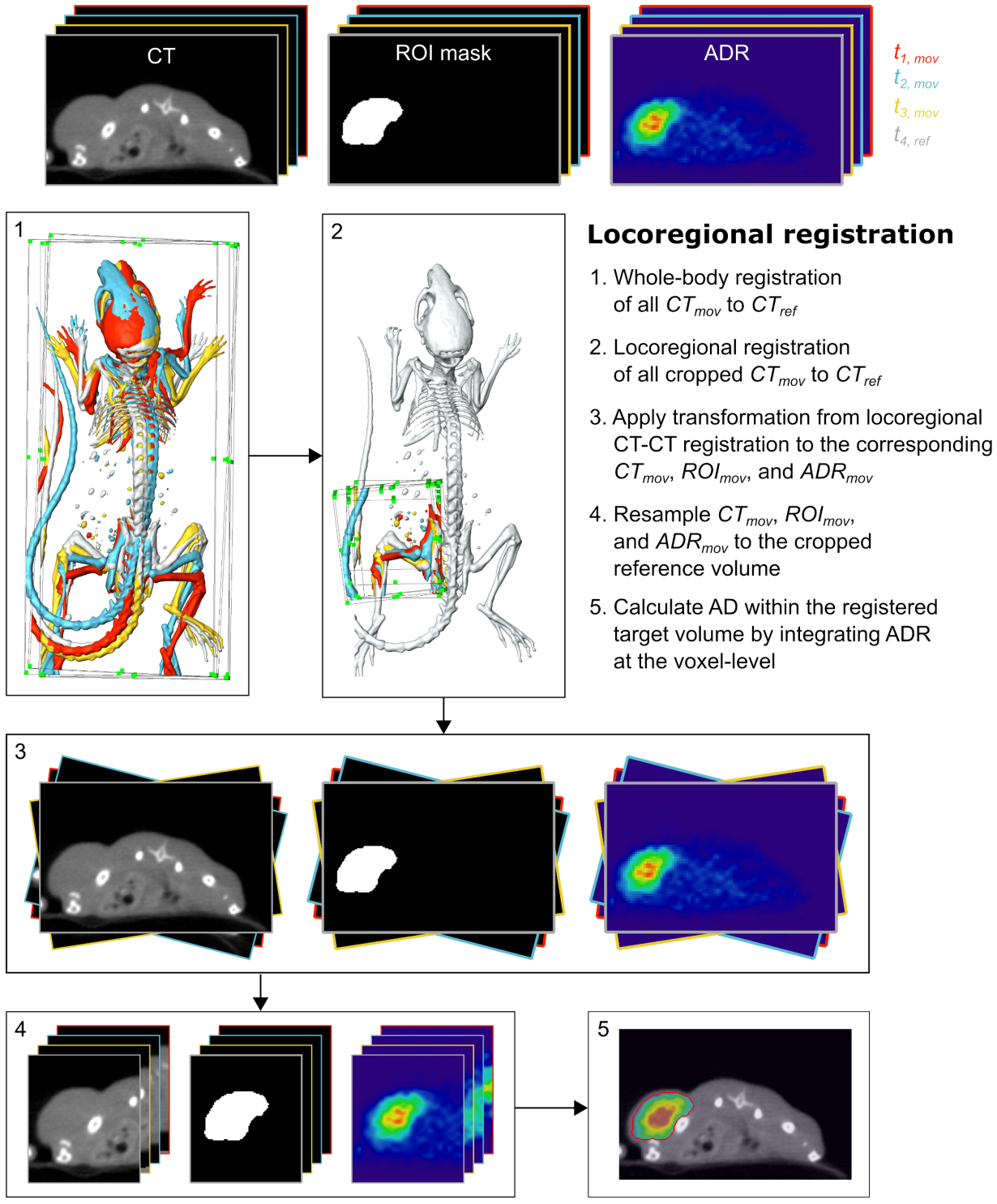

Figure 23: Overview of the locoregional registration framework for a representative preclinical tumor.

4.1.3 Deformable image registration with demons

Deformable image registration (DIR) in this work was performed using a diffeomorphic demons-based registration algorithm developed by Thirion (*219*), improved by Vercauteren,et al. (*220*), and implemented in MATLAB (The MathWorks, Inc., Natick, MA, version 2020b). In its basic form, Thirion's demon's algorithm is an iterative process in which the moving image (I_m) is gradually deformed to match a given static image (I_s). The demons in this setting act as a membrane at each voxel in the static image, generating gradient-based displacement forces ($\vec{d}$) that represent the diffusion of intensity in the moving image:

$$\vec{d} = \frac{(I_m - I_s)\overrightarrow{\nabla I_s}}{\left|\overrightarrow{\nabla I_s}\right|^2 + (I_m - I_s)^2} \qquad 17$$

In this fashion, a displacement field is generated that, when applied to the moving image and interpolated back into coordinate space, creates an updated I'_m that is more similar to I_s than the previous frame. The displacement field at each iteration is then also regularized via simple gaussian smoothing to reduce the impact of noise and ensure local conformity in deformation. The iterative process continues until I'_m converges to a stable solution.

The key aspect of the demon's algorithm is the generation of the vector field at each iteration and how it is manipulated to penalize or incentivize certain types of deformations. The resulting vector field may be guided by utilizing multi-scale application of the algorithm, regularization of the vector field, and the way each demon force is calculated. One aspect of Vercauteren et al.'s adaptation of demons algorithm is incorporating diffeomorphic constraints to the deformation field. This ensures invertibility of deformable registration and preserves the

topology of the underlying image by preventing folding of the underlying anatomy, which is often physically impossible (*221*).

For the implementation of diffeomorphic demons for DIR in this work, a multi-scale approach is employed to apply DIR first at half the resolution of the raw image. Gaussian smoothing of the deformation field between iterations was applied with a kernel size of 1.0. The application of DIR within the LRR framework takes place between steps 4 and 5 outlined in Figure 23. The initial rigid registration of these volumes is an essential preprocessing step for attaining accurate results from DIR algorithms (*222*). Figure 24 demonstrates the application of DIR for RPT dose-rate accumulation in a necrotic spherical tumor model. Here, the CT and activity distribution at timepoints 1 and 2 are deformed, producing an unrepresentative cumulative absorbed dose distribution and substantial uncertainty in PTV definition. Following the application of DIR, the cumulative absorbed dose distribution is more accurately portrayed and the variance in ROI overlap, reduced.

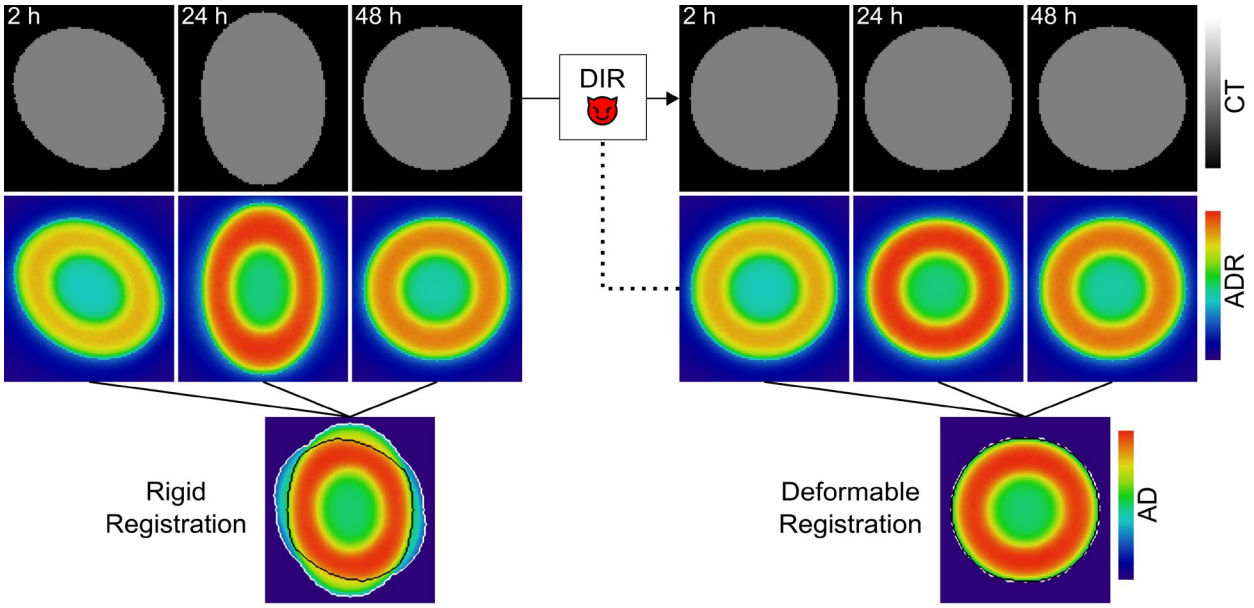

Figure 24: Example of dose rate accumulation with (left) and without (right) demons-based deformable registration (taking 48 h as the reference timepoint) in a sphere model of a tumor with a necrotic core. White and black contours on absorbed dose distributions (bottom) represent the union and intersection, respectively, of overlapping ROIs,

4.1.4 Target volume definition for theranostic dosimetry

All datasets in this work were presented with contours delineating the gross tumor volume (GTV) of each targeted tumor at each imaging timepoint. For preclinical work, physicist drawn contours were employed and for clinical work, physician drawn contours are provided. Unlike conventional radiotherapy applications where a specific dose is prescribed to a given target volume, the target volume in radiopharmaceutical therapy defines the prescription of desired dose to a region from a given, fixed, dose distribution. To assess the impact of registration accuracy on dosimetry, three target volume definitions were employed. Given a series of overlapping ROIs from registered target volumes, the minimum and maximum extent of this overlap may be characterized by the intersection and union, respectively, of the overlapping ROIs. A more simplistic approach is also employed that takes as true the target volume delineated at the reference timepoint.

ROI overlap was assessed in these models using both the Sørensen–Dice similarity coefficient (DSC) (*223*,*224*) and Hausdorff distance (d_H) (*225*,*226*). DSC represents intersectional overlap of the ROIs and was calculated using:

$$DSC(X,Y) = \frac{2|X \cap Y|}{|X| + |Y|} \qquad 18$$

The resulting value of DSC ranges between 0 and 1, with 1 representing perfect overlap. The Hausdorff distance represents the maximum perpendicular distance from any given point on contour X to any given point on contour Y is described by:

$$d_H(X,Y) = max\left\{\sup_{x \in X} d(x,Y), \sup_{y \in Y} d(X,y)\right\} \qquad 19$$

For this work, d_H was calculated using a modified approach by Dubuisson MP and Jain AK (*227*)

4.1.5 Anthropomorphic deformable phantom study

Guidance from TG 132 suggests that clinical systems utilizing DIR should be validated using a physical phantom (*228*). This guidance is primarily directed towards dose accumulation applications in conventional EBRT to ensure the quality of delivered dose, as verified with patient position imaging at each fraction, relative to that of the planned dose distribution. However, this guidance is similarly applicable in the field of RPT where prospective dosimetry and treatment planning is most accurately derived from multi-timepoint dose rate accumulation.

The LRR+DIR approach developed in this work was validated using a deformable polyvinyl chloride plastisol (PVCP) anthropomorphic phantom previously developed in our lab by Matrosic et al (*229*). The phantom is representative of the upper abdominal cavity with structures for the liver, stomach, kidneys, spine, spinal cord, and a tumor insert in the liver cavity (Figure 25). The PVC tumor insert was approximately 200 cm^3 which was within the range of tumor volumes observed in $^{86}Y/^{90}Y$-NM600 canine studies. The normal tissues in the PVCP phantom were designed with a density of 30.9 ± 4.6 HU while the tumor was given higher contrast at 709.6 ± 19.0 HU. Background tissue was given a density of -1.2 ± 6.7 HU. The deformable phantom was imaged in a SOMATOM Definition Edge CT scanner at three distinct deformation states resulting from a 0, 1.0, and 1.8 cm inferior-superior displacement. The resolution of each CT scan was 1.80 x 1.80 x 1.50 mm with Monte Carlo simulations for dosimetry performed at the same scale.

In order to model the multi-timepoint dosimetry from $^{86}Y/^{90}Y$-NM600 canine studies, a pseudo imaging series can be generated from a combination of phantom scans at various deformation states. Given three deformation states, nine distinct validations cases can be produced while holding the final timepoint constant. For this work, the undeformed phantom state was chosen for the final timepoint and one of the nine validation cases with three undeformed phantoms

in series was held as a control. Using contours of the tumor and normal tissues, an artificial activity distribution based on observations of uptake in ^{86}Y/^{90}Y-NM600 canine studies was then generated for each validation case.

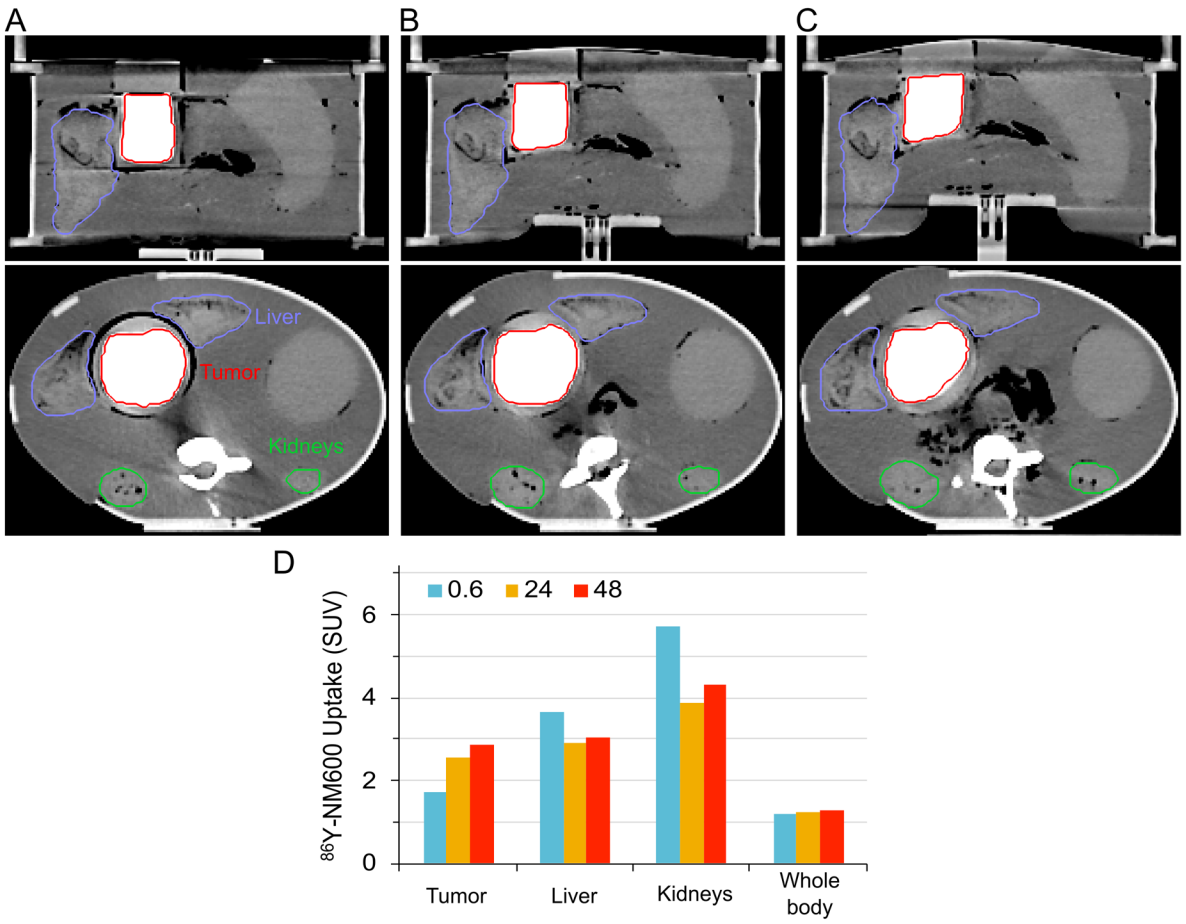

Figure 25: Coronal and axial slices of the deformable anthropomorphic phantom with inferior-superior displacements (A) 0.0, (B) 1.0, (C) and 1.8 cm. (D) The uptake of ^{86}Y-NM600 observed in a canine subject (#5, abdominal tumor) that was used to generate the underlying activity distribution for each validation case.

4.2 Results

4.2.1 Locoregional registration improves temporal coregistration of target volumes

The accuracy of each registration approach was assessed for the two deformation states used in the study, taking as a static reference the undeformed phantom state. Figure 26 showcases the final registration resulting from each approach in the most extreme deformation state with 1.8 cm inferior-superior displacement. Substantial improvement in ROI overlap was achieved after application of LRR, with DSC increasing from 0.657 to 0.901 (+31.3%) (Table 7). For the 1.0 cm displacement case, DSC following LRR similarly improved, but to a lesser extent (+17.5%). Given that the 1.0cm case started with overall better overlap (DSC of 0.793), this is to be expected. The ROI overlap achieved with LRR in the 1.0 cm case was 0.944 which was considerably higher than that achieved in the 1.8 cm case (DSC of 0.901). Interestingly, the improvement in HD from the application of LRR in both 1.0 and 1.8 cm displacement cases was 112.1% and 112.4%, respectively.

Despite the improved registration from LRR, the non-uniform deformation of the target volume in each displacement state limits the registration accuracy achievable with rigid methods. Further application of DIR to the LRR results for the 1.0 and 1.8 cm cases achieved considerably better ROI overlap (DSC of 0.967 and 0.973, respectively). Despite the 1.8 cm displacement case showcasing more severe non-uniform deformation of the target volume than in the 1.0 cm case, the final DSC achieved in both cases was similarly around 0.970 DSC. Similarly, the final HD resulting from LRR+DIR in the 1.0 and 1.8 cm cases was 0.77 and 0.61 mm, respectively. Overall, the LRR+DIR approach improved DSC by 19.8-38.7% and HD by 139.2-169.3%.

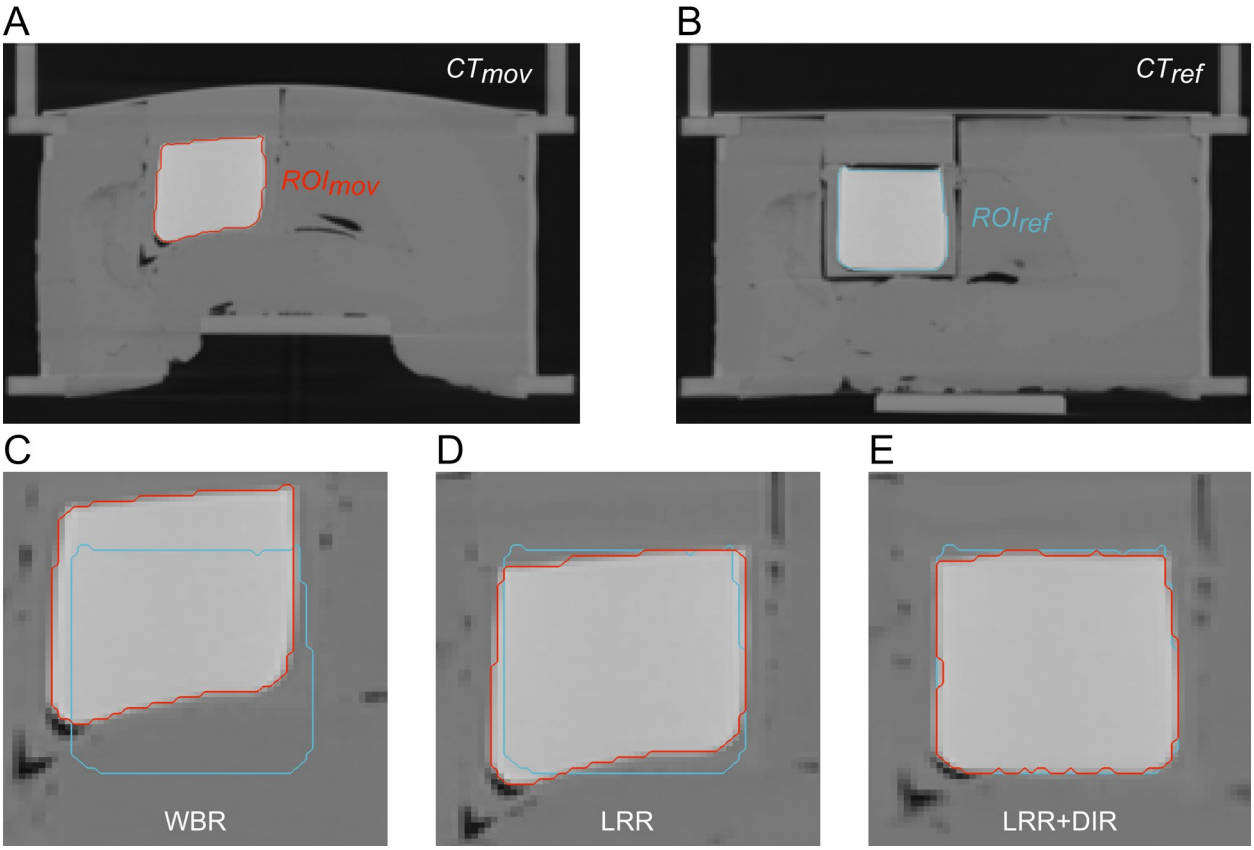

Figure 26: Impact of registration approach on ROI overlap in the context of significant deformation. (A) The target volume from the deformed timepoint (contour in red) is registered to the (B) undeformed reference target volume (contour in blue). ROI overlap results are shown for (C) whole-body, (D) locoregional, and (E) locoregional + deformable image registration.

Table 7: Analysis of ROI overlap following WBR, LRR, and LRR+DIR registration approaches

	Dice similarity coefficient			**Hausdorff distance (mm)**		
Displacement	**WBR**	**LRR**	**LRR+DIR**	**WBR**	**LRR**	**LRR+DIR**
1.0 cm	0.793	0.944	0.967	4.31	1.21	0.77
1.8 cm	0.657	0.901	0.973	7.36	2.06	0.61

4.2.2 Improved registration reduces dosimetric uncertainty due to target volume definition

The full theranostic dosimetry workflow was performed on all validation cases consisting of every possible combination of three deformation states while holding constant the final timepoint. As such, a unique dose distribution is generated for each registration approach in each validation case. For all work presented, the validation case, which was composed of a series of undeformed phantom states, was taken as the control distribution. In this control case the target volumes defined by the intersection, union, and reference ROIs are identical. Given that the CT scans at each timepoint are duplicates, the dose distribution similarly remains identical across registration approaches.

The cumulative dose volume histograms (DVHs) resulting from each unique dose distribution in each validation case are shown in Figure 27. For a PTV defined by the intersection of overlapping ROIs, the resulting DVH for each case and registration approach was dosimetrically hot relative to the control case. Comparatively, a PTV defined by the union of overlapping ROIs produces a DVH that is consistently colder than the control case due to the inclusion of non-target volume defined voxels. As registration accuracy and ROI overlap improves from WBR to LRR and LRR to LRR+DIR, the variance between the DVHs produced from each case decreases and begins to resemble more closely that of the control case. Figure 28 provides a more in-depth analysis of the dose distribution and DVH in each case. The range of uncertainty in the DVH due to target volume definition is shown as the difference in D_{90} between the intersection and union PTVs. This spread was 35.0% ± 4.3% for WBR, 14.4% ± 7.7% for LRR, and 4.4% ± 1.9% for LRR+DIR. Overall, a PTV defined by the intersection of ROIs produced a more accurate DVH than that of the union of ROIs with a difference in D_{90} of +3.4% ± 0.8% in the WBR case to +1.8% ± 0.9% for LRR+DIR. In comparison, the difference in D_{90} produced from the union of ROIs was

-31.6% ± 4.9% for WBR, -10.6% ± 6.6% for LRR, and -2.6% ± 1.3%. In all cases the uncertainty in D_{90} due to target volume definition was lowest following application LRR+DIR. Additionally, dosimetry using the reference volume as the PTV produced results more similar to the true profile in all registration cases: -1.4% ± 1.1% for WBR, -0.3% ± 0.6% for LRR, and -0.4% ± 0.4% for LRR+DIR.

For the ROI-level metric of mean dose, the impact of target volume definition is smaller but still substantial. In the case of WBR approaches, D_{mean} ranges from -9.8% ± 2.2% to +0.7% ± 0.1% based on PTVs defined by the union and intersection of ROIs, respectively. Following implementation of the LRR+DIR approach, this range in D_{mean} was reduced from 10.5% ± 2.2% to 1.8% ± 0.7%. As observed with D_{90}, estimates of D_{mean} were more accurate using the reference ROIs than the union or intersection approaches.

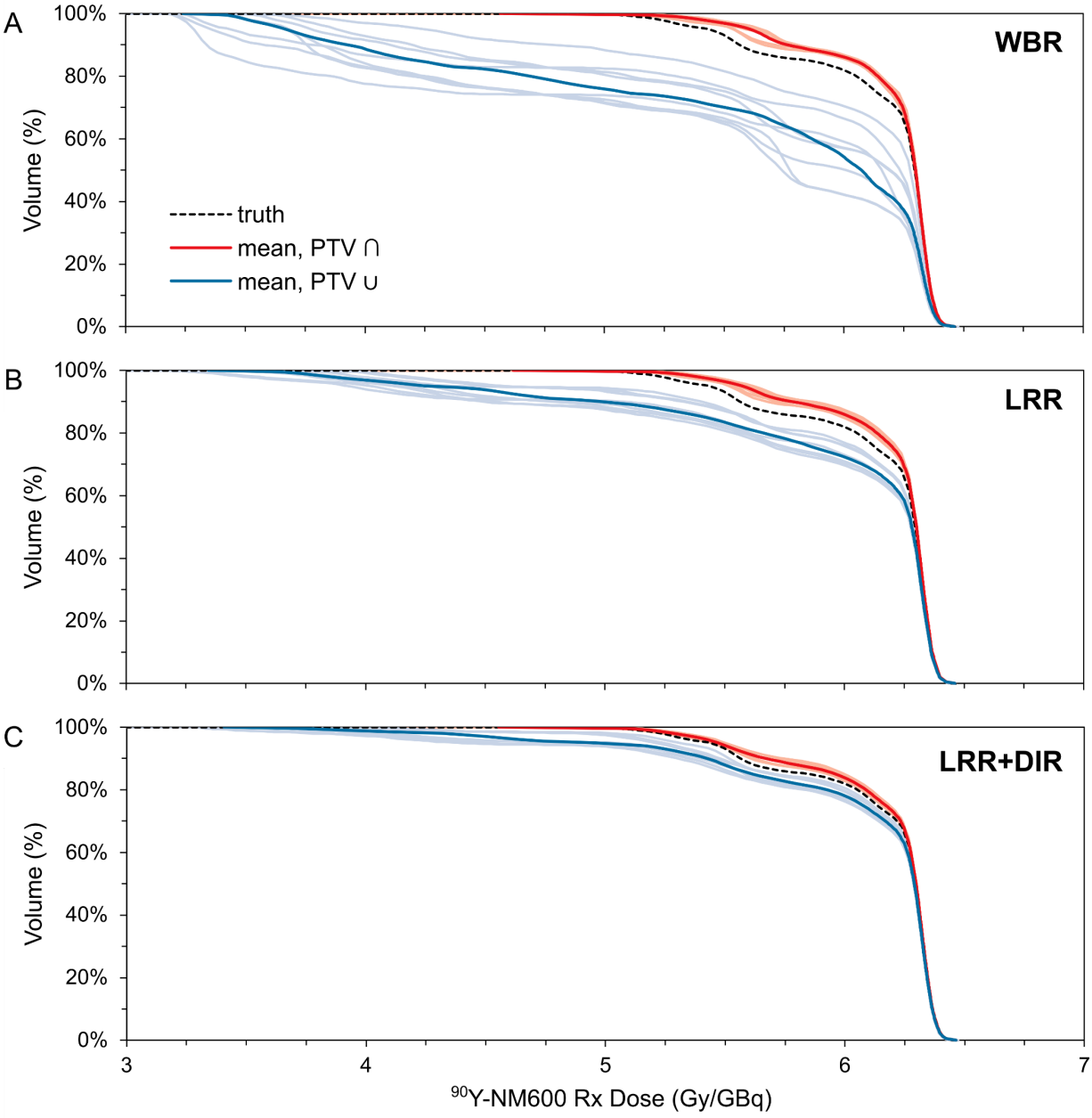

Figure 27: Cumulative dose volume histograms (DVHs) determined using the intersection (∩) and union (∪) of the target volumes registered via (A) WBR, (B) LRR, and (C) LRR+DIR approaches. All 8 validation cases are shown in a lighter shade with the bold color representing the average DVH. Results for the true, undeformed, validation case is shown with a dashed black line.

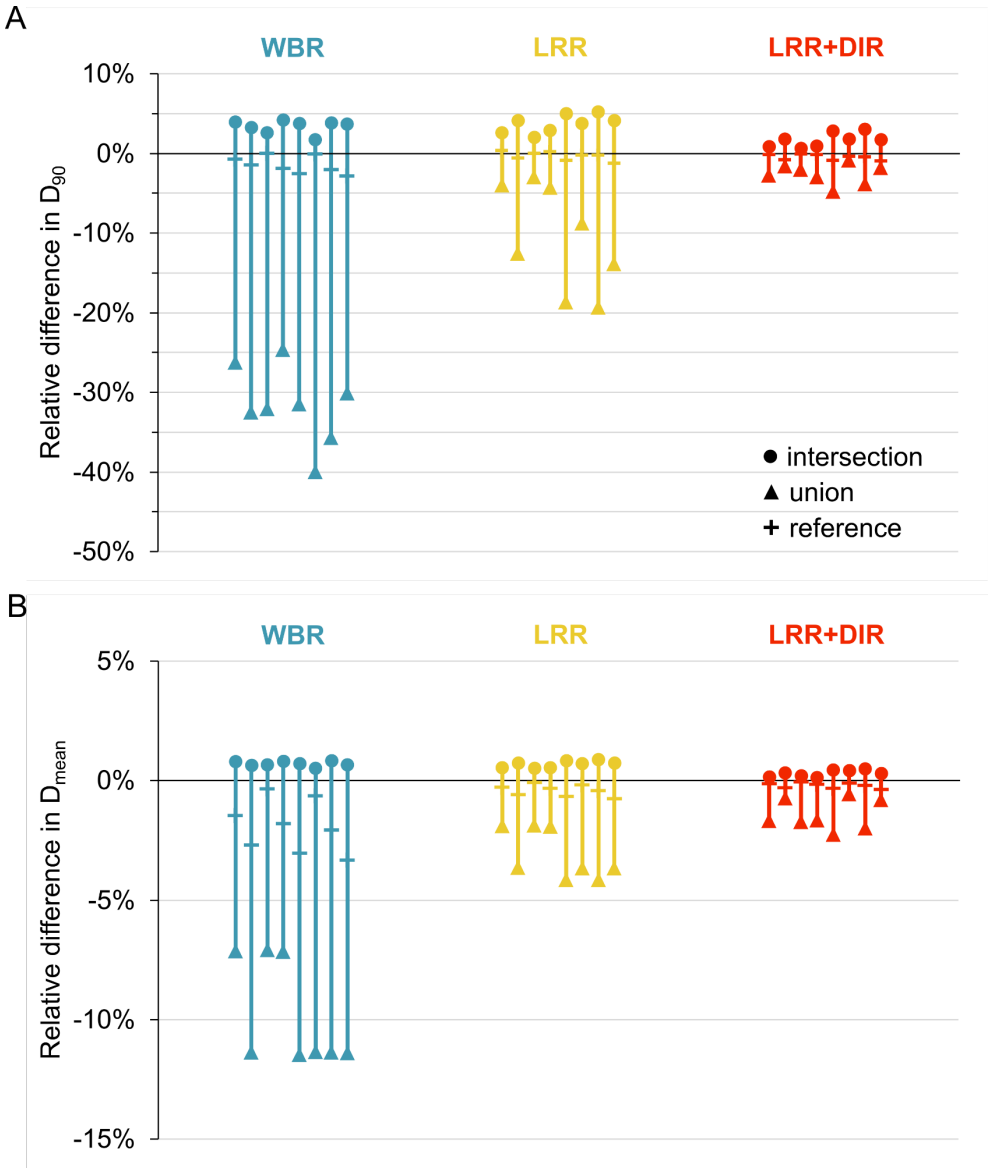

Figure 28: The range of measured (A) D_{90} and (B) D_{mean} determined using the intersection, union and reference target volumes registered via WBR, LRR, and LRR+DIR. The result from each case is shown connected with a line for each registration approach.

4.2.3 Accuracy of dose-rate accumulation enhanced with improved registration

The registration approach implemented in each validation case will produce a unique dose distribution following temporal integration of the underlying ADR volumes. To assess the impact of registration on the accuracy of the final dose distribution, a PTV defined by the reference volume at the final timepoint, which was held constant across all validation cases, was used to compare DVH profiles, dose difference maps, and gamma analysis. A comparison of the WBR, LRR, and LRR+DIR approaches for a representative case (in order of 1.0, 1.8, and 0.0 cm deformation states) is shown for Figure 29. With WBR, significant dose differences due to the inferior-superior displacement present at earlier timepoints is present in the inferior portion of the target volume. Following LRR this issue is reduced, but dose differences are still observed near the edges of the target volume due to the non-uniform nature of the deformations. With full application of LRR+DIR the dose differences at the deformed edges of the target volume are practically eliminated. Notably, improvements in the dose difference of regions outside the target volume can also be observed, but to a more limited extent.

Additional 3D global gamma analysis of this representative case was performed over a range of distance to agreement and percentage difference values (Table 8, Table 9, and Table 10). Voxels within the reference PTV with gamma values ≤ 1.0 are considered passing (Figure 29C). If the overall percentage of passing voxels within the reference PTV is $\geq 95\%$, the dose distribution is considered to pass for the given gamma analysis parameters. While results from WBR (Table 8) fail the entire spectrum of gamma analysis parameters tested, the results produced by LRR+DIR passed even the most stringent gamma analysis at 0.5% and 0.5 mm. The gamma pass rate at 2% 2 mm was 77.1% for WBR, 98.2% for LRR, and 100% for LRR+DIR in this validation case.

Additional gamma analysis of each registration approach was performed for each validation case. For WBR the average passing rate was 86.9% ± 9.6%, considered failing by ≥ 95% passing criteria, highlighting the unacceptable dosimetric accuracy of this approach in multi-timepoint internal dosimetry. Following LRR and LRR+DIR the gamma pass rate improved to 99.0% ± 0.8% and 100% ± 0.001%, respectively. The cumulative DVH profiles defined by the reference ROI for each validation case following application of WBR, LRR, and LRR+DIR are shown in Figure 30. Similar to the observations with intersection and union defined PTVs, significant variability between DVH profiles produced by the WBR approach can be seen. As registration accuracy improves with application of LRR and LRR+DIR the profiles closely resemble that of the true distribution.

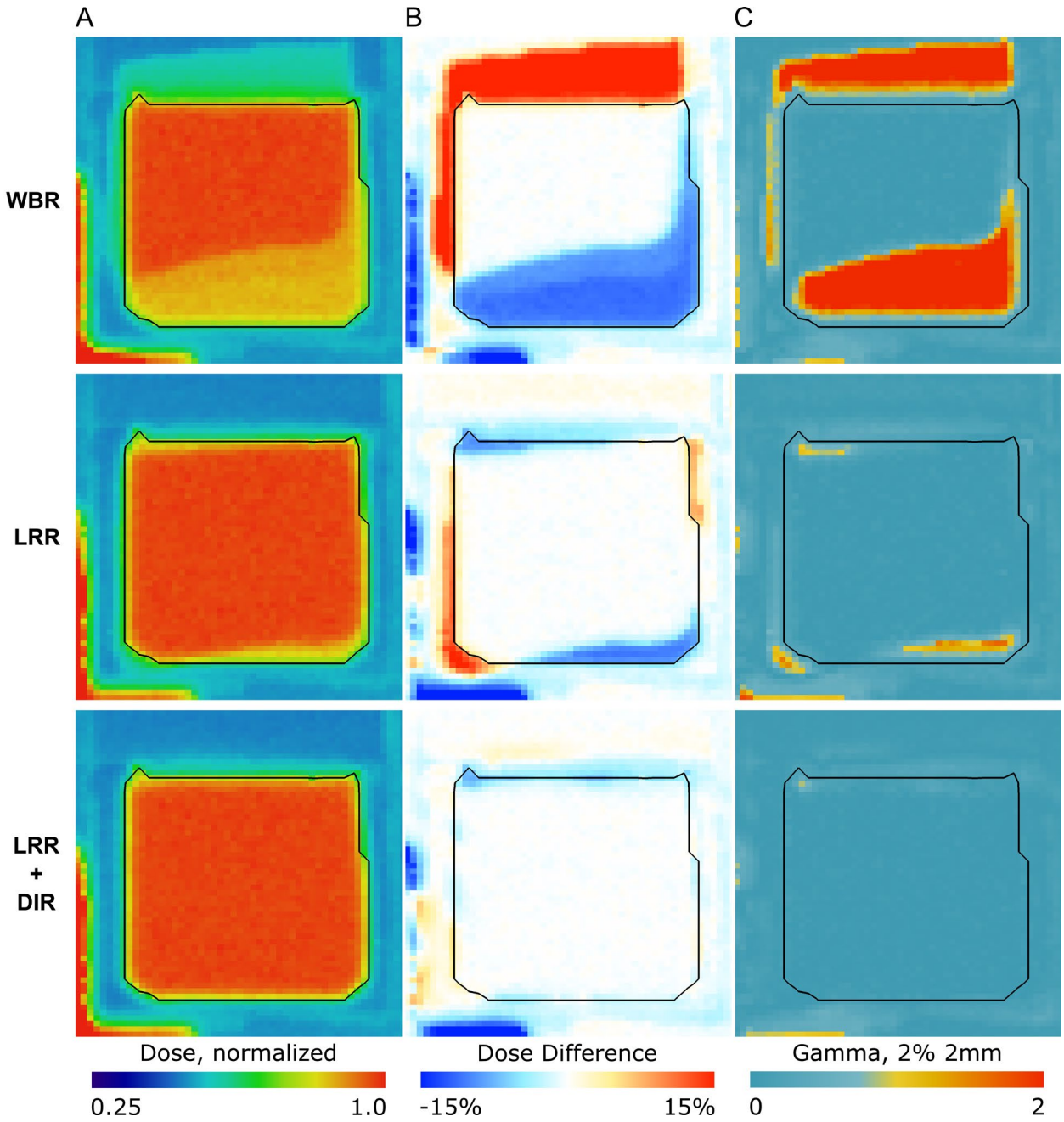

Figure 29: Coronal slices of the (A) dose distributions resulting from WBR, LRR, and LRR+DIR registration approaches. (B) Dose difference and (C) 3D global gamma analysis (2% and 2mm) is shown relative to the true dose distribution from the undeformed case. 3D gamma analysis is displayed over the range of 0 to 2, where any value <1.0 is passing under the 2% 2mm criteria. PTV defined by the reference ROI is overlayed in black.

Table 8: 3D gamma global analysis of the WBR dose distribution within the reference ROI calculated for a range of gamma parameters. Pass/fail (blue/red) criteria is set at 95%.

Percent (%) \ Distance to agreement (mm)	0.5	1.0	1.5	2.0	2.5	3.0	3.5	4.0	4.5	5.0
5.0	75.5%	76.9%	79.6%	80.3%	81.7%	83.5%	84.3%	85.4%	86.7%	87.6%
4.5	74.9%	75.8%	78.7%	79.7%	81.0%	83.0%	83.8%	84.8%	86.3%	87.1%
4.0	74.0%	74.9%	77.7%	79.2%	80.3%	82.5%	83.4%	84.4%	86.0%	86.8%
3.5	72.7%	73.7%	76.2%	78.3%	79.3%	81.6%	82.7%	83.5%	85.3%	86.1%
3.0	71.7%	73.1%	75.3%	77.8%	78.9%	81.2%	82.2%	83.0%	84.8%	85.6%
2.5	70.3%	72.6%	74.5%	77.4%	78.5%	80.8%	81.9%	82.7%	84.5%	85.4%
2.0	68.5%	72.2%	73.9%	77.1%	78.2%	80.4%	81.6%	82.4%	84.2%	85.1%
1.5	66.4%	71.7%	73.3%	76.7%	77.9%	80.1%	81.3%	82.1%	83.9%	84.8%
1.0	63.6%	71.0%	72.6%	76.0%	77.4%	79.5%	80.8%	81.4%	82.8%	83.7%
0.5	58.5%	69.2%	71.1%	73.9%	74.8%	75.5%	77.8%	77.7%	78.3%	79.2%

Table 9: 3D global gamma analysis of the LRR dose distribution within the reference ROI calculated for a range of gamma parameters. Pass/fail (blue/red) criteria is set at 95%.

Percent (%) \ Distance to agreement (mm)	0.5	1.0	1.5	2.0	2.5	3.0	3.5	4.0	4.5	5.0
5.0	97.5%	98.3%	99.0%	99.2%	99.6%	99.8%	99.9%	100%	100%	100%
4.5	97.0%	97.8%	98.8%	99.0%	99.5%	99.7%	99.8%	99.9%	100%	100%
4.0	96.6%	97.3%	98.5%	98.9%	99.4%	99.6%	99.8%	99.9%	100%	100%
3.5	96.1%	96.9%	98.2%	98.7%	99.2%	99.6%	99.7%	99.9%	99.9%	100%
3.0	95.4%	96.4%	97.7%	98.6%	99.1%	99.5%	99.7%	99.9%	99.9%	100%
2.5	94.6%	96.1%	97.3%	98.4%	98.9%	99.4%	99.6%	99.8%	99.9%	100%
2.0	93.7%	95.6%	96.9%	98.2%	98.8%	99.3%	99.6%	99.8%	99.9%	99.9%
1.5	92.6%	95.2%	96.6%	98.0%	98.7%	99.3%	99.5%	99.8%	99.9%	99.9%
1.0	91.0%	94.7%	96.1%	97.7%	98.5%	99.1%	99.4%	99.6%	99.7%	99.6%
0.5	88.1%	93.6%	95.3%	96.9%	97.4%	97.5%	98.1%	97.8%	97.9%	98.1%

Table 10: 3D global gamma analysis of the LRR+DIR dose distribution within the reference ROI calculated for a range of gamma parameters. Pass/fail (blue/red) criteria is set at 95%.

Percent (%) \ Distance to agreement (mm)	0.5	1.0	1.5	2.0	2.5	3.0	3.5	4.0	4.5	5.0
5.0	100%	100%	100%	100%	100%	100%	100%	100%	100%	100%
4.5	99.9%	100%	100%	100%	100%	100%	100%	100%	100%	100%
4.0	99.9%	100%	100%	100%	100%	100%	100%	100%	100%	100%
3.5	99.8%	99.9%	100%	100%	100%	100%	100%	100%	100%	100%
3.0	99.7%	99.9%	100%	100%	100%	100%	100%	100%	100%	100%
2.5	99.6%	99.9%	100%	100%	100%	100%	100%	100%	100%	100%
2.0	99.5%	99.8%	99.9%	100%	100%	100%	100%	100%	100%	100%
1.5	99.3%	99.7%	99.9%	100%	100%	100%	100%	100%	100%	100%
1.0	99.1%	99.6%	99.9%	100%	100%	100%	100%	100%	99.9%	99.8%
0.5	98.5%	99.5%	99.8%	99.9%	99.6%	99.4%	99.2%	98.9%	98.8%	98.6%

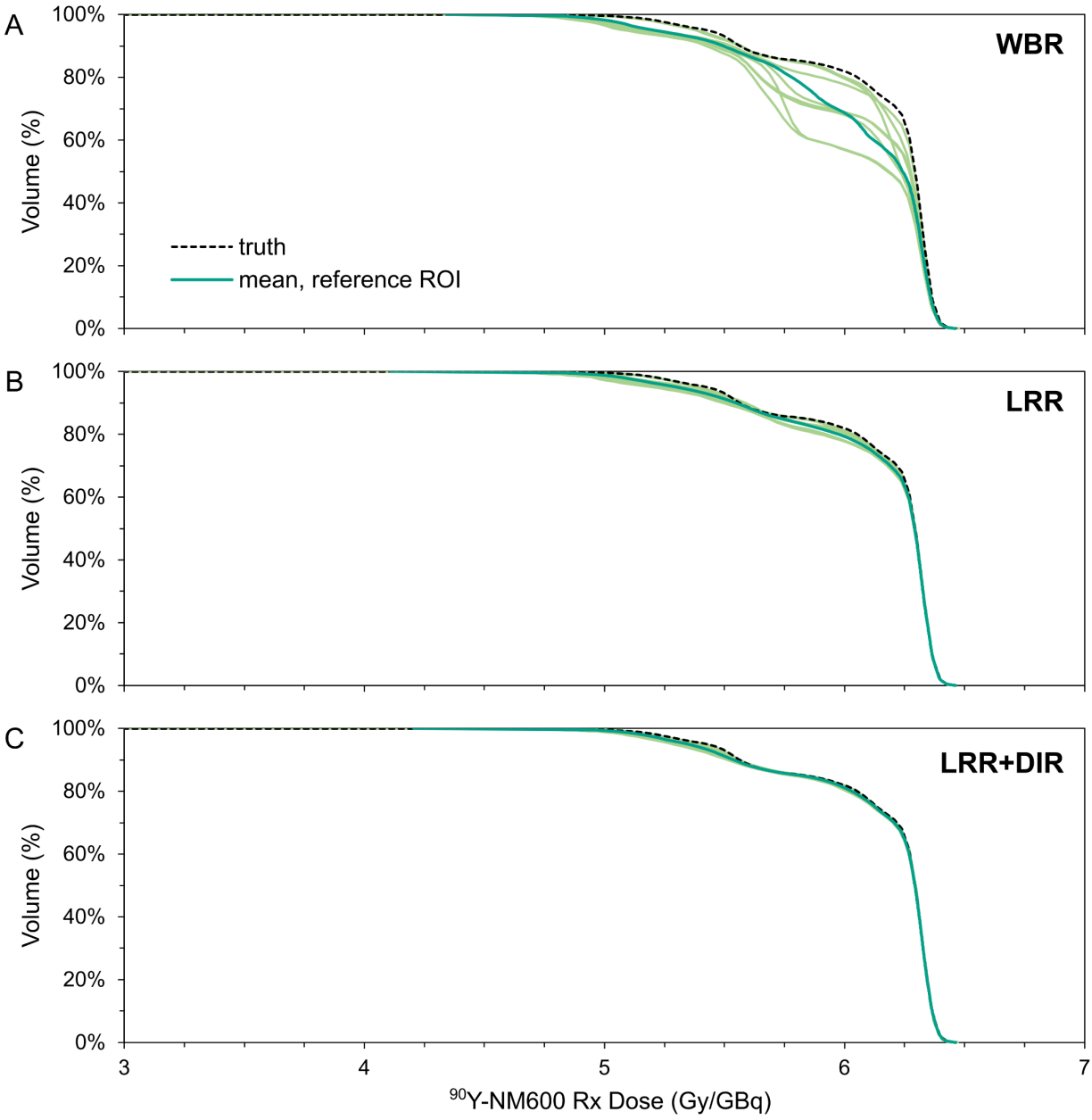

Figure 30: Cumulative dose volume histograms (DVHs) determined using the reference ROI as the target volume and following registration via (A) WBR, (B) LRR, and (C) LRR+DIR approaches. All 8 validation cases are shown in a lighter shade with the bold color representing the average DVH. Results for the true, undeformed, validation case is shown with a dashed black line.

4.3 Discussion

The registration accuracy of the target volume registered in multi-timepoint internal dosimetry was significantly improved following the application of LRR and DIR approaches, with the greatest ROI overlap achieved from a serial combination of LRR+DIR. Substantial improvements were achieved with the rigid LRR approach (+19.8-38.7% in DSC and -112.1%-112.4% in HD), but the non-uniform deformation of the target volume limited the achievable ROI overlap. With the application of DIR following LRR (LRR+DIR), these discrepancies were significantly reduced and a final DSC of 0.967-0.973 and HD of 0.61-0.77 mm was achieved. The registration accuracy achieved here matches that reported by previous investigations on the impact of DIR on external beam dose accumulation within bladder (DSC between 0.95-0.97) and rectum (DSC between 0.889-0.94) OARs (*230*). Important to note with the results reported here is that the image resolution of the anthropomorphic phantom was 1.80 mm x 1.80 mm x 1.50 mm, suggesting that the LRR+DIR approach achieved registration accuracy within one voxel width. Considering the voxel size in clinical PET images is on the range of 3-4 mm, the registration accuracy achieved with the developed LRR+DIR approach is more than sufficient for theranostic dosimetry and treatment planning for ^{86}Y/^{90}Y-NM600.

It was found that the dosimetric impact of target volume definition in multi-timepoint internal dosimetry can be reduced by 30.6% (from 35.0% to 4.4% difference in D_{90}) with the use of more advanced registration approaches, such as the developed LRR+DIR methodology, prior to temporal integration of the ADR distributions. D_{90} was chosen to assess the dosimetric impact on cumulative DVH profiles due to it's common use in treatment planning for conventional brachytherapy applications (*231*). Additionally, in all registration approaches, a PTV defined by

the intersection of ROIs was more accurate than that determined by using the union. Although the most accurate PTV definition in this analysis resulted from that of the reference ROI, which appears to be a good compromise between the overestimating intersection of ROIs and underestimating union of ROIs. However, the characteristic underestimation of the DVH profile with the reference PTV approach may not be reflected in all applications. The use of a single reference ROI would also substantially reduce the requisite time for contouring at each timepoint which poses an obstacle to adoption of multi-timepoint internal dosimetry approaches in the clinic. However, the LRR+DIR registration approach developed in this work requires contours at each timepoint for localization and further work is needed to develop a less-guided approach.

Gamma analysis of the dose distributions in this work suggests that while the LRR+DIR approach achieves by far the most dosimetrically accurate results (100% gamma pass rate at 2%/2 mm), the application of LRR alone can significantly improve the accuracy of underlying dose distributions with 98.2% gamma pass rates at 2%/2 mm achievable in this case. For comparison, in conventional IMRT QA, gamma analysis criteria is typically set to 3%/3 mm and ≥ 95% when comparing planned and delivered dose distributions. Notably, the accuracy of the underlying dose distribution produced from LRR+DIR approach was greatest within and around the target ROI while regions further from the targeted ROI still exhibited large dose differences. This supports the stance adopted by the developed LRR+DIR approach that dosimetry results from this targeted registration approach are limited to within the targeted ROI. If dosimetric analysis of adjacent regions is desired, targeted registration should be performed separately for those ROIs.

4.4 Acknowledgements

I would like to thank RED lab alumni Charlie Matrosic for designing and developing the 3D anthropomorphic phantom as well as performing CT imaging of the phantom in various deformation states. Abigail Besemer, another RED Lab alumni, provided the inspiration for the automated temporal coregistration approaches developed in this work. Committee member and advisor Bryan Bednarz provided guidance, funding, and discussion towards the completion of this work.

Chapter 5

Implementation of Theranostic ^{86}Y/^{90}Y-NM600 Dosimetry in the Clinical Setting

The success of tri-modal combinations of EBRT, ^{90}Y-NM600 radiopharmaceutical therapy, and systemic or targeted immunotherapies in preclinical tumor models has driven support for further translational investigations in companion canine models (*12*,*18*,*19*,*84*,*232*). Of particular interest in these translational investigations is whether the systemic immunomodulatory capacity of low-dose ^{90}Y-NM600 is maintained in the context of naturally occurring metastatic cancer models while continuing to abate systemic lymphopenia. Notably, the maximum range of ^{90}Y betas (~11 mm) provide considerably less crossfire in 20 kg dogs than that observed in 20 g mice. Key to the safe delivery and dose escalation of ^{90}Y-NM600 in canine patients is the personalized prescription of low-dose RPT leveraging pre-therapy PET-CT imaging with ^{86}Y-NM600 for theranostic dosimetry. In this chapter, we will cover the clinical implementation of the multi-timepoint

theranostic dosimetry methodology developed earlier in this work and assess the impact on treatment planning for six canine patients.

5.1 Methods and Materials

5.1.1 Companion canine patients

All studies performed on client-owned companion dogs were conducted under protocols approved by the Institutional Animal Care and Use Committees of the University of Wisconsin-Madison School of Veterinary Medicine (V006037 and V006123). Written informed consent was also obtained from all companion dog caregivers prior to entry into the trial. Companion canine patients received protocol prescribed care at the University of Wisconsin Veterinary care hospital (UWVC).

To be eligible for the study, companion canine patients needed to have advanced stage cancer with a biopsy-accessible primary tumor of at least 2 cm in length at the largest extent and at least one distant metastatic lesion. All dogs were required to present a pre-treatment constitutional clinical sign status of 0 or 1 (normal or asymptomatic/mild symptoms but able to function as an acceptable pet, respectively) based on Veterinary Cooperative Oncology Group – Common Terminology Criteria for Adverse Events (VCOG-CTCAE v1.1) criteria (*233*). Prior radiation therapy or immunotherapy was considered as an exclusion criteria and a minimum of 2 weeks from prior chemotherapy was required for washout. Dogs with prior surgery were allowed under the condition that post-surgical resurgence of the primary tumor attained the 2 cm minimum length threshold. Adverse events from treatment were monitored for, graded, and attributed for all dogs in all single and combination treatment groups throughout the observation period using VCOG-CTCAE v1.1 criteria. Prior to treatment, baseline physical examinations, CBC, biochemistry panels, and urinalyses were performed. Repeat screening for bloodwork, urinalysis,

and biospecimen collection (e.g. serum, plasma, PBMC, tumor biopsy) was performed at 6, 13, and 29 days after treatment commenced with additional monthly follow up.

5.1.2 In situ vaccination with EBRT+ IT-IC

The protocol for in situ vaccination in this study involves the combined delivery of focal EBRT followed 5-7 days later with a series of intratumoral (IT) injections of the immunocytokine (IC) hu14.18-IL2 over three consecutive days. hu14.18-IL2 is an immunocytokine fusion protein that consists of human recombinant IL2 (hrIL2) fused to the humanized anti-disialoganglioside (anti-GD2) monoclonal antibody (mAb), hu14.18, and has been investigated for the treatment of melanoma and neuroblastoma in humans (*234*,*235*). Notably, as a disialoganglioside, GD2 is not species specific and the hu14.18 mAb has been shown to recognize GD2 on human, canine, and mouse melanoma. Specifically, canine melanoma and soft tissue sarcomas have been shown to express GD2 and hrIL2 has been shown to produce significant immunostimulatory activity in dogs (*236*,*237*). When administered via IT injections, the hu14.18-IL2 compound used in this work elicits increased activation of T and NK cell infiltrates and tumor growth inhibition (*238*). Used in combination with EBRT in mouse models, IT-IC hu14.18-IL2 generates an *in situ* vaccination effect resulting in enhanced tumor response characterized by increased NK cell and CD8+ T cell infiltration along with antitumor immune memory (*7*).

Treatment planning and delivery of EBRT to companion canines in this work was performed by collaborators in veterinary oncology using a TomoTherapy HiArt treatment system (Accuray Inc., Sunnyvale, CA, USA). Canine patients underwent CT simulation, and the gross tumor volume (GTV) for the index lesion was delineated by the attending veterinary oncologist. A final treatment planning volume was generated by adding an approximately 2 mm margin (depending on anatomic region) to the GTV. Additional margins defining a clinical treatment

volume were not added in this approach to avoid unnecessary dose to peritumoral microscopic disease to help facilitate the *in situ* vaccination effect. Notably, the treatment volumes defined for EBRT by the veterinary oncology groups were not used in theranostic ^{86}Y/^{90}Y-NM600 treatment planning for ^{90}Y-NM600 RPT. A single fraction of intensity modulated radiotherapy (IMRT) delivering 8 Gy to 95% of the PTV was used. Nearby normal tissues were also contoured and plans were optimized to minimize dose to organs at risk (OARs) while maximizing the treatment planning objective for the PTV.

Five to seven days following delivery of EBRT, IT-IC injections were administered to the index lesion over the course of three consecutive days at a rate of 6 mg/m^2/d. The hu14.18-IL2 was injected in sedated or anesthetized dogs through a 25 gauge needle at a rate of 0.5 ml over 3 minutes while multiple needle re-directions were utilized to ensure adequate coverage of the index lesion. Time was allowed, as needed, between administrations to allow for puncture site clotting to avoid leakage of the injected material. Findings from prior and concurrently running IT-IC dose escalation trial had demonstrated effective use of 6 mg/m^2/d for the rate of delivery (*239*). hu14.18-IL2 was provided by Apeiron Biologics (Vienna, Austria).

5.1.3 EBRT + Low-dose ^{90}Y-NM600 + IT-IC combination protocol

The tri-modal treatment approach implemented in this companion canine trial seeks to enhance the *in situ* vaccination effect from EBRT + IT-IC by leveraging systemic ^{90}Y-NM600 RPT to deliver immunomodulatory dose to all sites of disease and overcome concomitant immune tolerance (CIT) (*9*). Figure 31 shows an overview of the trial structure. Following entry into the trial, patients are administered ^{86}Y-NM600 and undergo serial PET/CT imaging at 2, 24, and 48 h post-injection. Prior to each imaging timepoint, a blood sample was acquired to provide a secondary check on observed blood activity. In the 7-14 days following administration of ^{86}Y-

NM600, theranostic ^{86}Y/^{90}Y-NM600 dosimetry is performed using the RAPID platform to calculate the prescription absorbed dose (Rx dose) in tumors and normal tissues with units of dose per injected activity of ^{90}Y-NM600. Following consultation with colleagues in human oncology, veterinary oncology, radiology, and medical physics, the requisite administered activity of ^{90}Y-NM600 for RPT delivering a minimum of 2 or 3 Gy to all target lesions is chosen. Notably, five of six canine patients used in this analysis were in the 2 Gy cohort (taking place between February-November 2019) and one patient was in the 3 Gy cohort (July 2021). Patients were then treated with 8 Gy EBRT to the index tumor and prescribed ^{90}Y-NM600 via IV injection. EBRT was prescribed as described in section 5.1.2. Following treatment, all dogs were hospitalized in a UW-Madison radiation safety approved holding area within the UWVC. Radiation exposure at 1 m was measured daily until falling below the radiation safety limit (< 1 mR/hr at 1 m), at which time they were released to the companion owner. IT-IC injections to the index tumor site at 6 mg/m^2/d were then given one week later over three consecutive days.

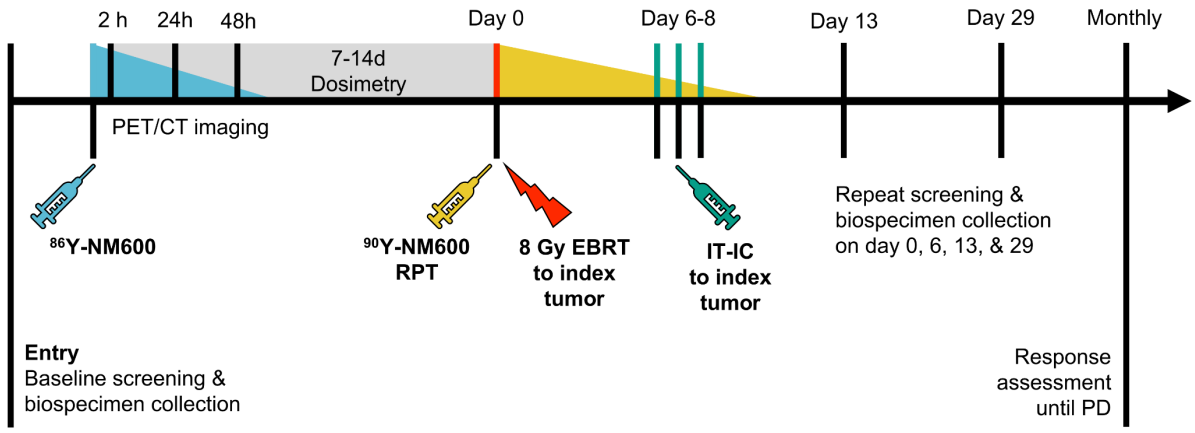

Figure 31: Overview of the tri-modal EBRT + IT-IC + ^{90}Y-NM600 RPT trial protocol. Note that icons and markers are not drawn to exact scale.

5.1.4 PET/CT imaging of ^{86}Y-NM600

Following enrollment, each canine patient received 5-10 mCi of ^{86}Y-NM600 via IV injection over five minutes and was imaged with serial PET/CT imaging at 2, 24, and 48 h on a GE Discovery MI scanner (GE Healthcare, Waukesha, WI). The production and labeling of ^{86}Y-NM600 and ^{90}Y-NM600 is described in section 3.1.1 of this work. While imaging was performed, canine patients were under general anesthesia and positioned in a prone position while immobilized using a bite block system and vacuum formable mattress to ensure repeatability of patient setup. CT scans (140 kVp, 4 mAs, 0.517 pitch factor) were acquired at a resolution of 1.37 x 1.37 x 2.79 mm. List mode PET scans (energy window of 425-650 keV, frame duration of 5, 7, and 10 min at 2, 24, and 48/72 h post-injection) were acquired at a resolution of 3.65 x 3.65 x 2.79 mm. PET image volumes were reconstructed both with (VPFX) and without (VPHD) time of flight and with (VP**-S) and without SharpIR applied. OSEM reconstruction in VPHD and VPFX was performed at 16 subsets and 4 iterations with a standard z-axis gaussian filter used during reconstruction. After each imaging timepoint, scan data was transferred to begin dosimetry and Monte Carlo simulations.

Following the final PET/CT timepoint, a contrast enhanced CT image was acquired following an IV injection of a bolus of iodine-based contrast agent to assist with contouring. The GTV for each apparent lesion was then defined by the collaborating veterinary oncologist, Michelle Turek, DVM, using Eclipse (Varian Medical Systems, Palo Alto, CA, USA). Normal tissue contours representing the liver, kidneys, gallbladder, marrow, heart, and spleen were additionally drawn at each timepoint before the structure sets were transferred to the dosimetry team for analysis.

5.1.5 Theranostic ^{86}Y/^{90}Y-NM600 tumor dosimetry for low-dose ^{90}Y-NM600 RPT

In order to produce prospective and patient-specific tumor dosimetry estimates for ^{90}Y-NM600 from pre-therapy PET/CT images of ^{86}Y-NM600, we employed the Radiopharmaceutical Assessment Platform of Internal Dosimetry (RAPID) platform (*206*,*240*), as described previously in section 3.1.5. Figure 32 describes the RAPID framework as applied to canine patients in this work. In application to this clinical dataset, CT and PET image volumes at each timepoint were registered via normalized mutual information and fused to an intermediate image matrix (2.73 x 2.73 x 2.79 mm) between CT and PET resolutions. PET imaged activity distributions of ^{86}Y-NM600 are decay corrected to represent ^{90}Y-NM600. Absorbed dose rate (ADR) distributions at each timepoint were then generated from Geant4 (version 9.6) Monte Carlo simulations using CT and PET volumes to define the geometry and source distribution, respectively. At least 4960 decays of ^{90}Y were simulated uniformly in each source voxel, or 2-10 billion decays per timepoint depending on patient size, to achieve less than 1% mean relative error in target ROIs. Simulations were performed using the RED Lab's computer cluster, KING, containing 32 CPUs (Intel Xeon E5405, 2.00 GHz, 4 cores) capable of running 128 jobs concurrently. Simulations were run in batches of 32 jobs, each performing 155 decays per source voxel (4960 decays per source voxel, total). Once simulations are completed and physician drawn contours have been imported into the RAPID workflow, target ROIs along with associated ADR volumes are temporally coregistered to the final timepoint. Finally, an absorbed dose distribution for each target ROI is produced by integrating the time-dose rate curve with a trapezoidal exponential fit. Beyond the final timepoint, the time-dose rate curve is modeled with purely radioactive decay and while the region of the curve between t_0 and t_1 is modeled as a linear extrapolation from a line connecting t_1 and t_2.

For tumors located in regions of low-density media (e.g. lung metastasis) with substantial intrascan motion, separate Monte Carlo simulations were performed assuming water density of the underlying tissue. This circumvents known limitations in the RAPID approach wherein partial volume effects from motion during the scan result in blurring of the CT image and artificially low HU density within the tumor ROI. Similarly, motion during the PET scan acquired over a substantially longer period of time can systematically blur the observed activity distribution underlying the CT scan. In all, the presence of low density HU values underlying high activity spill-out from the motion blurred PET image result in artificially high dosimetry estimates. Lung metastases dosimetry is additionally compared against estimates derived from conventional OLINDA sphere models (*87*).

Lung metastasis dosimetry presented in this work utilizes a combination of VPHD-LR PET derived source distributions simulated in unit density-based geometry models with ROI-level PVC of mean dose rate using Equation 16 (pg. 46). The PVC parameters D_{bkgd}, $D_{spillout}$, RC, and ($SAF/SAF_{VPHD-LR}$) were calculated based on the mean volume of the target tumor ROI across the PET/CT image series and the RC curve defined for VPHD-LR in the 10:1 Jaszczak hot sphere phantom study (Figure 17, pg. 64). D_{bkgd} was determined based on the estimated ^{90}Y-NM600 activity concentration in the lungs and an S-factor for a uniform activity distribution of 1.47×10^{-10} (Gy/s)/(Bq/ml).

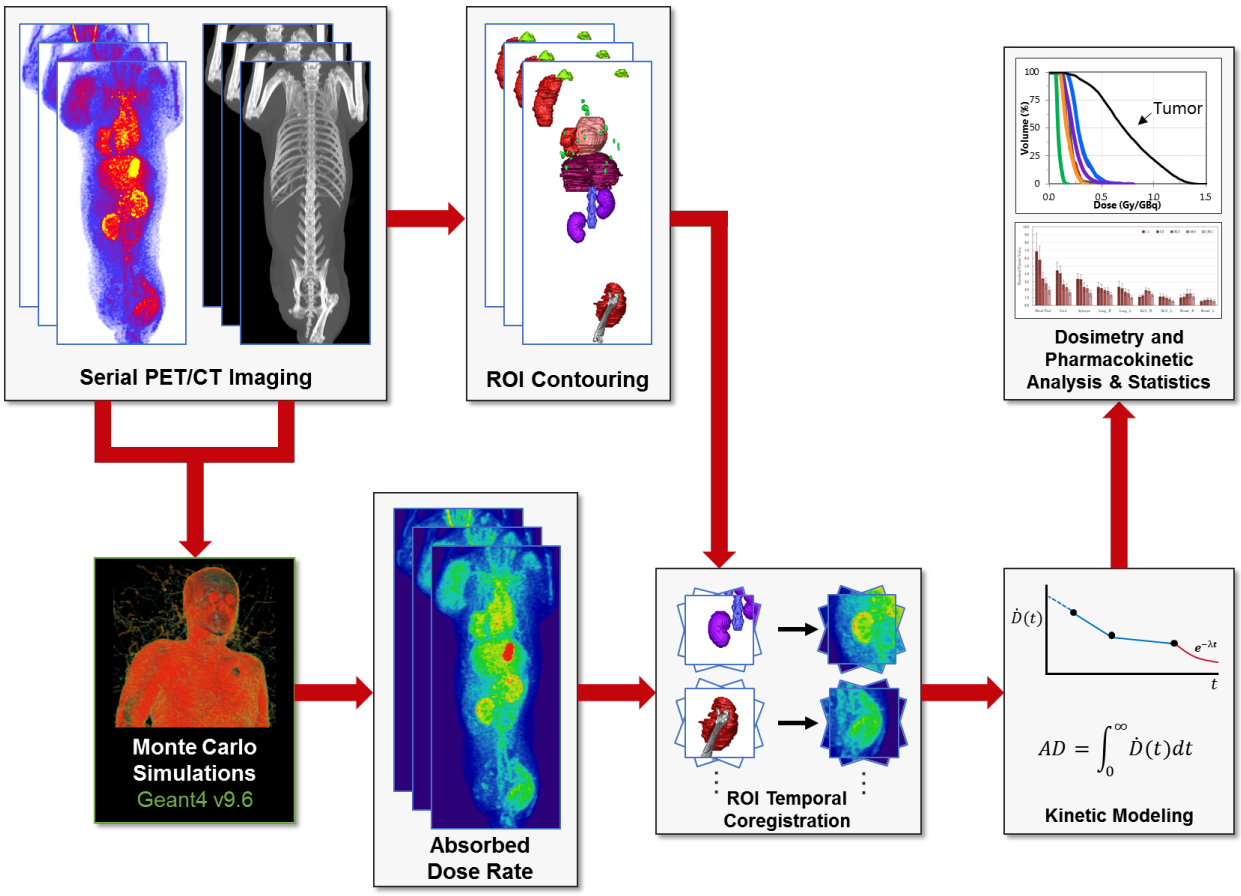

Figure 32: Overview of the RAPID workflow for theranostic dosimetry in canine patients.

5.1.6 Bone Marrow Dosimetry

Given the prolonged half-life of ^{86}Y-NM600 in blood (*17*), hematological toxicity resulting from excessive dose to the blood and red marrow is a potentially dose-limiting concern for ^{90}Y-NM600 RPT. Indeed, dose escalation studies of ^{90}Y-NM600 in mice indicate bone marrow as the likely dose-limiting organ (*19*). Excessive dose to the blood and bone marrow is additionally associated with systemic lymphopenia (*241–243*) as circulating lymphocytes are particularly radiosensitive (*244*). Given the presence of a functional immune system is essential for the tri-modal combination of EBRT + IT-IC + ^{90}Y-NM600 RPT to elicit an *in situ* vaccination response, limiting the dose to red marrow is a key treatment planning objective for prospective theranostic ^{86}Y/^{90}Y-NM600 dosimetry.

The dose delivered to bone marrow in canine patients was estimated based on the absorbed dose received by the marrow compartments of the lumbar vertebrae (L1-L4). Regional variability in marrow uptake is expected to be observed, but previous studies indicate the lumbar vertebrae is likely to provide the most conservative estimate of dose (*245–249*). In addition, a blood-based estimate of dose to the bone marrow was calculated based on the work by Jeffry Siegel (*250*). In his work, Equation 20 for ^{90}Y dose to red marrow ($D_{RM,^{90}\mathrm{Y}}$) is derived from a two component blood-based model using MIRD human phantom models.

$$D_{RM,^{90}\mathrm{Y}} = 2.10\text{E-}05\ \left[\tilde{A}_{blood}\right] \qquad 20$$

Here, $\left[\tilde{A}_{blood}\right]$ represents the blood-accumulated activity concentration in units of (MBq s/kg). A red marrow to blood activity concentration ratio (RMBLR) of 0.32 is assumed (*251*). Additionally, the dose contribution from gammas is assumed to be zero, a condition that holds true for the

primarily beta emitting ^{90}Y, which arrives at a solution for red marrow dose independent of patient mass.

5.1.7 ^{86}Y PET phantom study

A well counter calibration study in PET imaging is a quality assurance procedure to ensure accurate conversion of the observed count rate (cps) to activity concentration (Bq/ml) (*252*). The study involves imaging a large cylindrical phantom with a known activity concentration measured in a calibrated well counter and comparing the observed activity concentration in the resulting PET image with that measured by the well counter. To this end, the uniform background region from the Jaszczak phantom study, described in section 3.1.9, was used to assess the PET scanners quantification of ^{86}Y. The resulting PET images were reconstructed using VPHD (OSEM-3D), VPHD-S (OSEM-3D, PSF modeling), and VPFXS (OSEM-3D, PSF modeling, time-of-flight).

5.2 Results

5.2.1 TOF reconstruction overcorrects for scatter in PET imaging of ^{86}Y

The quantitative ^{86}Y imaging capabilities of the GE Discovery MI scanner used in this work was assessed with and without performing TOF corrections using VPFX-S and VPHD-S reconstructions, respectively. Figure 33A/B shows PET images of the uniform activity distribution in the Jaszczak phantom resulting from the two reconstruction approaches, with VPFX-S producing a significantly hotter activity distribution than that of VPHD-S. Notably, the fraction of acquired counts due to scatter that were corrected (i.e. the scatter fraction factor, SFF) in the PET scan of the Jaszczak phantom was 79.7%. In the slices shown in Figure 33A/B, a non-zero amount of activity (0.35 ± 0.04 kBq/ml) can be observed in the air surrounding the phantom in the VPFX-S image. For VPHD-S, little to no activity in air is apparent (0.03 kBq/ml). Line profile analysis across the radial dimension of the cylindrical phantom (Figure 33C) demonstrates that the higher

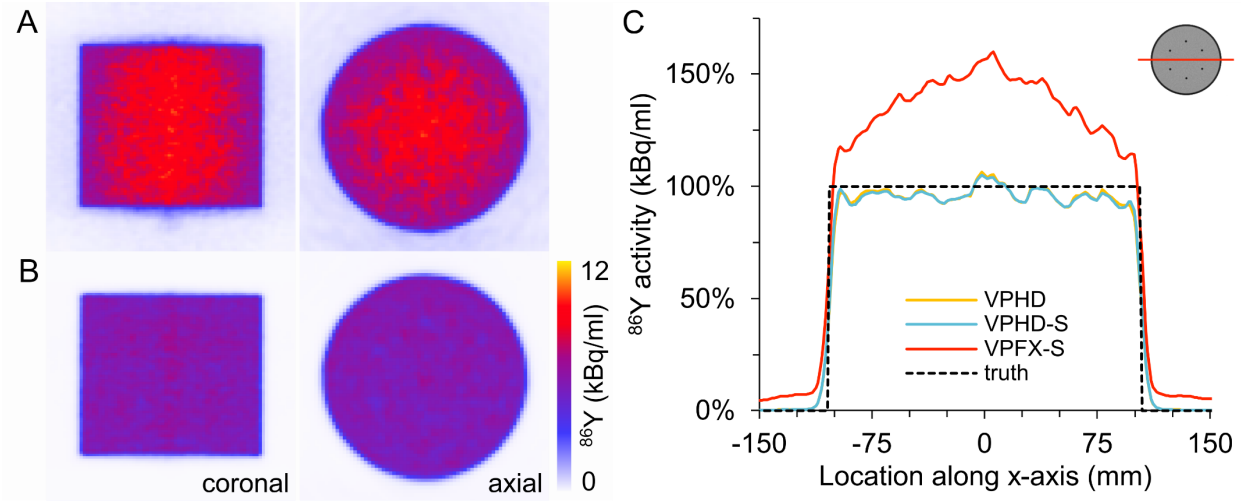

Figure 33: Coronal and axial slices of the PET imaged Jaszczak phantom containing a uniform distribution of ^{86}Y in solution and reconstructed using (A) VPFXS, with time-of-flight, and (B) VPHDS, without time-of-flight. (C) A left-right line profile through the center of each PET imaged activity distribution is shown relative to the true activity concentration. Axial slice of CT image with red line depicting the line profile through the phantom is shown on the top-right.

activity observed in the VPFX-S distribution is spatially varying with the highest activity concentration, 10.28 kBq/ml, observed along the central axis of the phantom. Using a 9 cm diameter ROI at the center of the phantom, averaged across 10 slices, the VPFX-S PET imaged activity concentration was 8.71 ± 0.42 kBq/ml. In contrast, the VPHD-S imaged activity distribution produced an average activity concentration of 5.84 ± 0.281 kBq/ml. Compared to the well counter measured activity concentration of 5.85 ± 0.03 kBq/ml (section 3.2.6), VPFX-S and VPHD-S produce a recovery factor of 148.8% and 99.7%, respectively. Notably, the VPHD PET imaged activity distribution, without SharpIR PSF modeling, showed negligible differences relative to the VPHD-S distribution in this uniform region.

The impact of TOF reconstruction on PET imaging of ^{86}Y-NM600 *in vivo* is shown in Figure 34 for a representative subject. As also observed in the phantom study, activity in air is apparent outside the patient in the VPFX-S scan and activity distribution within vital central organs appears washed out relative to the VPHD-S projection. Notably, the difference between the two PET distributions is smaller along regions central to the head of the patient, with a smaller transaxial cross-section, than that of the abdominal cavity.

Figure 35 shows the difference in ROI uptake observed from VPHD-S and VPFX-S PET distributions across all three imaging timepoints. The impact of higher observed activity in VPFX-S imaging manifests as a positive offset independent of the intensity or contrast of underlying activity. As such, lower uptake ROIs will demonstrate larger relative differences in activity than that of more highly targeted tissues (Figure 35B). Isolating this analysis on a single ROI, the marrow of the lumbar vertebrae, the impact of TOF reconstruction was assessed in each patient (Figure 36). The difference between VPFX-S and VPHD-S PET imaged marrow uptake of ^{86}Y-NM600, as measured with SUV (corrected for both body-weight and radioactive decay), increased

with patient body weight. In absolute terms, the difference in marrow uptake differed between +0.28 ± 0.03 SUV at 8 kg and +1.16 ± 0.09 SUV at 42 kg. As a result, key RPT treatment planning parameters such as the ratio of tumor to marrow uptake or dose will be lower in VPFX-S PET imaging studies, relative to VPHD-S and VPHD.

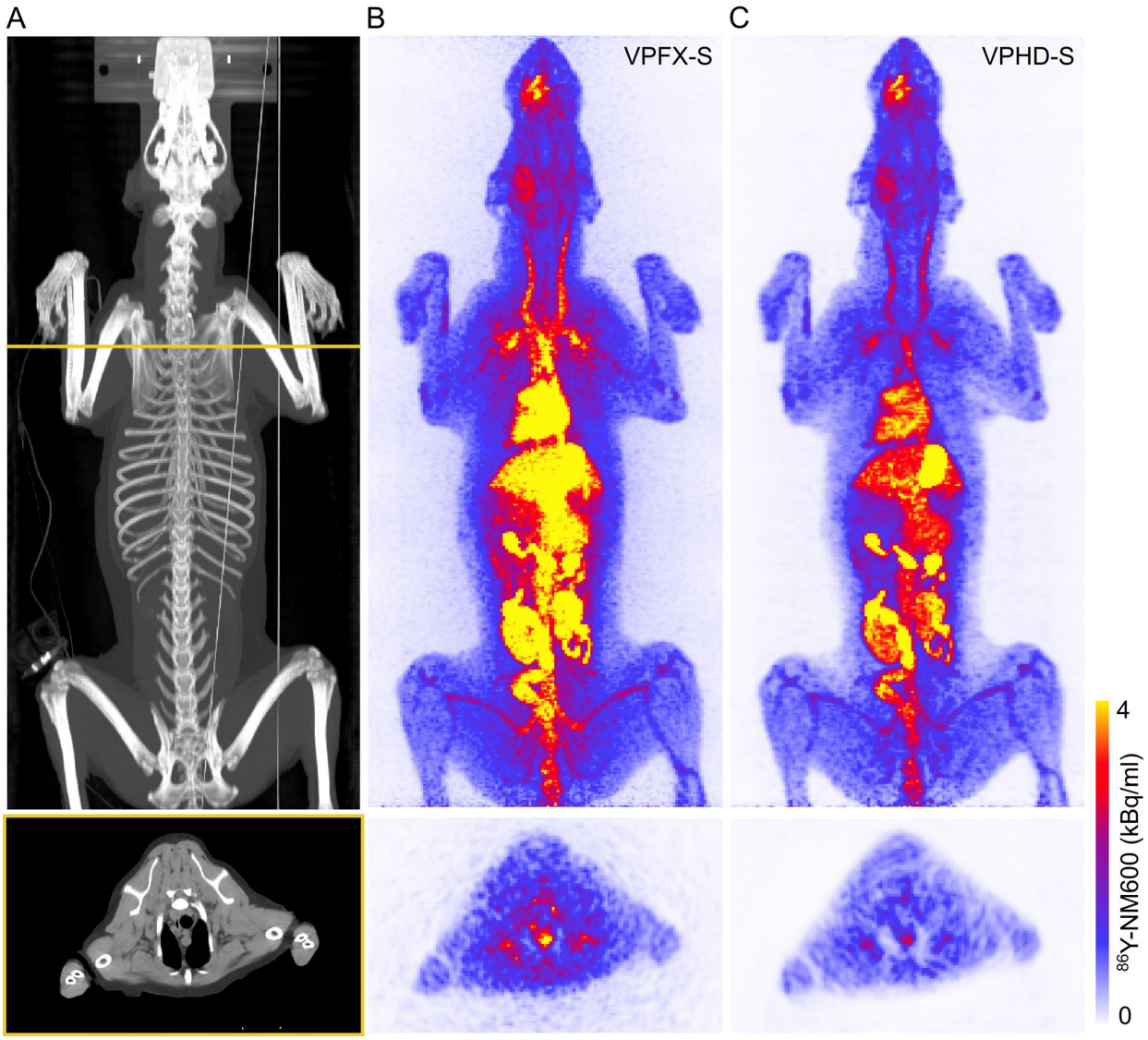

Figure 34: PET/CT images of a representative canine patient (#6) 48 h after administration of ^{86}Y-NM600. (A) Maximum intensity projection and axial slice of the CT scan with the slice location indicated in yellow. Similarly shown is the PET scan reconstructed using (B) VPFXS, with time-of-flight, and (C) VPHDS, without time-of-flight.

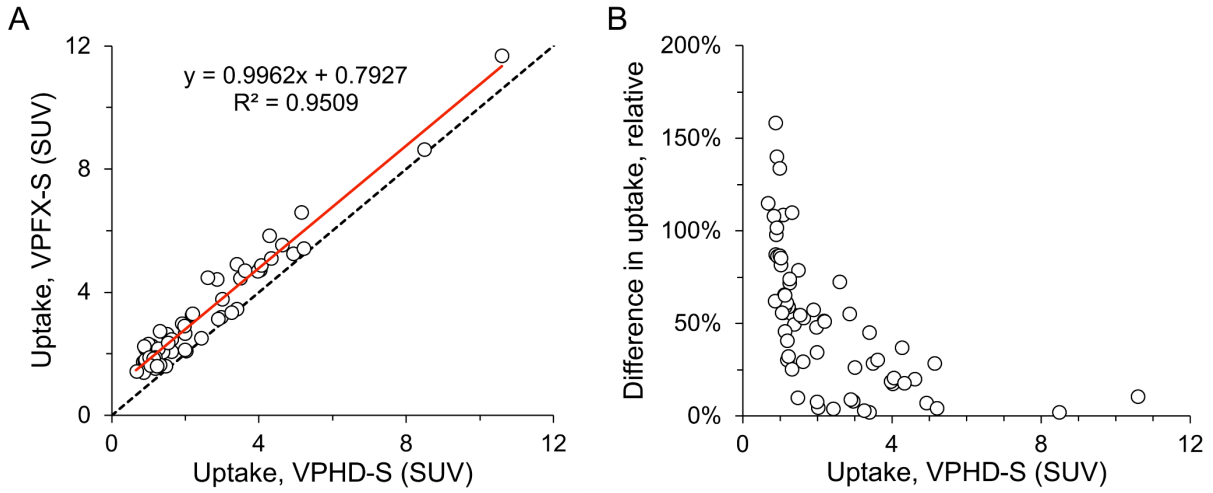

Figure 35: Difference in VPHD-S (without TOF) and VPFX-S (with TOF) PET based uptake of ^{86}Y-NM600 in all ROIs for a representative patient (#7). (A) ROI uptake for VPFX-S vs VPHD-S, where the dashed line represents equal uptake. A linear fit (red line) is shown with a slope parallel and offset to the line of unity. (B) Difference in uptake of VPFX-S measured uptake relative to that of VPHD-S.

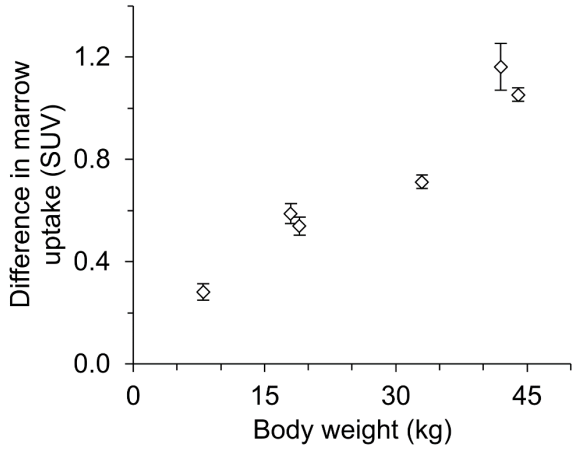

Figure 36: Absolute difference in observed uptake of ^{86}Y-NM600 in bone marrow as measured in the lumbar vertebrae from VPFX-S (with TOF) reconstructed PET relative to VPHD-S (without TOF) shown plotted against the body weight. Each point represents the average difference in marrow uptake across three timepoints with error bars for standard deviation.

5.2.2 PET imaging of ^{86}Y-NM600 in companion canines

Longitudinal PET-CT imaging of canine patients was performed over the course of 48-72 h after administration of ^{86}Y-NM600. Patient 3 received a final PET/CT scan at 72 h instead of 48 h. Table 11 provides an overview of all canine patients taking part in the study (n = 6). The body weight of canine patients, as measured prior to imaging and imaging, ranged between 8.4 to 44.6 kg. Five of six canine patients presented with late stage melanoma as well as metastatic spread. Canine patient #1 presented with osteosarcoma, but otherwise met inclusion criteria for the study. The administered activity of ^{86}Y-NM600 ranged between 4.82 to 7.98 mCi (178 to 295 MBq). An overview the PET-CT imaging in each canine patient and the targeted tumors therein is shown in the following pages (Figure 37-Figure 41). The SFF observed in canine patient scans ranged between 70.0% and 82.7% (mean, 74.3 ± 3.7, n = 21).

Table 11: Overview of canine patients undergoing ^{86}Y-NM600 PET/CT imaging and prospective theranostic dosimetry.

Patient ID	Breed	Age, Sex Weight	Primary/Index tumor (TNM staging)	Distant lesions	^{86}Y-NM600 administered
1	Cane Corso	MN, 5 y 44.6 kg	Metastatic Osteosarcoma (TxN0M1)	Pulmonary nodules, left proximal humerus	4.82 mCi (178 MBq)
2	Cocker Spaniel	MN, 9 y 18.2 kg	Oral Melanoma (T2N1M1)	Pulmonary nodules, mandibular LN	5.08 mCi (188 MBq)
3	Miniature Schnauzer	FS, 7 y 8.4 kg	Oral Melanoma (T1N1M1)	Regional LN, Pulmonary nodule	5.29 mCi (196 MBq)
4	Labrador Retriever	MN, 9 y 42.0 kg	Oral Melanoma (T2N1M1)	Regional LN and pulmonary nodules	7.98 mCi (295 MBq)
5	Mixed Breed	FS, 10 y 19.0 kg	Metastatic Subungual Melanoma (TxN2M1)	Pulmonary mass, Jejunal mass	7.10 mCi (263 MBq)
6	Mixed Breed	MN, 11 y 33.0 kg	Oral Melanoma (T2N2M1)	Regional LN, lung, abdominal	6.40 mCi (237 MBq)

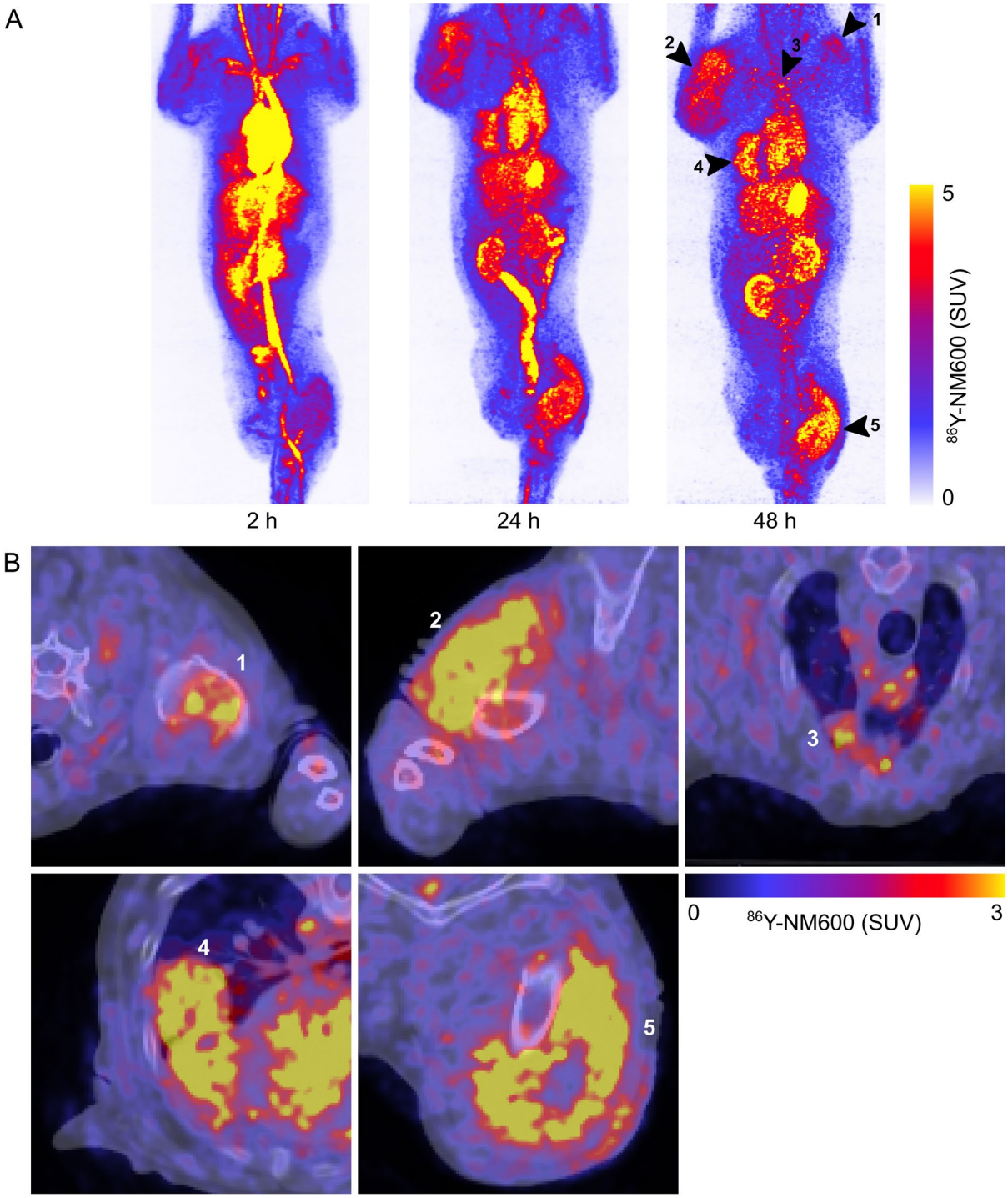

Figure 37: Canine patient 1. (A) Maximum intensity projections of VPHD PET images at each timepoint. (B) Axial slices of targeted tumors indicated with arrows at the final timepoint.

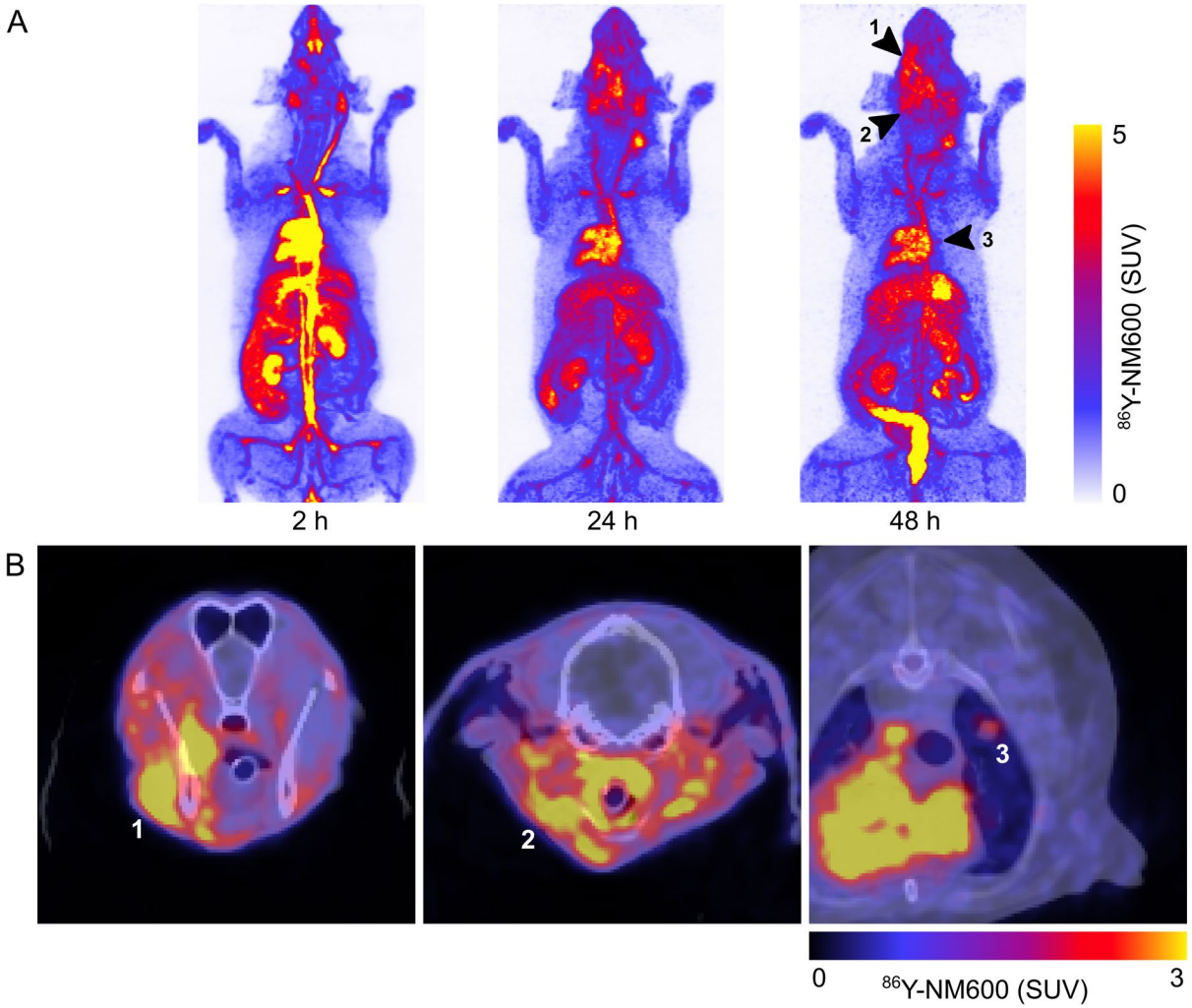

Figure 38: Canine patient 2. (A) Maximum intensity projections of VPHD PET images at each timepoint. (B) Axial slices of targeted tumors indicated with arrows at the final timepoint.

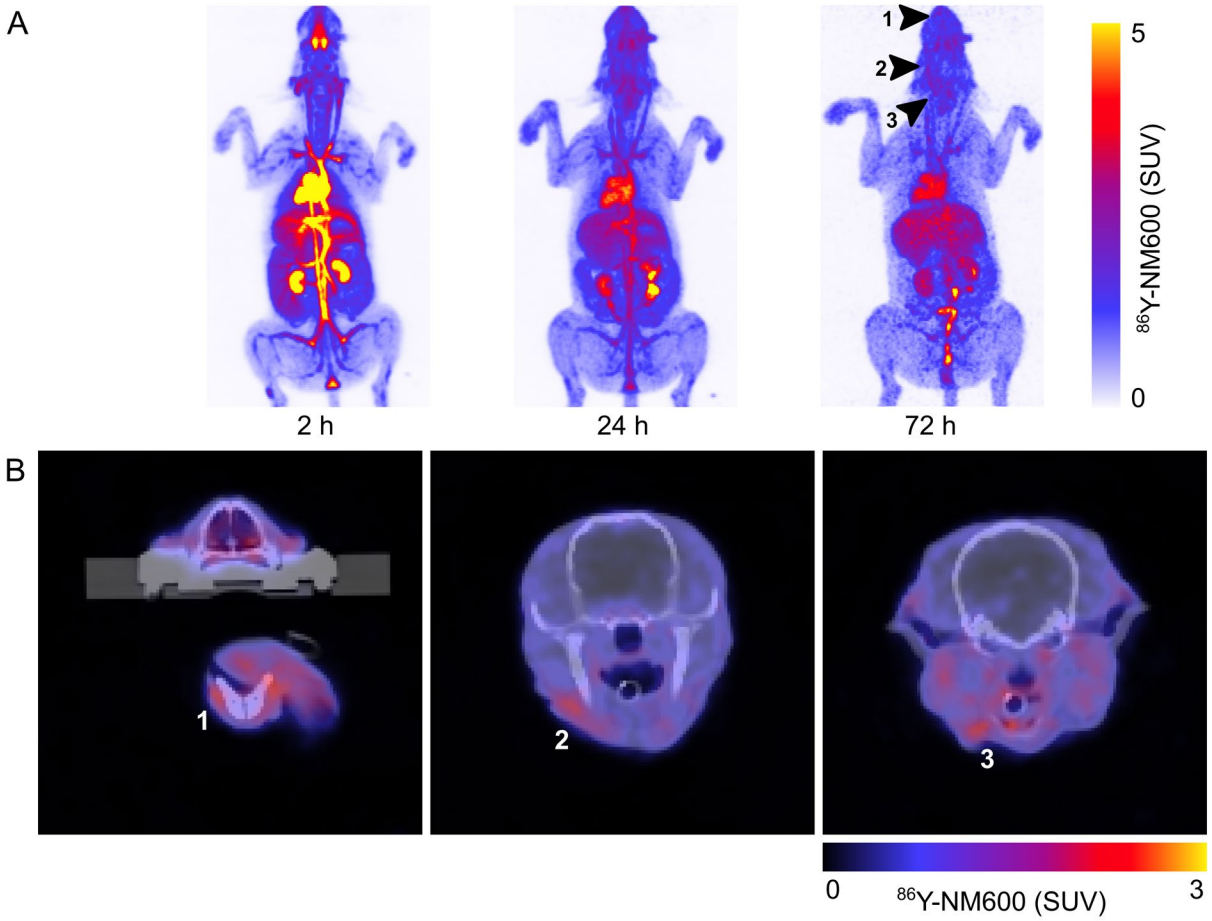

Figure 39: Canine patient 3. (A) Maximum intensity projections of VPHD PET images at each timepoint. (B) Axial slices of targeted tumors indicated with arrows at the final timepoint.

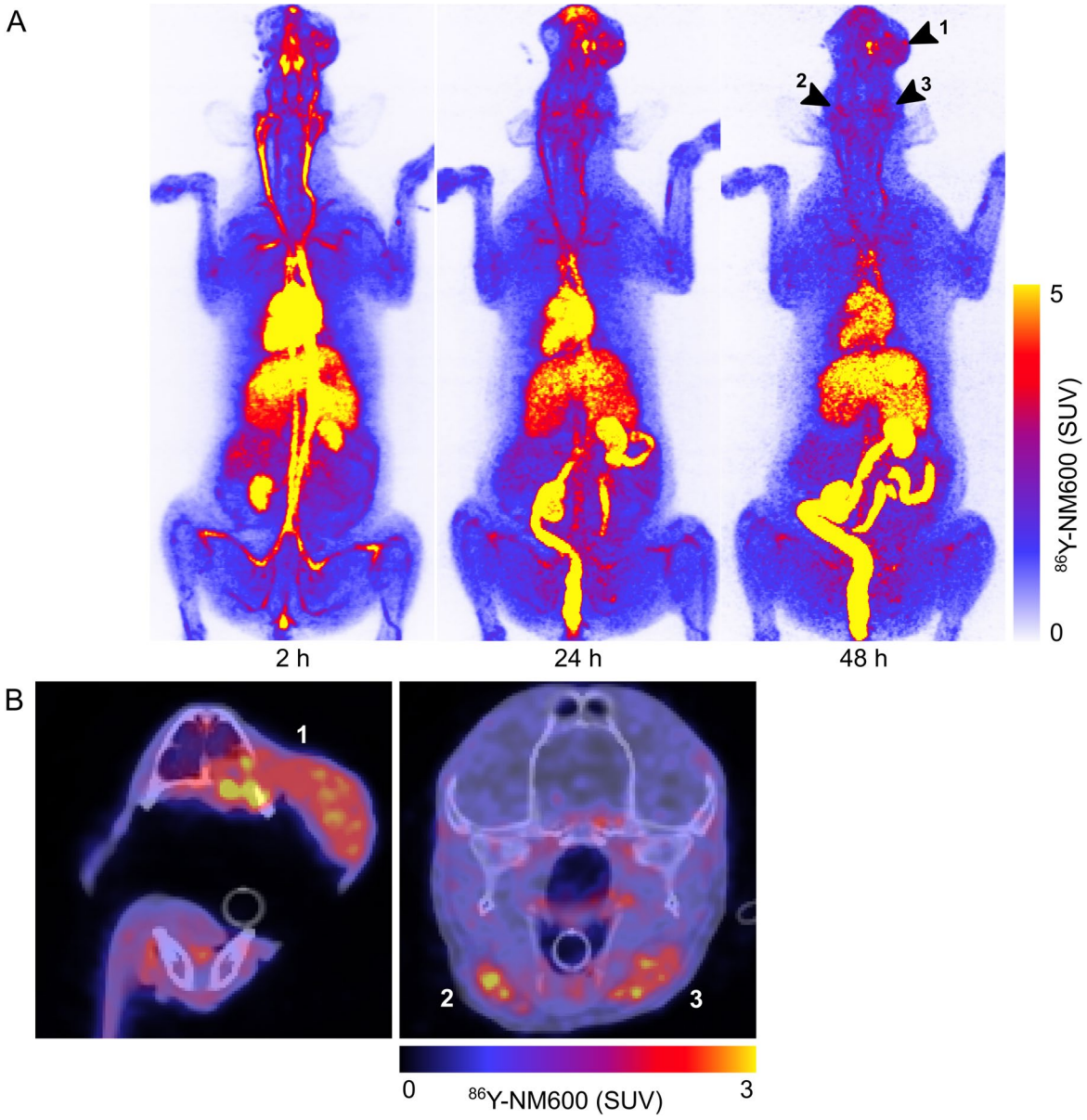

Figure 40: Canine patient 4. (A) Maximum intensity projections of VPHD PET images at each timepoint. (B) Axial slices of targeted tumors indicated with arrows at the final timepoint.

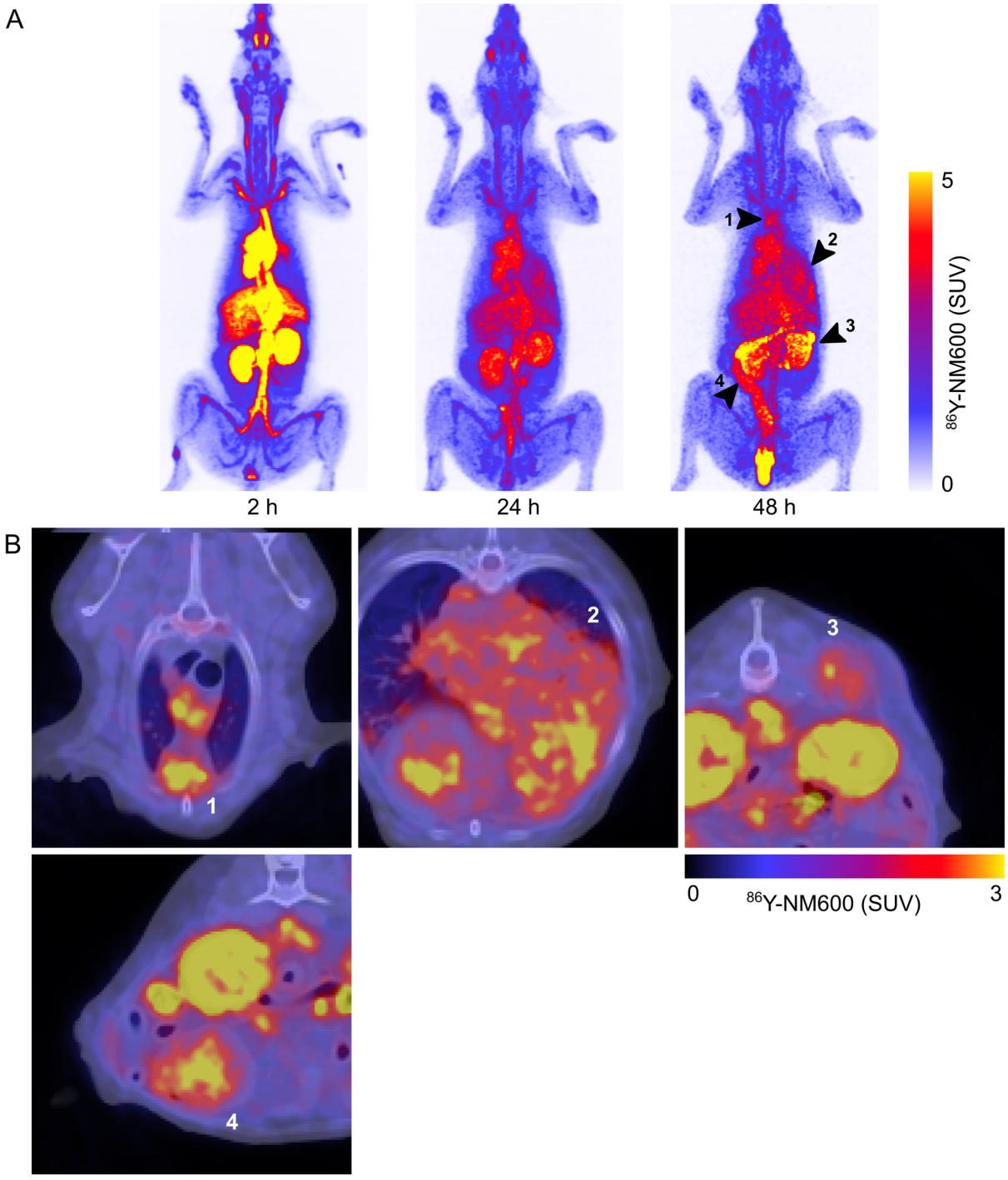

Figure 41: Canine patient 5. (A) Maximum intensity projections of VPHD PET images at each timepoint. (B) Axial slices of targeted tumors indicated with arrows at the final timepoint.

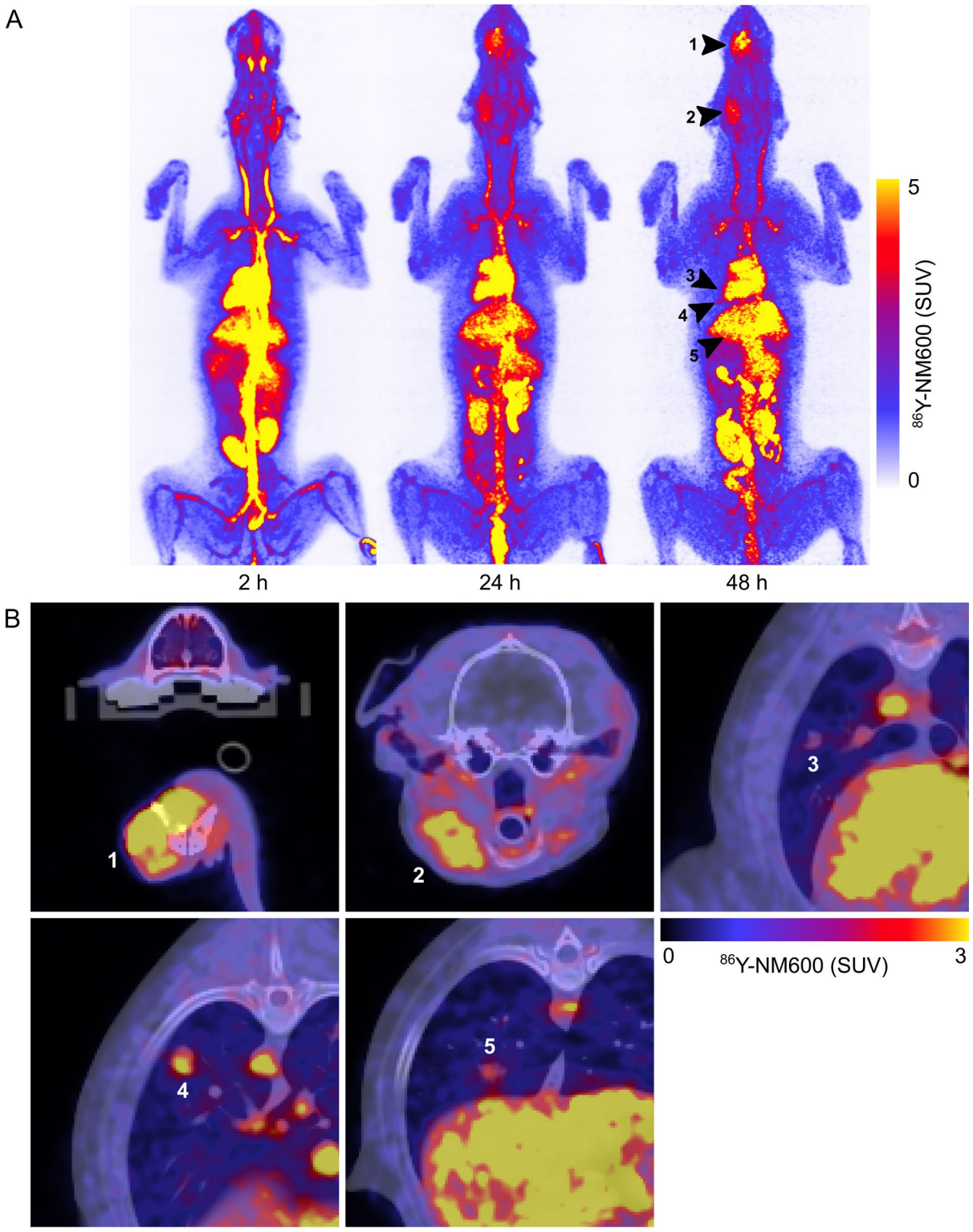

Figure 42: Canine patient 6. (A) Maximum intensity projections of VPHD PET images at each timepoint. (B) Axial slices of targeted tumors indicated with arrows at the final timepoint.

The biodistribution of ^{86}Y-NM600 through 48-72 h of PET-CT imaging in canine patients is shown in Figure 43. In contrast to preclinical studies in mice (section 3.2.1), kidney uptake at 48 h (3.94 ± 0.96 SUV) was higher than that of the liver (2.93 ± 0.53 SUV). Additionally, canine patients exhibited significant uptake and accumulation of ^{86}Y-NM600 in the gallbladder, reaching an average concentration of 6.53 ± 3.34 SUV. The extent to which ^{86}Y-NM600 accumulated in the gallbladder varied significantly across canine patients (3.39 to 10.36 SUV), suggesting that underlying physiological or environmental conditions may functionally impact the hepatobiliary metabolism of ^{86}Y-NM600 in canines. The evidence for hepatobiliary clearance of ^{86}Y-NM600 is further supported by the apparent uptake and accumulation of the compound in feces over the course of the 48-72 h imaging series. The spleen, lungs, and marrow (lumbar vertebrae) all exhibited non-specific uptake of ^{86}Y-NM600 at 1.42 ± 0.11 SUV, 0.83 ± 0.07 SUV, and 1.00 ± 0.12 SUV, respectively, 48 h post-injection.

Tumor uptake of ^{86}Y-NM600 across all canine patients varied between patient and site of disease (Figure 44). The time of peak uptake appeared to vary between 24 and 48 h post injection, with patient #3 demonstrating durable retention of ^{86}Y-NM600 out to 72 h. Targeted lung metastases exhibited the weakest uptake of all tumor sites, ranging between 1.34 to 1.91 SUV at 48 h post-injection. Given the small size of the lesions (0.49 to 5.48 ml) and intrafraction breathing motion, lower observed uptake in lung metastases is expected. Excluding lung metastases, the average uptake of tumors at 48 h post-injection was 2.41 ± 0.49 SUV, with the highest uptake being observed (3.32 SUV) at 24 h in patient 6. All tumors exhibited uptake greater than that observed in marrow by 48 h and the tumor-to-marrow ratio of uptake, excluding lung metastases, was 2.52 ± 0.46.

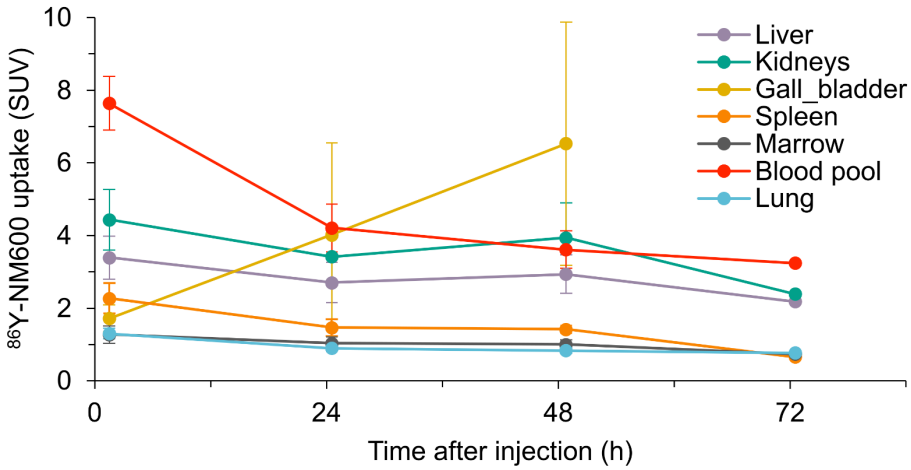

Figure 43: ROI analysis of ^{86}Y-NM600 uptake in normal tissues of canine patients (n = 6) based on VPHD PET imaging. The final imaging timepoint for patient #3 was 72 h instead of 48 h and exhibited atypical gallbladder uptake (not shown). Kidneys represent an average of the left and right kidney uptake in each patient. Marrow uptake was assessed in the lumbar vertebrae. Error bars shown for standard deviation.

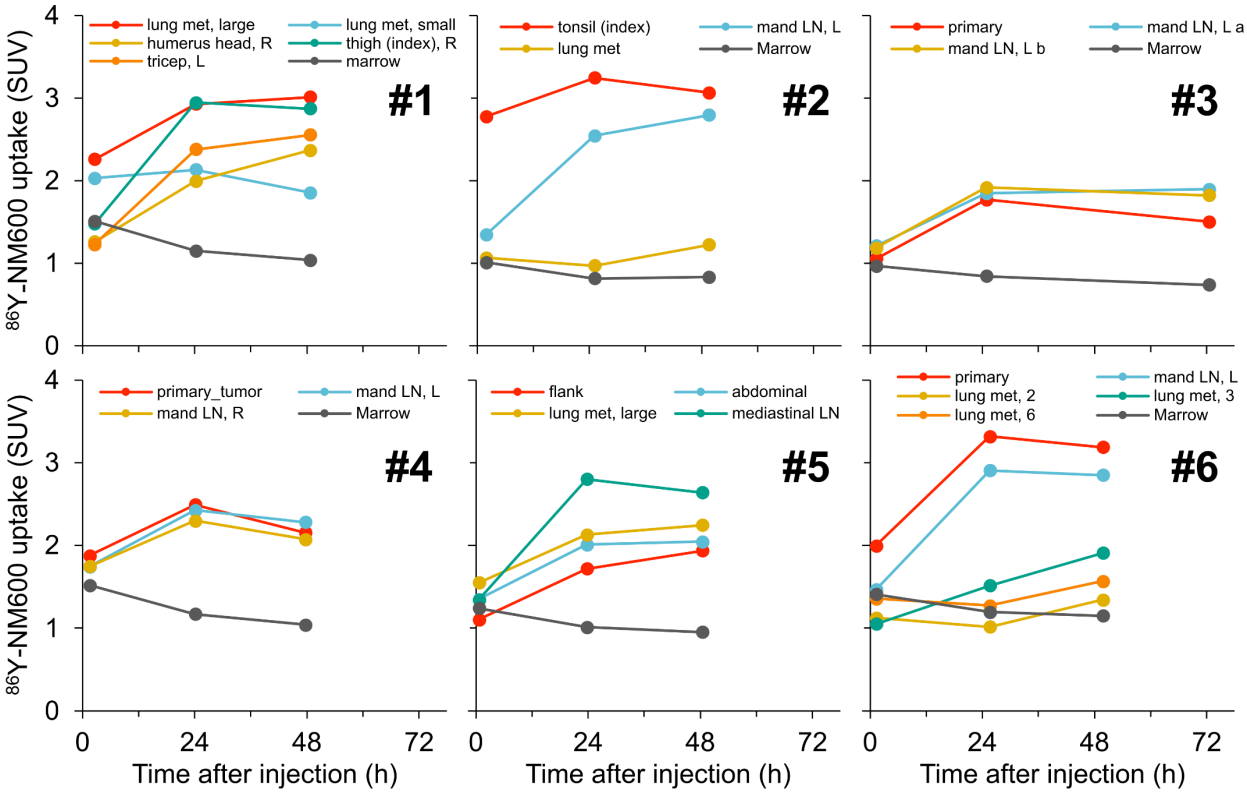

Figure 44: Individual uptake of ^{86}Y-NM600 in primary and metastatic tumors of canine patients targeted for prospective dosimetry. Canine patient ID is located in the top-right of each time-activity curve. Uptake in marrow of the lumbar vertebrae is shown for reference. Data shown is based on VPHD PET images

The blood activity concentration was assessed using both ex vivo blood draws prior to imaging and in vivo ROI analysis of the ascending aorta in the heart of PET-CT image volumes. Figure 45 shows a comparison of each measurement approach in a single representative canine patient. ^{86}Y-NM600 exhibits an initial rapid distribution phase followed by prolonged clearance from the blood. As such, the greatest difference between ex vivo and in vivo measurements (-24% ± 9%, n = 5) occurred immediately following administration of ^{86}Y-NM600 at the first 2 h imaging timepoint. By the final timepoint, this difference was reduced to -9% ± 11%. Given that the blood draws took place prior to imaging, marginally higher activity concentration in ex vivo measurements are to be expected. However, because the exact time of the blood draw was not accounted for, an offset of 15 minutes was assumed for all blood draw times if not explicitly recorded. A summary of the estimated biological half-life calculated from both in vivo VPHD PET and ex vivo blood draw measurements is provided in Table 12. Notably, the average half-life of 34.3 ± 4.2 h derived from VPHD PET was similar to that of 33.1 ± 5.8 h observed in tumor bearing mice. However, the average half-life of 28.5 ± 5.5 h from blood draw measurements suggests that ^{86}Y-NM600 clears from the blood more rapidly. Note that no blood draw measurements were available for patient 4.

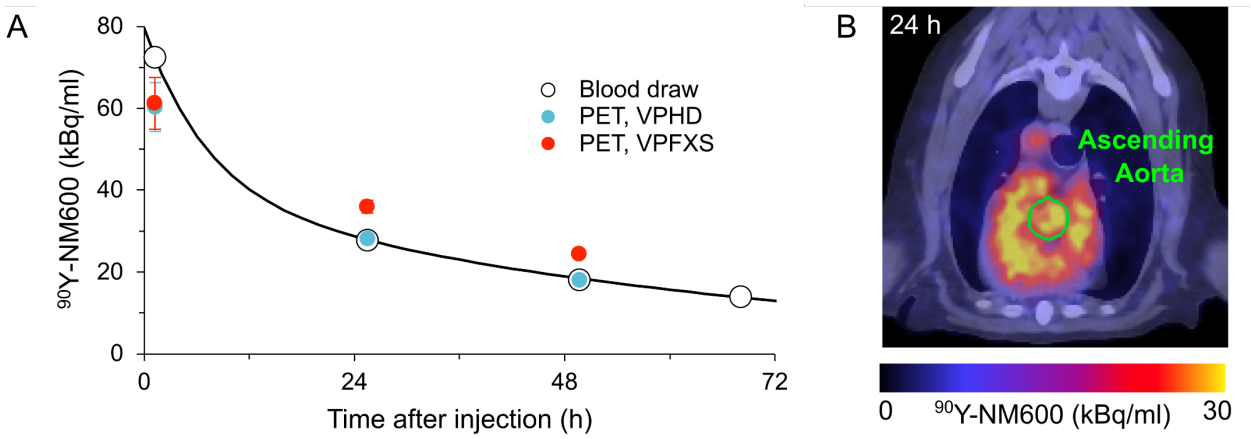

Figure 45: (A) Estimated blood activity concentration of ^{90}Y-NM600 based on decay corrected measurements of ^{86}Y-NM600 as measured via ex vivo blood draw measurements and in vivo VPHD or VPFX-S PET-CT imaging in a representative canine patient. Error bars shown for standard deviation. Bi-exponential fit of the blood draw data shown for reference. (B) Blood activity concentration in PET/CT image volumes was measured using an ROI of the ascending aorta, shown in green.

Table 12: Biological half-life of 86Y-NM600 in blood of tumor canine patients based on a mono-exponential fit.

	$t_{1/2}$ (h)	
Patient ID	**Blood draw**	**VPHD PET**
1	33.0	31.9
2	27.9	36.9
3	25.2	29.2
4	-	34.8
5	21.5	32.1
6	34.8	41.0
	28.5 ± 5.5	34.3 ± 4.2

5.2.3 Lung metastases dosimetry and the impact of PVC

An alternate dosimetry approach for lung metastases was pursued using the PVC methods developed in this thesis. Figure 46 provides an overview of the impact of iterative deconvolution (VPHD-LR) on PET uptake. Application of LR deconvolution successfully sharpens the spatially varying activity distribution in and around the target lesion, increasing activity concentration by over 20% in some voxels. On an ROI level, this culminates in an increase of 2.9% to 8.0% in uptake at the 48 h timepoint. The magnitude of the impact of LR iterative deconvolution was unique to each tumor, but generally increased with time as a gradually larger tumor-to-lung ratio provided a greater contrast between the tumor and background.

In order to overcome partial volume effects due to intrafraction motion introducing activity into low density regions, lung met dosimetry in this analysis was performed by using the whole-body mask to override the density of tissue in the body to be that of water (e.g. unit density, 0 HU). Figure 47 shows the difference between MC simulations run with CT-based density and water density as well as the impact on lung metastases dosimetry. Higher dose rates can be observed in low density lung voxels as well as the air cavity within the trachea. Note the substantially higher doses peripheral to the lung met ROI where spill out activity due to partial volume effects is present. Rx Dose estimates for ^{90}Y-NM600 RPT in lung metastases using MC simulations based on geometry models from CT-based density were 82% ± 52% higher than that of unit density-based geometry models and 125% ± 74% higher than OLINDA-based estimates. In contrast, Rx dose estimates based on the unit-density model were 23% ± 6% higher than OLINDA estimates.

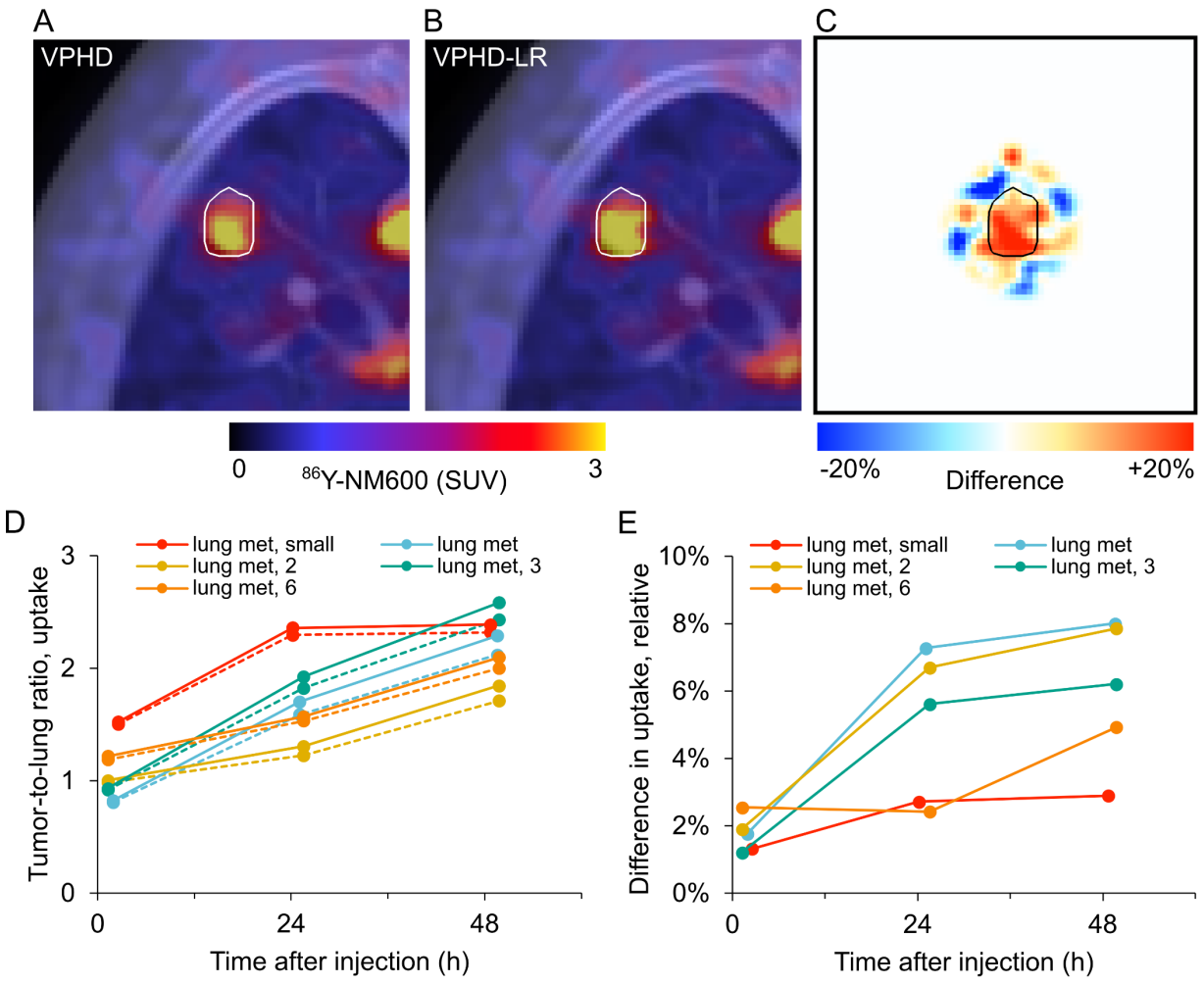

Figure 46: Impact of iterative deconvolution with VPHD-LR. Axial slices of ^{86}Y-NM600 PET-CT image volumes show for (A) VPHD and (B) VPHD-LR as well as the (C) difference map between VPHD and VPHD-LR in a representative lung metastasis at 48 h (#6, lung met 3). (D) Tumor-to-lung ratio of uptake for small lung metastases encountered across all canine patients. Dashed and solid lines represent VPHD and VPHD-LR derived uptake, respectively. (E) The relative difference in uptake due to application of LR within each tumor at each timepoints.

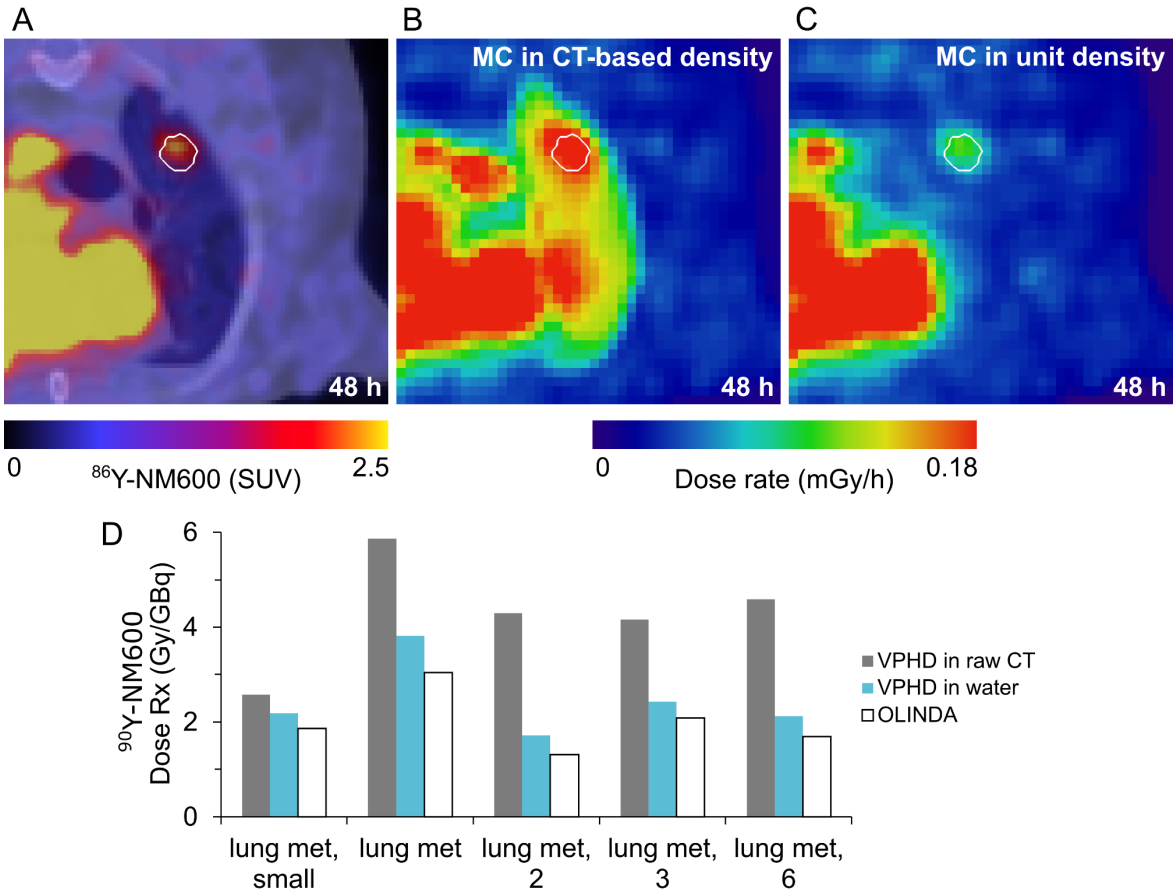

Figure 47: Impact of CT density on lung met dosimetry. (A) Axial slice showing the VPHD PET imaged activity distribution overlayed on the CT at 48 h post-injection for a representative lung metastasis case (#2, lung met). Dose rate maps resulting from MC simulation using (B) CT-based density and (C) unit density. (D) A comparison of the final mean Rx dose calculated from each method for small lung metastases encountered across all canine patients. OLINDA sphere-model estimates of tumor dosimetry shown for reference.

The results of VPHD-LR+PVC lung met dosimetry are shown in Figure 48. The effective partial volume correction observed as the relative difference between VPHD-LR and VPHD-LR+PVC time-dose-rate curve ranged between 38% and 83% across all targeted lung metastases. This correction factor was greatest at the 48 h timepoint (65% ± 18%), where the tumor-to-lung ratio was greatest. VPHD-LR alone increased the estimated Rx Dose for ^{90}Y-NM600 RPT by 2.9% ± 1.1% while VPHD-LR+PVC was 59.6% ± 18.6%, relative to results based on VPHD. A summary of all dosimetry estimates for all lung metastases studied in this work is shown in Table 13. For ^{90}Y-NM600 RPT treatment planning purposes, lung met dosimetry derived from the VPHD-LR+PVC approach was utilized.

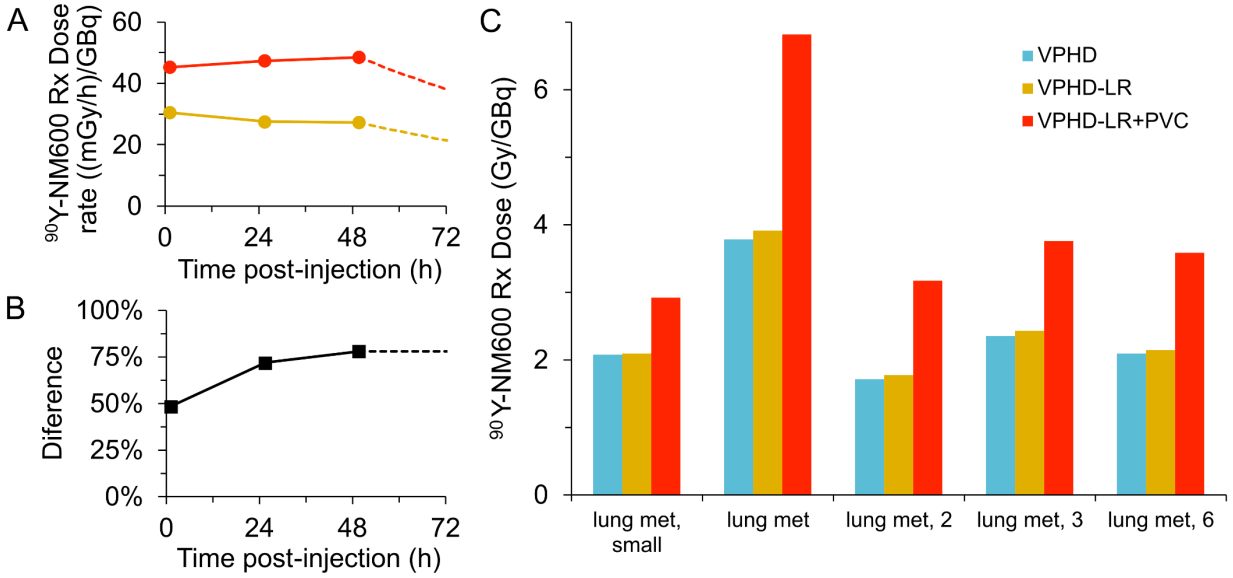

Figure 48: Impact of partial volume correction approaches on lung metastases dosimetry. (A) Mean dose rate curves for a representative lung metastasis (#2, lung met) resulting from VPHD-LR and VPHD-LR+PVC as well as (B) the relative difference between the dose-rate curves. (C) The final mean dose to each lung metastasis undergoing dosimetric analysis from each approach. Dosimetry results from VPHD shown for reference.

Table 13: Summary of dosimetry estimates for lung metastases targeted in canine patients. All dosimetry results shown based on unit density-based MC simulations.

		^{90}Y-NM600 Rx Dose (Gy/GBq)		
Patient ID	**Targeted tumor**	**VPHD**	**VPHD-LR**	**VPHD-LR+PVC**
#1	lung met, small	2.19	2.21	2.93
#2	lung met, small	3.82	3.97	6.82
#6	lung met, 2	1.72	1.78	3.18
#6	lung met, 3	2.42	2.51	3.76
#6	lung met, 6	2.12	2.17	3.59

5.2.4 Dosimetric Impact of Temporal Coregistration

The impact of the temporal coregistration methods on canine patient dosimetry were investigated for whole-body registration (WBR) and locoregional registration (LRR) as well as WBR+DIR and LRR+DIR (deformable image registration). Figure 49 shows analysis of ROI overlap in tumors and liver target volumes. In all cases, the application of DIR improved registration accuracy of target volumes with the highest DSC achieved with LRR+DIR. Additionally, the registration accuracy for LRR was greater than that of WBR for both tumor and Liver ROIs. The improvement derived from the application of DIR to the WBR approach in tumors was 26.6% ± 36.7% and 23.3% ± 14.2% for the liver. Smaller increases in registration accuracy were observed in tumor (+5.2% ± 10.9 %) and liver (17.6% ± 16.8%) for the application of DIR to the LRR approach.

Figure 50 shows the dosimetric impact of the developed temporal coregistration approaches on the multi-timepoint dosimetry performed for canine patients in this work. As expected, the WBR approach generated the widest range in D_{90}, -19.7% to 3.0% for tumors and -9.5% to 3.3% for the liver. Notably, a PTV defined by the reference ROI consistently produced the lowest D_{90} estimates in tumors, but he highest D_{90} estimates in the liver. The key difference between the two ROIs being the presence of even higher uptake tissue adjacent to the target volume. In the case of the liver, this was the gallbladder. For a PTV defined by the intersection of ROIs from each timepoint, voxels belonging to the gallbladder at any timepoint is effectively removed from dosimetric analysis. For a PTV defined by the reference ROI at the final timepoint, the presence of highly active gallbladder voxels within the liver PTV results in a lower D_{90} than that of the intersection of ROIs. For targeted tumor volumes, the application of DIR to WBR achieved similar results to LRR+DIR in some cases but remained substantially different for some

target volumes. This suggests that the improved accuracy from the LRR registration achieved a more advantageous initial position for the successful application of DIR in canine patient anatomy. Notably, the same was not true for targeted liver volumes, which achieved dosimetric accuracy comparable to the LRR+DIR approach.

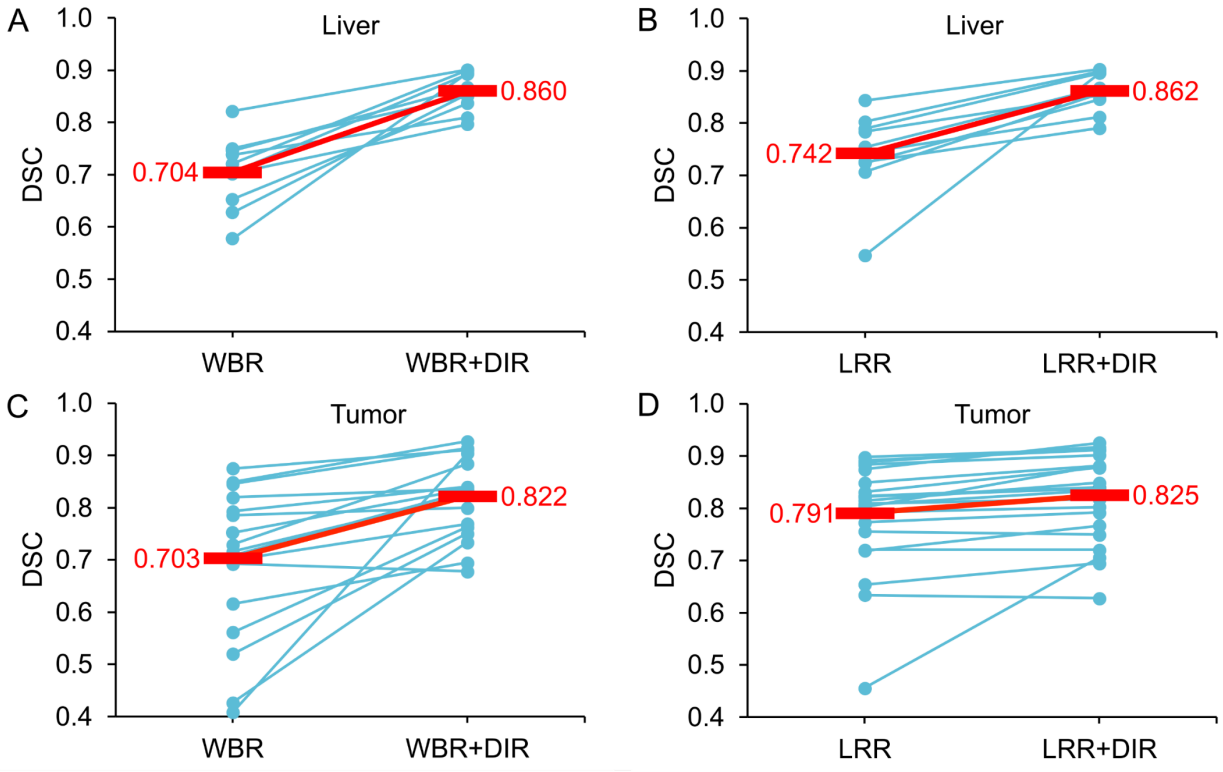

Figure 49: Registration accuracy of WBR, WBR+DIR, LRR, and LRR+DIR registration approaches, as measured via Dice similarity coefficient (DSC), in targeted tumor and liver volumes. Improved registration from the application of DIR to WBR and LRR (A, B) liver and tumor (C, D) ROIs. Red line and markers represent the mean registration accuracy in each case.

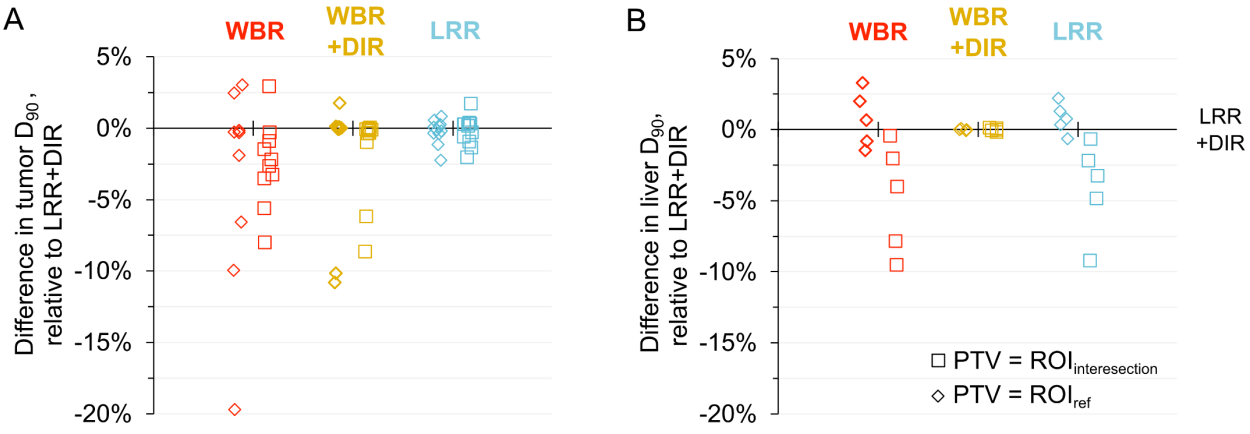

Figure 50: The dosimetric impact of the developed registration approaches on canine patient dosimetry, in terms of D_{90}, in both (A) tumor and (B) liver target volumes.

5.2.5 Clinical implementation of theranostic ^{86}Y/^{90}Y-NM600 tumor dosimetry

Prospective dosimetry and treatment planning for prescription of low-dose ^{90}Y-NM600 RPT was performed in six canine patients over the course of 2.5 years. Implementation of the RAPID workflow commenced immediately following the initial PET-CT scan and physician drawn contours were delivered within 1-2 business days of the final 48-72 h imaging timepoint. The requisite simulation time for a single timepoint ranged between 5.6 and 27.6 h with the total number of source voxels in a patient scaling with body weight (0.68 ± 0.08 h/kg). A dosimetry report on each canine patient was generated within 4 to 11 days (mean, 7.5 ± 2.3) from the first imaging timepoint.

Normal tissue dosimetry in primary organs at risk across all canine patients is presented in Figure 51. The kidneys and liver, previously indicated as the primary clearance pathways, received the highest normalized Rx Dose at 181.7 ± 43.4 Gy/(GBq/kg) and 139.4 ± 25.9 Gy/(GBq/kg), respectively. The spleen received 68.9 ± 13.0 Gy/(GBq/kg) while marrow of the lumbar vertebrae received 41.1 ± 6.6 Gy/(GBq/kg).

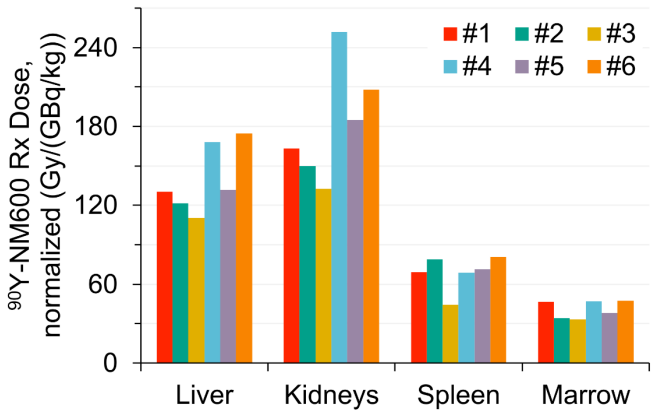

Figure 51: Normal tissue dosimetry for ^{90}Y-NM600 in at-risk organs of all canine patients. Data shown in terms of normalized Rx Dose. Marrow represents dose to marrow in the lumbar vertebrae.

Further analysis of marrow dosimetry was performed using blood-based dosimetry approaches (Figure 52). Marrow dose estimates based on the VPHD PET-CT imaged marrow were consistently more conservative than that of blood-based dosimetry (+51% ± 39%), with the relative difference increasing with patient weight. The average normalized Rx Dose to marrow derived from ex vivo blood-based marrow dosimetry was 28.6 ± 5.16 Gy/(GBq/kg). Blood-based marrow dosimetry using in vivo VPHD PET-CT estimates of blood activity concentration was 88% ± 8% of ex vivo blood-draw estimates, requiring a correction factor of 1.15 ± 0.10. Table 14 provides an overview of the marrow dosimetry estimates determined for canine patients in this study.

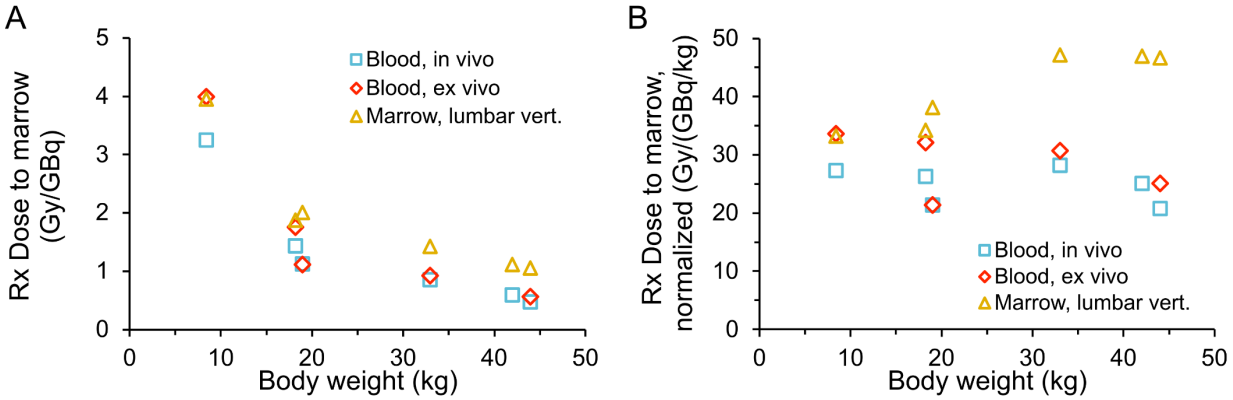

Figure 52: Marrow dosimetry estimates as measured via ex vivo blood draw measurements, in vivo blood ROI analysis, and in vivo marrow (lumbar vertebrae) dosimetry. Rx dose estimates shown in terms of (A) Gy/GBq and (B) Gy/(GBq/kg)), normalized by body weight.

Table 14: Summary of bone marrow dosimetry estimates in canine patients

	Rx Dose to marrow (Gy/GBq)		Normalized Rx Dose to marrow (Gy/(GBq/kg))	
Patient ID	**Blood-based, ex vivo**	**Marrow, lumbar vert.**	**Blood-based, ex vivo**	**Marrow, lumbar vert.**
#1	0.57	1.06	25.1	46.65
#2	1.77	1.88	32.1	34.26
#3	4.00	3.96	33.6	33.22
#4	-	1.12	-	46.93
#5	1.12	2.01	21.4	38.16
#6	0.93	1.43	30.7	47.17
			28.6 ± 5.2	41.1 ± 6.6

A comprehensive summary of tumor dosimetry in all canine patients is presented in Figure 53 where cumulative DVH curves are presented based on the intersection of temporally coregistered target ROIs. The characteristically heterogeneous dose distribution resulting from ^{90}Y-NM600 RPT is apparent from the sloped DVH curves with an average D_{98}/D_2 dose heterogeneity factor of 0.62 ± 0.10, where a value of 1.0 represents a uniform dose distribution. Canine patient 4 exhibits an extreme case of this heterogeneity as a subregion of the primary tumor was substantially hotter than regions elsewhere in the PTV (Figure 40B depicts the heterogeneous uptake of ^{86}Y-NM600 this tumor). Additionally, the dose delivered to tumors often varied substantially between sites of disease within canine patients. The voxel level dosimetry estimates for lung lesions, when present, from VPHD-LR PET in unit density background exhibited the lowest dose DVH profile of all tumors analyzed in canine patients 1, 2, and 6. Figure 53G presents the lung metastases dosimetry based on VPHD-LR+PVC where the Rx Dose is more similar to that of other targeted lesions in the patient. However, the Rx Dose delivered by targeted tumor volumes was still greater than that received by the marrow in all cases, where the marrow of the lumbar vertebrae represents the most conservative estimate of dose to the bone marrow. Notably, smaller target volumes, such as lymph nodes (LN) and lung metastases, containing fewer voxels within the PTV defined by the intersection of these ROIs resulted in markedly jagged DVH profiles.

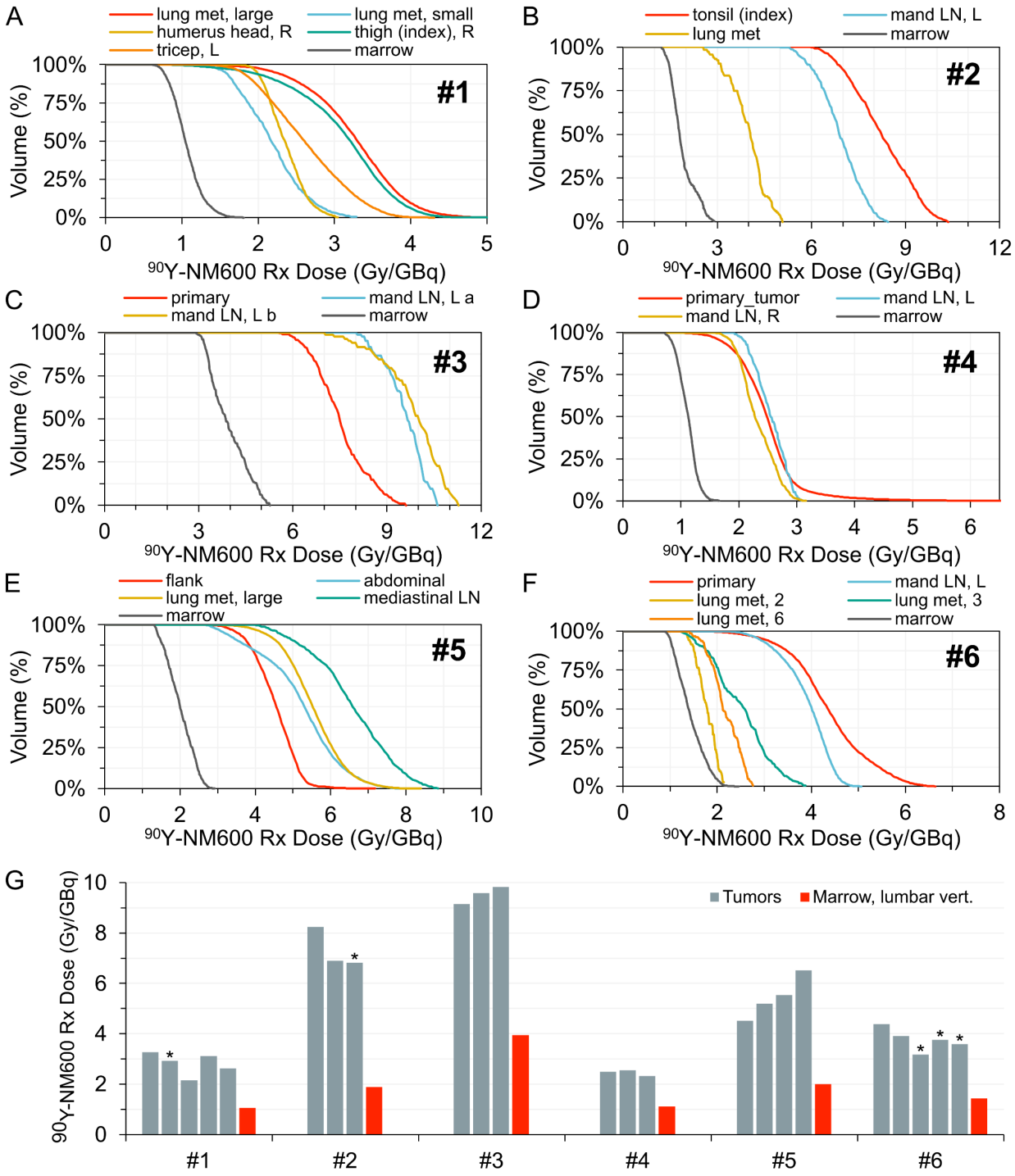

Figure 53: Tumor and marrow (lumbar vertebrae) dosimetry for ^{90}Y-NM600 in all canine patients. (A-F) Cumulative DVH curves and (G) final mean dose calculated for each target volume. Marrow dose to lumbar vertebrae shown for reference. '*' indicates lung met dosimetry as determined via VPHD-LR+PVC.

For treatment planning purposes, a tumor-to-marrow ratio of >2.0 for the tumor receiving the minimum amount of dose in the subset of tumors was desirable. Figure 54 provides an overview of the minimum tumor-to-marrow ratio in each canine patient, considering both blood-based and image based marrow dosimetry approaches. Using dosimetry estimates for marrow in the lumbar vertebrae, the tumor-to-marrow ratio ranged between 2.03 and 4.38 (2.73 ± 0.57) across all canine patients. In this context, a maximum tolerable dose of between 4.06 and 7.24 Gy (to the tumor receiving the least amount of dose) could be delivered to tumors while maintaining a marrow dose of <2 Gy. However, with blood-based marrow dosimetry, this ratio extended between 2.29 and 5.80 (4.11 ± 0.97), extending the range of deliverable dose to between 4.62 and 8.04 Gy. An overview of the tumor dosimetry and associated tumor-to-marrow analysis is shown in Table 15 for all lesions targeted within canine patients in this study.

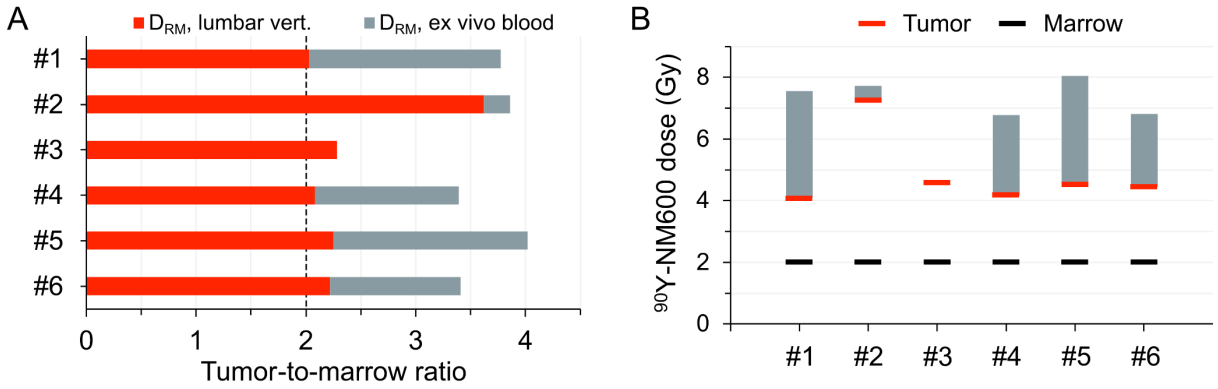

Figure 54: (A) Tumor-to-marrow ratio (D_{tumor}/D_{RM}), where D_{tumor} represents the minimum dose delivered to a given set of tumors within a canine patient. Marrow dose is determined either via ex vivo blood-based dosimetry or in vivo dosimetry estimates from the lumbar vertebrae. For all but canine patient #3, blood-based dosimetry estimates were less than that determined in the lumbar vertebrae. (B) The maximum achievable D_{min} capable of being delivered to all tumors in a canine patient while limiting marrow dose to ≤ 2 Gy. The grey bar represents the extended range of D_{min} using blood based marrow dosimetry estimates.

Table 15: Summary of tumor dosimetry results in canine patients. Tumor-to-marrow ratio calculated based on conservative lumbar marrow dosimetry estimates.

ID	Tumor volume	^{90}Y-NM600 Rx Dose (Gy/GBq)	^{90}Y-NM600 norm. Rx Dose (Gy/(GBq/kg))	Tumor-to-marrow ratio
#1	lung met, large	3.27	143.7	3.08
	lung met, small	2.93	128.8	2.76
	humerus head, R	2.15	94.7	2.03
	thigh (index), R	3.11	137.0	2.94
	tricep, L	2.63	115.7	2.48
#2	tonsil (index)	8.24	145.0	4.38
	mand LN, L	6.90	125.5	3.66
	lung met	6.82	124.1	3.62
#3	primary	9.14	76.7	2.31
	mand LN, L a	9.57	80.4	2.42
	mand LN, L b	9.83	82.5	2.48
#4	primary	2.49	104.6	2.23
	mand LN, L	2.55	107.0	2.28
	mand LN, R	2.33	97.8	2.08
#5	flank	4.52	85.9	2.25
	abdominal	5.19	98.6	2.58
	lung met, large	5.53	105.1	2.75
	mediastinal LN	6.52	123.8	3.24
#6	primary	4.39	144.8	3.07
	mand LN, L	3.91	129.1	2.74
	lung met, 2	3.18	104.8	2.22
	lung met, 3	3.76	124.1	2.63
	lung met, 6	3.59	118.3	2.51
			113.2 ± 21.3	2.73 ± 0.57

Following delivery of the tri-modal treatment combination of EBRT + ^{90}Y-NM600 RPT + IT-IC, canine patients exhibited no dose-limiting toxicities in the 2 Gy cohort (patients 1-5). No follow up analysis was available for canine patient 6 as of the time when this thesis was completed. All adverse events observed in canine patients were low grade and transient in nature. While bone marrow toxicity was anticipated as the dose-limiting factor in this study, only one case of grade 1 neutropenia and two grade 1 lymphopenias were observed. Based on conservative marrow dosimetry estimates, canine patients in this cohort received between 0.59 and 1.01 Gy to the bone marrow. Notably, grade 1 and 2 hepatic enzyme (ALKP and ALT) elevations were observed in all canine patients, potentially resulting from the hepatobiliary excretion of ^{86}Y/^{90}Y-NM600.

5.3 Discussion

The theranostic ^{86}Y/^{90}Y-NM600 prospective dosimetry workflow developed in this work was successfully implemented in six canine patients to facilitate the judicious delivery of low-dose ^{90}Y-NM600 RPT as part of the tri-modal treatment combination with EBRT and IT-IC. Phantom studies of the quantitative imaging of ^{86}Y identified issues systemic to the TOF reconstruction in the setting of high SFF and prompt gamma contamination. Additionally, the application of PVC in dosimetry of lung metastases proved critical in a treatment planning setting where the prescription of ^{90}Y-NM600 RPT was determined based on the lesion receiving the least amount of dose. The implementation of LRR+DIR in the temporal coregistration of targeted tumor and normal tissue volumes drastically improved the accuracy and repeatability of dosimetry estimates in canine patients.

The extent to which commercial TOF reconstruction using VPFX with the GE Discovery MI PET-CT scanner distorted and amplified the perceived activity distribution of ^{86}Y was unexpected and highlights the importance of establishing robust imaging protocols for atypical PET, and SPECT, tracers increasingly used in theranostic investigations. Utilizing TOF in the reconstruction of PET images can substantially improve localization of positron annihilation events, but requires the utilization of alternative scatter correction algorithms (*253*). Corrections accounting for normalization, deadtime, and attenuation are apportioned to spatially distributed TOF timing bins using multiplicative factors whereas corrections for scatter and random events is performed on an additive basis (*254*). In the context of quantitative imaging of ^{86}Y with significant prompt gamma contamination at energies at and above the conventional 511 keV energy window, the overabundance of multiples and out-of-field contributions push TOF scatter correction

algorithms beyond their capabilities (*255*,*256*). The average SFF of 74.3% ± 3.7% observed in ^{86}Y PET imaging is nearly double that of typical ^{18}F imaging studies (43.3% (*257*)). Investigations into ^{86}Y PET imaging with a GE Discovery 690 VCT PET-CT system by PEN Braad et al (*258*) arrived at similar conclusions wherein TOF reconstruction produced large errors in quantification and uniformity. Their group arrived at a quantification error of 25-50% in cylindrical phantom studies (NEMA NU-2 1994 phantom without inserts) with the distortion being greatest at the center of images produced with TOF reconstruction. The foremost impact that TOF reconstruction appears to have on theranostic ^{86}Y/^{90}Y-NM600 dosimetry estimates is degradation of the tumor-to-marrow ratio leading to lower rates of treatment eligibility and general overestimation of activity in canine patients resulting in overly optimistic dosimetry estimates that lead to under-prescription of ^{90}Y-NM600.

The biodistribution of ^{86}Y-NM600 in canine patients demonstrated hepatobiliary excretion of the agent in a capacity similar to that observed in mouse models. The variability between patients in the accumulation of ^{86}Y-NM600 in the gallbladder as part of this excretion pathway presents an interesting avenue for further investigations. In the case of patient 1, who presented with significant gallbladder uptake, a high fat diet had been established prior to and during the imaging study. The impact of a high fat diet or other environmental factors on the pharmacokinetics of NM600 has not been thoroughly investigated but could potentially alter the biodistribution of ^{90}Y-NM600 to an extent that may prove dosimetrically impactful.

One limitation in the analysis of blood activity and the calculation of [A_{bld}] is the use of a mono-exponential fit of a profile seemingly presenting bi-phasic behavior. This resulted in poor fitting of the data points across all measurement methods. Specifically, the blood half-life estimated in this work likely underestimates the prolonged late-phase clearance of the ^{86}Y-NM600.

In the case of blood-draw measurements of activity concentration, the occasional presence of a fourth datapoint past that of the final imaging timepoint allowed for more accurate fitting of the blood-activity profile. However, this was not always the case in all canine patient studies and the use of more advanced bi-exponential modeling of the time-activity curve would lead to overfitting of the data, rendering the derived decay rates of little use. For more accurate quantification of the blood-activity half-life of ^{86}Y-NM600 in canine patients, and thus more accurate blood-based dosimetry estimates, more frequent blood sampling should be performed to allow for more advanced pharmacokinetic modeling to be implemented.

Another key limitation of this work lies in the accounting of lung metastases and small lesions with no apparent uptake due to size and breathing motion based partial volume effects. Given that the premise of the ^{90}Y-NM600 RPT delivery was targeting a specific minimum dose in all sites of disease, smaller lesions with a characteristically low self-absorbed fraction due to the long pathlength of ^{90}Y betas are likely to receive the lowest dose. Compounding this is the difficulty in attaining high confidence in the accuracy of PET-CT imaging of these lesions where significant partial volume effects result in lower amounts of apparent activity to begin with. Partial volume corrections like those implemented in this work can account for these effects to an extent, but the confidence in dosimetry estimates wanes as larger correction factors arrive at results multiple times that of the initial uncorrected estimate. The smallest lesion for which uptake was clearly apparent and dosimetric analysis performed was 0.49 ml, with an RC factor of 0.412. However, preclinical biodistribution and dosimetry studies performed in mice bearing tumors varying between 50 and 200 mm^3 in volume indicated that smaller lesions presented with higher concentrations of ^{86}Y-NM600 (unpublished work with Peter Carlson, MD PhD). Notably, observations of necrosis and heterogeneous uptake in larger tumors both in mice and canine

patients indicates that bigger is not always better when it comes to uptake of ^{86}Y-NM600 in tumors. Still, further investigation is needed to support assumptions of ^{86}Y-NM600 uptake in lesions too small for quantification with clinical PET-CT evaluation (e.g. micro-metastases).

A tumor-to-marrow ratio of dose was >2.0 in all canine patient tumors for which theranostic dosimetry was performed. Using blood-based marrow dosimetry estimates, this ratio is even higher at >2.2 across all tumors. Combined with the lack of bone marrow toxicity or lymphopenia observed in canine patients receiving ^{90}Y-NM600, the opportunity to escalate the minimum dose delivered to canine patients is promising. Assuming a maximum tolerable dose to marrow of 2 Gy in this tri-modal treatment combination, a minimum dose of at least 4 Gy to all tumors should be achievable in a majority of patients.

5.4 Acknowledgements

The companion canine trial from which much of the data analyzed in this work is derived was the culmination of several years of collaboration between a research groups in medical physics, radiology, human oncology, veterinary oncology, and others. Eduardo Aluicio-Sarduy and committee member Jonathan Engle of the Cyclotron Gang provided ^{86}Y for labeling with NM600 and use in phantom studies. Reinier Hernandez and committee member Jamey Weichert provided radiolabeled ^{86}Y-NM600 and ^{90}Y-NM600 for use in canine patients. Tyler Bradshaw and Reiner Hernandez assisted in phantom preparation. David Vail, Michelle Turek, Kara Magee, Rubi Hayim, and others provided veterinary care and assistance in PET-CT imaging for canine patients. Committee member Zach Morris provided guidance towards delivery of low-dose ^{90}Y-NM600 RPT in combination with EBRT and IT-IC. Morris and Sondel lab alumni, Ravi Patel and Peter Carlson helped establish in preclinical investigations the framework for the trimodal combination of EBRT, low dose ^{90}Y-NM600 RPT, and immunotherapy. Joe Grudzinski assisted in the review of theranostic dosimetry estimates and contouring of normal tissues. Finally, committee member and advisor Bryan Bednarz provided guidance, funding, and discussion towards the completion of this work. Portions of the methodology and results pertaining to the canine trial in this work have been adapted from recent co-authored publications (*12*,*239*).

Chapter 6

Conclusion and Future Works

The work presented in this thesis explores the development and translation of theranostic $^{86}Y/^{90}Y$-NM600 dosimetry from a preclinical tool into a critical component of the clinical implementation of low dose ^{90}Y-NM600 RPT. In the preclinical setting, the translation of theranostic dosimetry tools accompanied that of $^{86}Y/^{90}Y$-NM600. Early work in this thesis characterized the pharmacokinetics and biodistribution of ^{86}Y-NM600 in a variety of tumor models, including B78 melanoma. The challenges associated with quantitative ^{86}Y PET imaging of tumors were further explored in phantom studies where the recovery of PET-imaged ^{86}Y activity in small lesions was characterized in the preclinical and clinical scanners used in this work. On the clinical side, a voxel-level partial volume correction approach was developed based on Lucy-Richardson iterative deconvolution using an ^{86}Y-specific point spread function measured in the scanner. The algorithm is spatially invariant but utilizes a PSF specific to the location of targeted lesion of interest. For small lesions (0.5 ml), the VPHD-LR approach improved recovery of PET-imaged ^{86}Y by up to

17.8% and theranostic mean dose estimates for ^{90}Y of up to 14.2%. In the setting of heterogeneous activity, more marginal improvements of 1.8% and 1.5% in mean activity and dose were observed. In addition to voxel-level approaches, a novel RC-based PVC methodology for correcting dose-rate distributions was developed to achieve more accurate mean dose estimates for spherical lesions in a uniform background. With this VPHD-LR+PVC approach, the accuracy of mean dose estimates in 2 ml lesions, for example, improved from -38.6% to +0.9%.

In addition to partial volume correction, the development of an automated locoregional registration approach proved essential for achieving accurate voxel-level dosimetry estimates. The addition of deformable image registration between rigidly registered CT scans at reference and moving timepoints was particularly useful in accurately aligning target volumes across the imaging series. The capability of this framework was validated in a deformable anthropomorphic phantom and the impact of the registration approaches on target volume definition thoroughly explored. Detailed analysis comparing cumulative dose distributions in a representative target volume showed minimal dose differences between target volume definitions following application of the LRR+DIR approach. Notably, the intersection of target volumes generated the most robust DVH profiles across registration approaches in both phantom and canine patient studies.

Finally, the developed ^{86}Y/^{90}Y-NM600 theranostic dosimetry framework was successfully implemented in an ongoing companion canine trial. The time required for theranostic dosimetry to be performed was approximately 7.5 days, well within the initially given timeframe of two weeks. Following prescription of low-dose ^{90}Y-NM600 RPT in the first dose escalation cohort, >2 Gy to all targeted lesions, canine patients exhibited little to no hematological toxicity and systemic lymphopenia was avoided in all cases. Retrospective analysis provided by theranostic dosimetry will also help support further dose escalation of ^{90}Y-NM600 in the trial. Additionally, phantom

studies performed as part of this work revealed systemic issues with TOF PET imaging of ^{86}Y and helped in establishing ideal imaging protocols.

The work presented in this thesis towards developing a translatable theranostic dosimetry approach has also had an impact on radiopharmaceutical dosimetry in related investigations. The updated RAPID workflow developed as part of this thesis is also currently in use in a clinical trial using ^{131}I-NM404 RPT to boost and replace dose from EBRT in patients with recurrent head and neck cancer. On the preclinical side, overhaul of the RAPID platform has helped facilitate more widespread application of the platform by scientists and other members of the advanced imaging and dosimetry core at UW-Madison. The modular format of the RAPID research platform additionally allows for future medical physics researchers to further develop key segments of the workflow and add functionality as desired. In parallel, but unaffiliated with the work presented in this thesis, commercial efforts have been expended to develop a more clinically applicable software package to better facilitate clinical translation of theranostic dosimetry at this institution and elsewhere.

6.1 Recommendations for future work

6.1.1 Compensating for intra-scan motion

A great deal of effort was undertaken in this thesis to account for patient positioning irregularities between PET/CT scans to achieve more accurate dose-rate accumulation in theranostic dosimetry. However, a key underlying assumption in this process is the accurate coregistration of the PET and CT image volumes acquired at each timepoint. While CT scans were acquired in a matter of seconds, a whole-body PET scan of ^{86}Y-NM600 at later timepoints in this study required an hour or more for large canine patients. Canine patients were under general anesthesia while undergoing imaging in this study, but regular functional bodily motion (e.g. breathing, peristalsis) introduced uncertainty in the alignment of PET and CT images. In the case of breathing motion, the use of gated PET-CT imaging could help improve conspicuity of small metastatic lesions in the lungs. Elsewhere, involuntary motions in the abdominal cavity, as occasionally observed in canine patients of this study, can lead to significant displacement in critical organs such as the kidneys. This type of misregistration is currently undetectable without manual review of PET-CT overlap in target volumes. Future research efforts could be directed towards developing an automated method of detecting atypical PET distributions or temporal uptake profiles in otherwise predicably behaving normal tissues.

6.1.2 Automated contouring

One of the greatest expenditures of time and energy in the clinical and preclinical implementation of multi-timepoint internal dosimetry in this work was in generating contours at each timepoint. Early efforts towards adapting the locoregional registration framework developed

here towards that of contour propagation of a single set of contours at one timepoint showed limited success. Further development of this approach to make contouring at each timepoint unnecessary would drastically improve the translational capacity of this theranostic dosimetry workflow. Results presented in this thesis already provides a preliminary justification for utilizing a single contour from a reference timepoint in multi-timepoint dosimetry with reasonable success. Additionally, recent advances in machine learning based approaches for auto contouring of normal tissues in conventional diagnostic imaging studies should also benefit the adoption of multi-timepoint dosimetry. One interesting avenue to pursue along this line is the incorporation of temporal uptake profiles from PET-CT imaging series in machine learning models to automatically identify anomalous regions uptake for further analysis.

6.1.3 Single timepoint dosimetry

An additional barrier to the implementation of theranostic dosimetry, and multi-timepoint internal dosimetry in particular is the cost of multiple imaging timepoints and lack of available resources in nuclear medicine to support widespread adoption. As such, the development of single-timepoint and reduced-timepoint dosimetry approaches is an active area of research in the field and should be investigated further for ^{86}Y/^{90}Y-NM600. Initial steps to take towards this will need to be in the detailed pharmacokinetic modeling of ^{86}Y/^{90}Y-NM600 in tumors and normal tissues. The baseline kinetic parameters derived from this work will be key to the accuracy of the assumed time-activity-curves required for single-timepoint dosimetry. Recent work by Jackson PA et al (*134*) demonstrates a natural limitation of single timepoint dosimetry in highlighting the benefits of late timepoint imaging for tumors and early timepoint imaging for normal tissues. The inter- and intra-patient variability in tumor uptake kinetics, as observed with canine patients in this work, further adds to the uncertainties adopted in transitioning to single-timepoint approaches. The extent

to which this impacts ^{86}Y/^{90}Y-NM600 can be further investigated with comprehensive retrospective analysis of the wealth of preclinical imaging data accumulated across numerous dosimetry studies. This should help establish baseline kinetics for modeling of single timepoint dosimetry and allow for analysis of the extent to which accuracy is be impacted by reduced timepoint dosimetry.

6.1.4 Characterizing immunological response following ^{90}Y-NM600 RPT

Considerable efforts have been made in this thesis to ensure the safe and effective delivery of low-dose ^{90}Y-NM600 RPT to canine patients in the associated dose escalation trial. Monitoring for hematological and lymphocytic toxicities while dose escalation continues should help elucidate dose-limiting factors for ^{90}Y-NM600 RPT in the trimodal treatment combination investigated herein. While ex vivo sampling for immunogenic markers in canine patients provides one avenue through which to quantify immunomodulatory dose response to RPT, further in vivo methods should be considered. A number of PET tracers to monitor immune activation and behavior of regulatory T cells, for example, are emerging and would be interesting to assess in conjunction with in situ vaccination approaches utilizing RPT. Given the difficulty in establishing robust fundamental radiobiological parameters to better characterize the impact of RPT, end to end analysis of immune activation could prove more impactful for translational research. The presence of ^{90}Y/^{177}Lu-NM600 should not interfere significantly with the PET imaging of immune cell dynamics with a secondary tracer.

6.1.5 Dose discrepancies in low density media

As discussed within the context of lung metastases dosimetry, there are non-negligible density-derived effects on Monte Carlo based dosimetry estimates. In some cases, the presence of

apparent activity in air cavities results in abnormally high doses. In the case of lung tissue, the low density of the media results in large doses not observed in normal tissue closer in HU-density to that of water. Further analysis and benchmarking of the Monte Carlo code should be performed, but the differences between dose-to-medium and dose-to-water in the context of radiopharmaceutical dosimetry should be further investigated. This could entail the experimental benchmarking of direct measurements of dose from ^{90}Y using film or thermo-luminescent dosimeters (TLDs) against that of RAPID Monte Carlo dosimetry estimates based on imaging of the experimental setup. One such set up could have film layered between blocks of known density media and exposed to a line source of ^{90}Y contained within a capillary tube for a precise amount of time. 2D dose profiles from film measurements could then be compared to RAPID dosimetry estimates in the varying-density media for confirmation.

Fundamentally, Monte Carlo produces estimates of dose in terms of dose-to-medium. Comparatively, radiation oncology has largely adopted the standard of dose-to-water for dosimetry purposes and the vast majority of established dose limits for OARs are in terms of dose-to-water. The Monte Carlo framework underlying RAPID should be adapted to accommodate for the translation of dose-to-medium into dose-to-water. This would better facilitate combination therapy with conventional radiotherapy approaches like external beam or brachytherapy and would eliminate the need to perform additional simulations in water density-based geometries for lung met dosimetry. However, there is also a concerted effort in radiation oncology to encourage the reporting of dose-to-medium for analysis in clinical trials involving EBRT (*259*,*260*).

Bibliography

1. Galon J, Bruni D. Approaches to treat immune hot, altered and cold tumours with combination immunotherapies. *Nat Rev Drug Discov 2018 183*. 2019;18:197-218.
2. Spiotto M, Fu Y-X, Weichselbaum RR. The intersection of radiotherapy and immunotherapy: mechanisms and clinical implications. *Sci Immunol*. 2016;1.
3. Wennerberg E, Vanpouille-Box C, Bornstein S, Yamazaki T, Demaria S, Galluzzi L. Immune recognition of irradiated cancer cells. *Immunol Rev*. 2017;280:220-230.
4. Kang J, Demaria S, Formenti S. Current clinical trials testing the combination of immunotherapy with radiotherapy. *J Immunother Cancer*. 2016;4:51.
5. Marabelle A, Tselikas L, de Baere T, Houot R. Intratumoral immunotherapy: using the tumor as the remedy. *Ann Oncol Off J Eur Soc Med Oncol*. 2017;28:xii33-xii43.
6. Brody JD, Ai WZ, Czerwinski DK, et al. In situ vaccination with a TLR9 agonist induces systemic lymphoma regression: A phase I/II study. *J Clin Oncol*. 2010;28:4324-4332.
7. Morris ZS, Guy EI, Francis DM, et al. In Situ Tumor Vaccination by Combining Local Radiation and Tumor-Specific Antibody or Immunocytokine Treatments. *Cancer Res*. 2016;76:3929-3941.
8. Weide B, Derhovanessian E, Pflugfelder A, et al. High response rate after intratumoral treatment with interleukin-2. *Cancer*. 2010;116:4139-4146.
9. Morris ZS, Guy EI, Werner LR, et al. Tumor-Specific Inhibition of In Situ Vaccination by Distant Untreated Tumor Sites. *Cancer Immunol Res*. 2018;6:825-834.
10. Theelen WSME, Peulen HMU, Lalezari F, et al. Effect of Pembrolizumab After Stereotactic Body Radiotherapy vs Pembrolizumab Alone on Tumor Response in Patients With Advanced Non–Small Cell Lung Cancer: Results of the PEMBRO-RT Phase 2 Randomized Clinical Trial. *JAMA Oncol*. 2019;5:1276.
11. Lin AJ, Gang M, Rao YJ, et al. Association of Posttreatment Lymphopenia and Elevated Neutrophil-to-Lymphocyte Ratio With Poor Clinical Outcomes in Patients With Human Papillomavirus–Negative Oropharyngeal Cancers. *JAMA Otolaryngol Head Neck Surg*. 2019;145:413.
12. Patel RB, Hernandez R, Carlson P, et al. Low-dose targeted radionuclide therapy renders immunologically cold tumors responsive to immune checkpoint blockade. *Sci Transl Med*. 2021;13:3631.
13. Divgi C. The Current State of Radiopharmaceutical Therapy. *J Nucl Med*. 2018;59:1706-1707.
14. Czernin J. Molecular Imaging and Therapy with a Purpose: A Renaissance of Nuclear Medicine. *J Nucl Med*. 2017;58:21A-22A.
15. Dolgin E. Radioactive drugs emerge from the shadows to storm the market. *Nat Biotechnol*. 2018;36:1125-1127.

16. Weichert JP, Clark PA, Kandela IK, et al. Alkylphosphocholine analogs for broad-spectrum cancer imaging and therapy. *Sci Transl Med*. 2014;6:240ra75-240ra75.

17. Grudzinski JJ, Hernandez R, Marsh I, et al. Preclinical characterization of 86/90Y-Nm600 in a variety of murine and human cancer tumor models. *J Nucl Med*. 2019;60:1622-1628.

18. Clark PA, Sriramaneni RN, Bates AM, et al. Low-Dose Radiation Potentiates the Propagation of Anti-Tumor Immunity against Melanoma Tumor in the Brain after In Situ Vaccination at a Tumor outside the Brain. *Radiat Res*. April 2021.

19. Hernandez R, Walker KL, Grudzinski JJ, et al. 90Y-NM600 targeted radionuclide therapy induces immunologic memory in syngeneic models of T-cell Non-Hodgkin's Lymphoma. *Commun Biol*. 2019;2:79.

20. Li T, Ao ECI, Lambert B, Brans B, Vandenberghe S, Mok GSP. Quantitative Imaging for Targeted Radionuclide Therapy Dosimetry - Technical Review. *Theranostics*. 2017;7:4551-4565.

21. Besemer AE, Yang YM, Grudzinski JJ, Hall LT, Bednarz BP. Development and Validation of RAPID: A Patient-Specific Monte Carlo Three-Dimensional Internal Dosimetry Platform. *Cancer Biother Radiopharm*. 2018;33:155-165.

22. Bednarz B, Grudzinski J, Marsh I, et al. Murine-specific internal dosimetry for preclinical investigations of imaging and therapeutic agents. *Heal Phys*. 2018;114:450-459.

23. Grudzinski J, Marsh I, Titz B, et al. CLR 125 Auger Electrons for the Targeted Radiotherapy of Triple-Negative Breast Cancer. *Cancer Biother Radiopharm*. 2018;33:87-95.

24. Baiu DC, Marsh IR, Boruch AE, et al. Targeted molecular radiotherapy of pediatric solid tumors using a radioiodinated alkyl-phospholipid ether analog. *J Nucl Med*. 2018;59:244-250.

25. Marsh IR, Grudzinski J, Baiu DC, et al. Preclinical Pharmacokinetics and Dosimetry Studies of 124I/131I-CLR1404 for Treatment of Pediatric Solid Tumors in Murine Xenograft Models. *J Nucl Med*. 2019;60:1414-1420.

26. Dillekås H, Rogers MS, Straume O. Are 90% of deaths from cancer caused by metastases? *Cancer Med*. 2019;8:5574.

27. Hanahan D, Weinberg RA. The Hallmarks of Cancer. *Cell*. 2000;100:57-70.

28. Neal JW, Sledge GW. Successes, toxicities and challenges in solid tumours. *Nat Rev Clin Oncol 2014 1111*. 2014;11:627-628.

29. Jamal-Hanjani M, Quezada SA, Larkin J, Swanton C. Translational implications of tumor heterogeneity. *Clin Cancer Res*. 2015;21:1258-1266.

30. Holohan C, Van Schaeybroeck S, Longley DB, Johnston PG. Cancer drug resistance: an evolving paradigm. *Nat Rev Cancer*. 2013;13:714-726.

31. Lopez JS, Banerji U. Combine and conquer: challenges for targeted therapy combinations in early phase trials. *Nat Rev Clin Oncol*. 2017;14:57.

32. Delaney G, Jacob S, Featherstone C, Barton M. The role of radiotherapy in cancer treatment: estimating optimal utilization from a review of evidence-based clinical

guidelines. *Cancer*. 2005;104:1129-1137.

33. Chen P, Mrkobrada M, Vallis KA, et al. Comparative antiproliferative effects of 111In-DTPA-hEGF, chemotherapeutic agents and γ-radiation on EGFR-positive breast cancer cells. *Nucl Med Biol*. 2002;29:693-699.

34. Sgouros G, Bodei L, McDevitt MR, Nedrow JR. Radiopharmaceutical therapy in cancer: clinical advances and challenges. *Nat Rev Drug Discov*. 2020;19:589-608.

35. Hall E, Giaccia A. Radiobiology for the Radiologist. 6th editio. Philadelphia: Lippincott Williams & Wilkins; 2006.

36. Gill MR, Falzone N, Du Y, Vallis KA. Targeted radionuclide therapy in combined-modality regimens. *Lancet Oncol*. 2017;18:e414-e423.

37. Sgouros G, Bodei L, McDevitt MR, Nedrow JR. Radiopharmaceutical therapy in cancer: clinical advances and challenges. *Nat Rev Drug Discov 2020 199*. 2020;19:589-608.

38. Marcu L, Bezak E, Allen BJ. Global comparison of targeted alpha vs targeted beta therapy for cancer: In vitro, in vivo and clinical trials. *Crit Rev Oncol Hematol*. 2018;123:7-20.

39. Pouget J-P, Lozza C, Deshayes E, Boudousq V, Navarro-Teulon I. Introduction to Radiobiology of Targeted Radionuclide Therapy. *Front Med*. 2015;2:12.

40. Haberkorn U, Giesel F, Morgenstern A, Kratochwil C. The Future of Radioligand Therapy: α, β, or Both? *J Nucl Med*. 2017;58:1017-1018.

41. Malcolm J, Falzone N, Lee BQ, Vallis KA. Targeted Radionuclide Therapy: New Advances for Improvement of Patient Management and Response. *Cancers (Basel)*. 2019;11.

42. O'Neill E, Kersemans V, Allen PD, et al. Imaging DNA Damage Repair in vivo Following 177 Lu-DOTATATE Therapy . *J Nucl Med*. 2019:jnumed.119.232934.

43. De Jong M, Wout ;, Breeman AP, Valkema R, Bernard BF, Krenning EP. Combination Radionuclide Therapy Using 177 Lu-and 90 Y-Labeled Somatostatin Analogs. *J Nucl Med*. 2005;46:13-17.

44. Mothersill C, Seymour CB. Radiation-induced bystander effects — implications for cancer. *Nat Rev Cancer 2004 42*. 2004;4:158-164.

45. Boyd M, Ross SC, Dorrens J, et al. Radiation-induced biologic bystander effect elicited in vitro by targeted radiopharmaceuticals labeled with alpha-, beta-, and auger electron-emitting radionuclides. *J Nucl Med*. 2006;47:1007-15.

46. Lugade AA, Sorensen EW, Gerber SA, Moran JP, Frelinger JG, Lord EM. Radiation-Induced IFN-γ Production within the Tumor Microenvironment Influences Antitumor Immunity. *J Immunol*. 2008;180:3132-3139.

47. Seidlin SM, Marinelli LD, Oshry E. Radioactive iodine therapy. Effect on functioning metastases of adenocarcinoma of the thyroid. *J Am Med Assoc*. 1946;132:838-847.

48. Mumtaz M, Lin LS, Hui KC, Mohd Khir AS. Radioiodine I-131 for the therapy of graves' disease. *Malays J Med Sci*. 2009;16:25-33.

49. Das S, Al-Toubah T, El-Haddad G, Strosberg J. 177 Lu-DOTATATE for the treatment of

gastroenteropancreatic neuroendocrine tumors. *Expert Rev Gastroenterol Hepatol*. 2019;13:1023-1031.

50. Kratochwil C, Giesel FL, Stefanova M, et al. PSMA-Targeted Radionuclide Therapy of Metastatic Castration-Resistant Prostate Cancer with 177Lu-Labeled PSMA-617. *J Nucl Med*. 2016;57:1170-1176.

51. Elgqvist J, Frost S, Pouget JP, Albertsson P. The Potential and Hurdles of Targeted Alpha Therapy – Clinical Trials and Beyond. *Front Oncol*. 2013;3.

52. Lau WY, Ho S, Leung TWT, et al. Selective internal radiation therapy for nonresectable hepatocellular carcinoma with intraarterial infusion of 90yttrium microspheres. *Int J Radiat Oncol*. 1998;40:583-592.

53. Maleux G, Deroose C, Laenen A, et al. Yttrium-90 radioembolization for the treatment of chemorefractory colorectal liver metastases: Technical results, clinical outcome and factors potentially influencing survival. *http://dx.doi.org/103109/0284186X20151101151*. 2015;55:486-495.

54. Salem R, Thurston KG. Radioembolization with 90Yttrium Microspheres: A State-of-the-Art Brachytherapy Treatment for Primary and Secondary Liver Malignancies: Part 1: Technical and Methodologic Considerations. *J Vasc Interv Radiol*. 2006;17:1251-1278.

55. Müller C, Van Der Meulen NP, Benešová M, Schibli R. Therapeutic radiometals beyond 177Lu and 90Y: Production and application of promising α-particle, β--particle, and auger electron emitters. *J Nucl Med*. 2017;58:91S-96S.

56. Randhawa P, Olson AP, Chen S, et al. Meitner-Auger Electron Emitters for Targeted Radionuclide Therapy: Mercury-197m/g and Antimony-119. *Curr Radiopharm*. 2021;14.

57. Aluicio-Sarduy E, Thiele NA, Martin KE, et al. Establishing Radiolanthanum Chemistry for Targeted Nuclear Medicine Applications. *Chemistry*. 2020;26:1238.

58. Parker C, Lewington V, Shore N, et al. Targeted Alpha Therapy, an Emerging Class of Cancer Agents: A Review. *JAMA Oncol*. 2018;4:1765-1772.

59. Warner S. Diagnostics + Therapy = Theranostics. *Scientist*. 2004;18:38-39.

60. Ciardiello F, Arnold D, Casali PG, et al. Delivering precision medicine in oncology today and in future—the promise and challenges of personalised cancer medicine: a position paper by the European Society for Medical Oncology (ESMO). *Ann Oncol*. 2014;25:1673-1678.

61. Luster M, Clarke SE, Dietlein M, et al. Guidelines for radioiodine therapy of differentiated thyroid cancer.

62. Maffey-Steffan J, Scarpa L, Svirydenka A, et al. The 68Ga/177Lu-theragnostic concept in PSMA-targeting of metastatic castration–resistant prostate cancer: impact of post-therapeutic whole-body scintigraphy in the follow-up. *Eur J Nucl Med Mol Imaging*. 2020;47:695.

63. Rösch F, Herzog H, Qaim S. The Beginning and Development of the Theranostic Approach in Nuclear Medicine, as Exemplified by the Radionuclide Pair 86Y and 90Y. *Pharmaceuticals*. 2017;10:56.

64. Walrand S, Flux GD, Konijnenberg MW, et al. Dosimetry of yttrium-labelled radiopharmaceuticals for internal therapy: 86Y or 90Y imaging? *Eur J Nucl Med Mol Imaging*. 2011;38:57-68.

65. Conti M, Eriksson L. Physics of pure and non-pure positron emitters for PET: A review and a discussion. *EJNMMI Phys*. 2016;3:8.

66. Bokhari TH, Butt MB, Hina S, Iqbal M, Daud M, Imran M. A review on 90Y-labeled compounds and biomolecules. *J Radioanal Nucl Chem*. 2017;314:1487-1496.

67. Chakravarty R, Pandey U, Manolkar RB, Dash A, Venkatesh M, Pillai MRA. Development of an electrochemical 90Sr–90Y generator for separation of 90Y suitable for targeted therapy. *Nucl Med Biol*. 2008;35:245-253.

68. Necsoiu D, Morgan IL, Hupf H, et al. Production of 90Y by the 90Zr(n,p)90Y reaction using neutrons produced from a variable energy cyclotron. *AIP Conf Proc*. 2001;576:335.

69. Krane KS. The 89Y(n,γ) reaction: Radiative cross sections and the decay of 90Ym. *Appl Radiat Isot*. 2020;163:109191.

70. Yue J, Mauxion T, Reyes DK, et al. Comparison of quantitative Y-90 SPECT and non-time-of-flight PET imaging in post-therapy radioembolization of liver cancer. *Med Phys*. 2016;43:5779-5790.

71. Selwyn RG, Nickles RJ, Thomadsen BR, DeWerd LA, Micka JA. A new internal pair production branching ratio of 90Y: The development of a non-destructive assay for 90Y and 90Sr. *Appl Radiat Isot*. 2007;65:318-327.

72. Le Fur M, Caravan P. 86Y PET imaging. In: Methods in Enzymology. Academic Press Inc.; 2021.

73. Aluicio-Sarduy E, Hernandez R, Valdovinos HF, et al. Simplified and automatable radiochemical separation strategy for the production of radiopharmaceutical quality 86Y using single column extraction chromatography. *Appl Radiat Isot*. 2018;142:28-31.

74. Perk LR, Gerard ;, Visser WM, et al. Zr as a PET Surrogate Radioisotope for Scouting Biodistribution of the Therapeutic Radiometals 90 Y and 177 Lu in Tumor-Bearing Nude Mice After Coupling to the Internalizing Antibody Cetuximab.

75. Snyder F, Wood R. Alkyl and Alk-l-enyl Ethers of Glycerol in Lipids from Normal and Neoplastic Human Tissues. *Cancer Res*. 1969;29:251-257.

76. Meyer KL, Schwendner SW, Counsell RE. Potential tumor or organ-imaging agents. 30. Radioiodinated phospholipid ethers. *J Med Chem*. 1989;32:2142-2147.

77. Counsell RE, Schwendner SW, Meyer KL, Haradahira T, Gross MD. Tumor visualization with a radioiodinated phospholipid ether. *J Nucl Med*. 1990;31:332-336.

78. Pinchuk AN, Rampy MA, Longino MA, et al. Synthesis and structure-activity relationship effects on the tumor avidity of radioiodinated phospholipid ether analogues. *J Med Chem*. 2006;49:2155-2165.

79. Weichert JP, Clark PA, Kandela IK, et al. Alkylphosphocholine analogs for broad-spectrum cancer imaging and therapy. *Sci Transl Med*. 2014;6:240ra75-240ra75.

80. Carrasco MP, Jiménez-López JM, Ríos-Marco P, Segovia JL, Marco C. Disruption of

cellular cholesterol transport and homeostasis as a novel mechanism of action of membrane-targeted alkylphospholipid analogues. *Br J Pharmacol*. 2010;160:355-366.

81. Marino R, Baiu DC, Bhattacharya S, et al. Tumor-selective anti-cancer effects of the synthetic alkyl phosphocholine analog CLR1404 in neuroblastoma. *Am J Cancer Res*. 2015;5:3422-3435.

82. Morris ZS, Weichert JP, Saker J, et al. Therapeutic combination of radiolabeled CLR1404 with external beam radiation in head and neck cancer model systems. In: Radiotherapy and Oncology. Vol 116. Elsevier Ireland Ltd; 2015:504-509.

83. Grudzinski JJ, Titz B, Kozak K, et al. A phase 1 study of 131I-CLR1404 in patients with relapsed or refractory advanced solid tumors: Dosimetry, biodistribution, pharmacokinetics, and safety. Doherty TM, ed. *PLoS One*. 2014;9:e111652.

84. Jagodinsky JC, Jin WJ, Bates AM, et al. Temporal analysis of type 1 interferon activation in tumor cells following external beam radiotherapy or targeted radionuclide therapy. *Theranostics*. 2021;11:6120.

85. Eberlein U, Cremonesi M, Lassmann M. Individualized Dosimetry for Theranostics: Necessary, Nice to Have, or Counterproductive? *J Nucl Med*. 2017;58:97S-103S.

86. DeVita Junior VT, Hellman S, Rosenberg SA. Cancer: principles & practice of oncology. In: Cancer: Principles & Practice of Oncology. ; 2001:lxxii-3.

87. Stabin MG, Sparks RB, Crowe E. OLINDA/EXM: the second-generation personal computer software for internal dose assessment in nuclear medicine. *J Nucl Med*. 2005;46:1023-7.

88. Strigari L, Konijnenberg M, Chiesa C, et al. The evidence base for the use of internal dosimetry in the clinical practice of molecular radiotherapy. *Eur J Nucl Med Mol Imaging*. 2014;41:1976-1988.

89. Bolch WE, Eckerman KF, Sgouros G, et al. MIRD Pamphlet No. 21: A Generalized Schema for Radiopharmaceutical Dosimetry—Standardization of Nomenclature. *J Nucl Med*. 2009;50:477-484.

90. Stabin MG. MIRDOSE: Personal Computer Software for Internal Dose Assessment in Nuclear Medicine. *J Nucl Med*. 1996;37:538-546.

91. Mattsson S, Johansson L, Leide Svegborn S, et al. Radiation Dose to Patients from Radiopharmaceuticals: a Compendium of Current Information Related to Frequently Used Substances. *Ann ICRP*. 2015;44:7-321.

92. Stabin MG, Emmons MA, Segars WP, Fernald MJ. Realistic reference adult and paediatric phantom series for internal and external dosimetry. *Radiat Prot Dosimetry*. 2012;149:56-59.

93. Carter LM, Camilo Ocampo Ramos J, Bolch WE, Lewis JS, Kesner AL. Technical Note: Patient-morphed mesh-type phantoms to support personalized nuclear medicine dosimetry — a proof of concept study. *Med Phys*. 2021;48:2018-2026.

94. Howard DM, Kearfott KJ, Wilderman SJ, Dewaraja YK. Comparison of I-131 Radioimmunotherapy Tumor Dosimetry: Unit Density Sphere Model Versus Patient-

Specific Monte Carlo Calculations. *Cancer Biother Radiopharm*. 2011;26:615.

95. Hobbs RF, Song H, Watchman CJ, et al. A bone marrow toxicity model for 223Ra alpha-emitter radiopharmaceutical therapy. *Phys Med Biol*. 2012;57:3207.

96. Hobbs RF, Song H, Huso DL, H Sundel M, Sgouros G. A nephron-based model of the kidneys for macro-to-micro α-particle dosimetry. *Phys Med Biol*. 2012;57:4403.

97. Adelstein SJ. Biophysical aspects of Auger processes: A review of the literature 1987--1991. United States: American Inst of Physics, Inc; 1992.

98. Bodei L, Kassis AI, Adelstein SJ, Mariani G. Radionuclide Therapy with Iodine-125 and Other Auger–Electron-Emitting Radionuclides: Experimental Models and Clinical Applications. *https://home.liebertpub.com/cbr*. 2004;18:861-877.

99. Seniwal B, Bernal MA, Fonseca TCF. Microdosimetric calculations for radionuclides emitting β and α particles and Auger electrons. *Appl Radiat Isot*. 2020;166:109302.

100. Graves SA, Hobbs RF. Dosimetry for Optimized, Personalized Radiopharmaceutical Therapy. *Semin Radiat Oncol*. 2021;31:37-44.

101. Agostinelli S, Allison J, Amako K, et al. Geant4—a simulation toolkit. *Nucl Instruments Methods Phys Res Sect A Accel Spectrometers, Detect Assoc Equip*. 2003;506:250-303.

102. Briesmeister JF. MCNP-A general Monte Carlo code for neutron and photon transport. *LA-7396-M*. 1986.

103. Kawrakow I. The EGSnrc code system, Monte Carlo simulation of electron and photon transport. *NRCC Rep Pirs-701*. 2001.

104. Kolbert KS, Sgouros G, Scott AM, et al. Implementation and evaluation of patient-specific three-dimensional internal dosimetry. *J Nucl Med*. 1997;38:301-308.

105. Tagesson M, Ljungberg M, Strand SE. The SIMDOS Monte Carlo code for conversion of activity distributions to absorbed dose and dose-rate distributions. In: Sixth International Radiopharmaceutical Dosimetry Symposium, Oak Ridge, TN: Oak Ridge Associated Universities. ; 1999:425-440.

106. Ljungberg M, Liu X, Strand SE. Dosing: A 3D voxel-based Monte Carlo program for absorbed dose calculations. In: Journal of Nuclear Medicine. Vol 42. SOC NUCLEAR MEDICINE INC 1850 SAMUEL MORSE DR, RESTON, VA 20190-5316 USA; 2001:243P-243P.

107. Yoriyaz H, Stabin MG, dos Santos A. Monte Carlo MCNP-4B-based absorbed dose distribution estimates for patient-specific dosimetry. *J Nucl Med*. 2001;42:662-9.

108. Lehmann J, Siantar CH, Wessol DE, et al. Monte Carlo treatment planning for molecular targeted radiotherapy within the MINERVA system. *Phys Med Biol*. 2005;50:947.

109. Chiavassa S, Bardiès M, Guiraud-Vitaux F, et al. OEDIPE: A Personalized Dosimetric Tool Associating Voxel-Based Models with MCNPX. *https://home.liebertpub.com/cbr*. 2005;20:325-332.

110. Dewaraja YK, Schipper MJ, Shen J, et al. Tumor-Absorbed Dose Predicts Progression-Free Survival Following (131)I-Tositumomab Radioimmunotherapy. *J Nucl Med*. 2014;55:1047-53.

111. Marcatili S, Pettinato C, Daniels S, et al. Development and validation of RAYDOSE: a Geant4-based application for molecular radiotherapy. *Phys Med Biol*. 2013;58:2491.

112. Grimes J, Uribe C, Celler A. JADA: A graphical user interface for comprehensive internal dose assessment in nuclear medicine. *Med Phys*. 2013;40:072501.

113. Lu CC, Lin HH, Chuang KS, et al. Development and validation of a fast voxel-based dose evaluation system in nuclear medicine. *Radiat Phys Chem*. 2014;104:355-359.

114. Kost SD, Dewaraja YK, Abramson RG, Stabin MG. VIDA: A Voxel-Based Dosimetry Method for Targeted Radionuclide Therapy Using Geant4. *https://home.liebertpub.com/cbr*. 2015;30:16-26.

115. Cross WG, Ing H, Freedman NO, Mainville J. Tables of beta-ray dose distributions in water, air and other media. 1982.

116. Sgouros G, Barest G, Thekkumthala J, et al. Treatment planning for internal radionuclide therapy: Three-dimensional dosimetry for nonuniformly distributed radionuclides. *J Nucl Med*. 1990;31:1884-1891.

117. Cross WG. Variation of beta dose attenuation in different media. *Phys Med Biol*. 1968;13:611-618.

118. Ahnesjö A. Collapsed cone convolution of radiant energy for photon dose calculation in heterogeneous media. *Med Phys*. 1989;16:577-592.

119. Sanchez-Garcia M, Gardin I, Lebtahi R, Dieudonné A. A new approach for dose calculation in targeted radionuclide therapy (TRT) based on collapsed cone superposition: validation with 90Y. *Phys Med Biol*. 2014;59:4769.

120. Grassi E, Fioroni F, Ferri V, et al. Quantitative comparison between the commercial software STRATOS® by Philips and a homemade software for voxel-dosimetry in radiopeptide therapy. *Phys Medica*. 2015;31:72-79.

121. Gardin I, Bouchet LG, Assié K, et al. Voxeldose: A Computer Program for 3-D Dose Calculation in Therapeutic Nuclear Medicine. *https://home.liebertpub.com/cbr*. 2004;18:109-115.

122. Kletting P, Schimmel S, Hänscheid H, et al. The NUKDOS software for treatment planning in molecular radiotherapy. *Z Med Phys*. 2015;25:264-274.

123. Grassi E, Valentina F, Fioroni F, et al. VoxelMed: A flexible software for voxel-dosimetry in radionuclide therapy. *J Nucl Med*. 2014;55:1497-1497.

124. Guy MJ, Flux GD, Papavasileiou P, Flower MA, Ott RJ. RMDP: A Dedicated Package For 131I SPECT Quantification, Registration and Patient-Specific Dosimetry. *https://home.liebertpub.com/cbr*. 2004;18:61-69.

125. Pasciak AS, Bourgeois AC, Bradley YC. A Comparison of Techniques for (90)Y PET/CT Image-Based Dosimetry Following Radioembolization with Resin Microspheres. *Front Oncol*. 2014;4.

126. Marcatili S. Multi-scale dosimetry for targeted radionuclide therapy optimisation. October 2015.

127. Therese Soderlund A, Chaal J, Tjio G, Totman JJ, Conti M, Townsend DW. Beyond 18F-

FDG: Characterization of PET/CT and PET/MR Scanners for a Comprehensive Set of Positron Emitters of Growing Application—18F, 11C, 89Zr, 124I, 68Ga, and 90Y. *J Nucl Med*. 2015;56:1285-1291.

128. Tran-Gia J, Salas-Ramirez M, Lassmann M. What You See Is Not What You Get: On the Accuracy of Voxel-Based Dosimetry in Molecular Radiotherapy. *J Nucl Med*. 2020;61:1178-1186.

129. Arsdale ED Van, Greenlaw RH. Formalized Immobilization and Localization in Radiotherapy. *https://doi.org/101148/993697*. 1971;99:697-698.

130. Goitein M, Busse J. Immobilization Error: Some Theoretical Considerations. *https://doi.org/101148/1172407*. 1975;117:407-412.

131. Marks JE, Haus AG. The effect of immobilisation on localisation error in the radiotherapy of head and neck cancer. *Clin Radiol*. 1976;27:175-177.

132. Xiao Y, Roncali E, Hobbs R, et al. Toward Individualized Voxel-Level Dosimetry for Radiopharmaceutical Therapy. *Int J Radiat Oncol*. 2021;109:902-904.

133. Jackson PA, Beauregard JM, Hofman MS, Kron T, Hogg A, Hicks RJ. An automated voxelized dosimetry tool for radionuclide therapy based on serial quantitative SPECT/CT imaging. *Med Phys*. 2013;40.

134. Jackson PA, Hofman MS, Hicks RJ, Scalzo M, Violet J. Radiation Dosimetry in 177Lu-PSMA-617 Therapy Using a Single Posttreatment SPECT/CT Scan: A Novel Methodology to Generate Time- and Tissue-Specific Dose Factors. *J Nucl Med*. 2020;61:1030-1036.

135. Pitiot A, Bardinet E, Thompson PM, Malandain G. Piecewise affine registration of biological images for volume reconstruction. *Med Image Anal*. 2006;10:465-483.

136. Ao ECI, Wu N-Y, Wang S-J, Song N, Mok GSP. Improved dosimetry for targeted radionuclide therapy using nonrigid registration on sequential SPECT images. *Med Phys*. 2015;42:1060-1070.

137. Pauwels S, Barone R, Walrand S, et al. Practical Dosimetry of Peptide Receptor Radionuclide Therapy with ⁹⁰Y-Labeled Somatostatin Analogs. *J Nucl Med*. 2005;46:92S LP-98S.

138. Ilan E, Sandström M, Wassberg C, et al. Dose Response of Pancreatic Neuroendocrine Tumors Treated with Peptide Receptor Radionuclide Therapy Using 177Lu-DOTATATE. *J Nucl Med*. 2015;56:177-182.

139. Cremonesi M, Ferrari ME, Bodei L, et al. Correlation of dose with toxicity and tumour response to 90Y- and 177Lu-PRRT provides the basis for optimization through individualized treatment planning. *Eur J Nucl Med Mol Imaging*. 2018;45:2426-2441.

140. Violet J, Jackson P, Ferdinandus J, et al. Dosimetry of 177Lu-PSMA-617 in Metastatic Castration-Resistant Prostate Cancer: Correlations Between Pretherapeutic Imaging and Whole-Body Tumor Dosimetry with Treatment Outcomes. *J Nucl Med*. 2019;60:517-523.

141. Kratochwil C, Fendler WP, Eiber M, et al. EANM procedure guidelines for radionuclide therapy with 177 Lu-labelled PSMA-ligands (177 Lu-PSMA-RLT). *Eur J Nucl Med Mol*

Imaging. 2019;46:2536-2544.

142. Kabasakal L, AbuQbeitah M, Aygün A, et al. Pre-therapeutic dosimetry of normal organs and tissues of (177)Lu-PSMA-617 prostate-specific membrane antigen (PSMA) inhibitor in patients with castration-resistant prostate cancer. *Eur J Nucl Med Mol Imaging*. 2015;42:1976-1983.

143. Delker A, Fendler WP, Kratochwil C, et al. Dosimetry for (177)Lu-DKFZ-PSMA-617: a new radiopharmaceutical for the treatment of metastatic prostate cancer. *Eur J Nucl Med Mol Imaging*. 2016;43:42-51.

144. Herrmann K, Bluemel C, Weineisen M, et al. Biodistribution and radiation dosimetry for a probe targeting prostate-specific membrane antigen for imaging and therapy. *J Nucl Med*. 2015;56:855-861.

145. Weineisen M, Schottelius M, Simecek J, et al. 68Ga- and 177Lu-Labeled PSMA I&T: Optimization of a PSMA-Targeted Theranostic Concept and First Proof-of-Concept Human Studies. *J Nucl Med*. 2015;56:1169-1176.

146. Dewaraja YK, Frey EC, Sgouros G, et al. MIRD pamphlet no. 23: Quantitative SPECT for patient-specific 3-dimensional dosimetry in internal radionuclide therapy. *J Nucl Med*. 2012;53:1310-1325.

147. Dewaraja YK, Ljungberg M, Green AJ, et al. MIRD pamphlet No. 24: Guidelines for quantitative 131I SPECT in dosimetry applications. *J Nucl Med*. 2013;54:2182-2188.

148. Ljungberg M, Celler A, Konijnenberg MW, Eckerman KF, Dewaraja YK, Sjögreen-Gleisner K. MIRD pamphlet no. 26: Joint EANM/MIRD guidelines for quantitative 177Lu SPECT applied for dosimetry of radiopharmaceutical therapy. *J Nucl Med*. 2016;57:151-162.

149. Sundlöv A, Sjögreen-Gleisner K. Peptide Receptor Radionuclide Therapy – Prospects for Personalised Treatment. *Clin Oncol*. 2021;33:92-97.

150. Cherry SR, Sorenson JA, Phelps ME. Physics in nuclear medicine. Elsevier/Saunders; 2012.

151. Badawi RD, Shi H, Hu P, et al. First Human Imaging Studies with the EXPLORER Total-Body PET Scanner*. *J Nucl Med*. 2019;60:299-303.

152. Levin CS, Hoffman EJ. Calculation of positron range and its effect on the fundamental limit of positron emission tomography system spatial resolution. *Phys Med Biol*. 1999;44:781-799.

153. Jødal L, Le Loirec C, Champion C. Positron range in PET imaging: non-conventional isotopes. *Phys Med Biol*. 2014;59:7419.

154. De Jong HWAM, Perk L, Visser GWM, Boellaard R, Van Dongen GAMS, Lammertsma AA. High resolution PET imaging characteristics of68Ga, 124i and89Zr compared to18F. *IEEE Nucl Sci Symp Conf Rec*. 2005;3:1624-1627.

155. Disselhorst JA, Brom M, Laverman P, et al. Image-quality assessment for several positron emitters using the NEMA NU 4-2008 standards in the Siemens Inveon small-animal PET scanner. *J Nucl Med*. 2010;51:610-617.

156. Abdul-Fatah SB, Zamburlini M, Halders SGEA, Brans B, Teule GJJ, Kemerink GJ. Identification of a shine-through artifact in the trachea with (124)I PET/CT. *J Nucl Med*. 2009;50:909-911.

157. Hoffman EJ, Huang SC, Phelps ME. Quantitation in positron emission computed tomography: 1. effect of object size. *J Comput Assist Tomogr*. 1979;3:299-308.

158. Kessler RM, Ellis JR, Eden M. Analysis of emission tomographic scan data: Limitations imposed by resolution and background. *J Comput Assist Tomogr*. 1984;8:514-522.

159. Jentzen W, Hobbs RF, Stahl A, Knust J, Sgouros G, Bockisch A. Pre-therapeutic 124I PET(/CT) dosimetry confirms low average absorbed doses per administered 131I activity to the salivary glands in radioiodine therapy of differentiated thyroid cancer. *Eur J Nucl Med Mol Imaging*. 2010;37:884-895.

160. Soret M, Bacharach SL, Buvat I. Partial-volume effect in PET tumor imaging. *J Nucl Med*. 2007;48:932-945.

161. Alavi A, Werner TJ, Høilund-Carlsen PF, Zaidi H. Correction for Partial Volume Effect Is a Must, Not a Luxury, to Fully Exploit the Potential of Quantitative PET Imaging in Clinical Oncology. *Mol Imaging Biol*. 2018;20.

162. Erlandsson K, Buvat I, Pretorius PH, Thomas BA, Hutton BF. A review of partial volume correction techniques for emission tomography and their applications in neurology, cardiology and oncology. *Phys Med Biol*. 2012;57.

163. Geworski L, Knoop BO, De Cabrejas ML, Knapp WH, Munz DL. Recovery correction for quantitation in emission tomography: a feasibility study. *Eur J Nucl Med 2000 272*. 2000;27:161-169.

164. Teo BK, Seo Y, Bacharach SL, et al. Partial-volume correction in PET: Validation of an iterative postreconstruction method with phantom and patient data. *J Nucl Med*. 2007;48:802-810.

165. Tohka J, Reilhac A. Deconvolution-based partial volume correction in Raclopride-PET and Monte Carlo comparison to MR-based method. *Neuroimage*. 2008;39:1570-1584.

166. Erlandsson K, Buvat I, Pretorius PH, Thomas BA, Hutton BF. A review of partial volume correction techniques for emission tomography and their applications in neurology, cardiology and oncology. *Phys Med Biol*. 2012;57:R119-R159.

167. Tran-Gia J, Salas-Ramirez M, Lassmann M. What You See Is Not What You Get - On the Accuracy of Voxel-Based Dosimetry in Molecular Radiotherapy. *J Nucl Med*. December 2019:jnumed.119.231480.

168. Barbee DL, Flynn RT, Holden JE, Nickles RJ, Jeraj R. A method for partial volume correction of PET-imaged tumor heterogeneity using expectation maximization with a spatially varying point spread function. *Phys Med Biol*. 2010;55:221-236.

169. Kirov AS, Piao JZ, Schmidtlein CR. Partial volume effect correction in PET using regularized iterative deconvolution with variance control based on local topology. *Phys Med Biol*. 2008;53:2577-2591.

170. Tohka J, Reilhac A. Deconvolution-based partial volume correction in Raclopride-PET

and Monte Carlo comparison to MR-based method. *Neuroimage*. 2008;39:1570-1584.

171. JC Y, MA F, S W. Improved quantification of radionuclide uptake using deconvolution and windowed subtraction techniques for scatter compensation in single photon emission computed tomography. *Med Phys*. 1990;17:1011-1022.

172. S W, AP L, RJ O, MO L, MA F. Constrained deconvolution of SPECT liver tomograms by direct digital image restoration. *Med Phys*. 1985;12:53-58.

173. Cysouw MCF, Golla SVS, Frings V, et al. Partial-volume correction in dynamic PET-CT: effect on tumor kinetic parameter estimation and validation of simplified metrics. *EJNMMI Res*. 2019;9:1-11.

174. Rizzo G, Castiglioni I, Russo G, et al. Using Deconvolution to Improve PET Spatial Resolution in OSEM Iterative Reconstruction. *Methods Inf Med*. 2018;46:231-235.

175. Jomaa H, Mabrouk R, Khlifa N. Partial volume effect correction in PET image using iterative deconvolution and shearlet transform. *2018 4th Int Conf Adv Technol Signal Image Process ATSIP 2018*. May 2018:1-6.

176. Raptis E, Parkes LM, Anton-Rodriguez JM, Carter SF, Herholz K, Matthews JC. Evaluation of the Benefit of Partial Volume Correction for High Resolution PET Scanners. *2019 IEEE Nucl Sci Symp Med Imaging Conf NSS/MIC 2019*. October 2019.

177. Lucy LB. An iterative technique for the rectification of observed distributions. Vol 79.; 1974.

178. Richardson WH. Bayesian-Based Iterative Method of Image Restoration*. *J Opt Soc Am*. 1972;62:55.

179. Dempster AP, Laird NM, Rubin DB. Maximum Likelihood from Incomplete Data Via the EM Algorithm. *J R Stat Soc Ser B*. 1977;39:1-22.

180. Eriksson D, Stigbrand T. Radiation-induced cell death mechanisms. *Tumor Biol*. 2010;31:363-372.

181. Vakifahmetoglu H, Olsson M, Zhivotovsky B. Death through a tragedy: Mitotic catastrophe. *Cell Death Differ*. 2008;15:1153-1162.

182. MOLE RH. Whole body irradiation; radiobiology or medicine? *Br J Radiol*. 1953;26:234-241.

183. Wennerberg E, Vanpouille-Box C, Bornstein S, Yamazaki T, Demaria S, Galluzzi L. Immune recognition of irradiated cancer cells. *Immunol Rev*. 2017;280:220-230.

184. Formenti SC, Demaria S. Combining radiotherapy and cancer immunotherapy: A paradigm shift. *J Natl Cancer Inst*. 2013;105:256-265.

185. Ngwa W, Irabor OC, Schoenfeld JD, Hesser J, Demaria S, Formenti SC. Using immunotherapy to boost the abscopal effect. *Nat Rev Cancer*. 2018;18:313-322.

186. Liu S-Z. Nonlinear Dose-Response Relationship in the Immune System following Exposure to Ionizing Radiation: Mechanisms and Implications. *Nonlinearity Biol Toxicol Med*. 2003;1:154014203908444.

187. Fowler JF. The linear-quadratic formula and progress in fractionated radiotherapy. *Br J*

Radiol. 1989;62:679-694.

188. Golden EB, Apetoh L. Radiotherapy and Immunogenic Cell Death. *Semin Radiat Oncol*. 2015;25:11-17.

189. Harding SM, Benci JL, Irianto J, Discher DE, Minn AJ, Greenberg RA. Mitotic progression following DNA damage enables pattern recognition within micronuclei. *Nature*. 2017;548:466.

190. Wang H, Hu S, Chen X, et al. cGAS is essential for the antitumor effect of immune checkpoint blockade. *Proc Natl Acad Sci U S A*. 2017;114:1637-1642.

191. Vanpouille-Box C, Alard A, Aryankalayil MJ, et al. DNA exonuclease Trex1 regulates radiotherapy-induced tumour immunogenicity. *Nat Commun*. 2017;8:15618.

192. Nakamura N, Kusunoki Y, Akiyama M. Radiosensitivity of CD4 or CD8 positive human T-lymphocytes by an in vitro colony formation assay. *Radiat Res*. 1990;123:224-227.

193. Liu R, Xiong S, Zhang L, Chu Y. Enhancement of antitumor immunity by low-dose total body irradiationis associated with selectively decreasing the proportion and number of T regulatorycells. *Cell Mol Immunol*. 2010;7:157.

194. Balogh A, Persa E, Bogdándi EN, et al. The effect of ionizing radiation on the homeostasis and functional integrity of murine splenic regulatory T cells. *Inflamm Res*. 2013;62:201-212.

195. Liu S, Sun X, Luo J, et al. Effects of radiation on T regulatory cells in normal states and cancer: mechanisms and clinical implications. *Am J Cancer Res*. 2015;5:3276.

196. Arina A, Beckett M, Fernandez C, et al. Tumor-reprogrammed resident T cells resist radiation to control tumors. *Nat Commun*. 2019;10.

197. Rodriguez-Ruiz ME, Garasa S, Rodriguez I, et al. Intercellular Adhesion Molecule-1 and Vascular Cell Adhesion Molecule Are Induced by Ionizing Radiation on Lymphatic Endothelium. *Int J Radiat Oncol*. 2017;97:389-400.

198. Ware JH, Sanzari J, Avery S, et al. Effects of Proton Radiation Dose, Dose Rate and Dose Fractionation on Hematopoietic Cells in Mice. *Radiat Res*. 2010;174:325.

199. Maks CJ, Wan XS, Ware JH, et al. Analysis of White Blood Cell Counts in Mice after Gamma- or Proton-Radiation Exposure. *Radiat Res*. 2011;176:170.

200. Conti M, Eriksson L. Physics of pure and non-pure positron emitters for PET: a review and a discussion. *EJNMMI Phys*. 2016;3:8.

201. Haraguchi M, Yamashiro S, Yamamoto A, et al. Isolation of GD3 synthase gene by expression cloning of GM3 alpha-2,8-sialyltransferase cDNA using anti-GD2 monoclonal antibody. *Proc Natl Acad Sci U S A*. 1994;91:10455.

202. LI P, M S, A K, et al. A syngeneic orthotopic murine model of pancreatic adenocarcinoma in the C57/BL6 mouse using the Panc02 and 6606PDA cell lines. *Eur Surg Res*. 2011;47:98-107.

203. Watson PA, Ellwood-Yen K, King JC, Wongvipat J, LeBeau MM, Sawyers CL. Context-Dependent Hormone-Refractory Progression Revealed through Characterization of a Novel Murine Prostate Cancer Cell Line. *Cancer Res*. 2005;65:11565-11571.

204. S R, K M, E B. The antiproliferative effect of kefir cell-free fraction on HuT-102 malignant T lymphocytes. *Clin Lymphoma Myeloma*. 2009;9 Suppl 3.

205. Knowles SM, Zettlitz KA, Tavaré R, et al. Quantitative ImmunoPET of Prostate Cancer Xenografts with 89 Zr-and 124 I-Labeled Anti-PSCA A11 Minibody. *J Nucl Med*. 2014;55:452-459.

206. Besemer AE, Yang YM, Grudzinski JJ, Hall LT, Bednarz BP. Development and validation of RAPID: a patient-specific monte carlo three-dimensional internal dosimetry platform. *Cancer Biother Radiopharm*. 2018;33:155-165.

207. Hauf S, Kuster M, Batič M, et al. Radioactive decays in Geant4. *IEEE Trans Nucl Sci*. 2013;60:2966-2983.

208. Bhat MR. Evaluated Nuclear Structure Data File (ENSDF). In: Springer, Berlin, Heidelberg; 1992:817-821.

209. AM A, CW S, S T, et al. Application and evaluation of a measured spatially variant system model for PET image reconstruction. *IEEE Trans Med Imaging*. 2010;29:938-949.

210. Alessio AM, Kinahan PE. Improved quantitation for PET/CT image reconstruction with system modeling and anatomical priors. *Med Phys*. 2006;33:4095-4103.

211. VY P, F K, C M, M C. Fully 3-D PET reconstruction with system matrix derived from point source measurements. *IEEE Trans Med Imaging*. 2006;25:907-921.

212. Chicheportiche A, Marciano R, Orevi M. Comparison of NEMA characterizations for Discovery MI and Discovery MI-DR TOF PET/CT systems at different sites and with other commercial PET/CT systems. *EJNMMI Phys*. 2020;7:4.

213. Berthon B, Marshall C, Edwards A, Evans M, Spezi E. Influence of cold walls on PET image quantification and volume segmentation: A phantom study. *Med Phys*. 2013;40:082505.

214. Munk OL, Tolbod LP, Hansen SB, Bogsrud T V. Point-spread function reconstructed PET images of sub-centimeter lesions are not quantitative. *EJNMMI Phys 2017 41*. 2017;4:1-12.

215. Roach PJ, Bailey DL, Schembri GP, Thomas PA. Transition from Planar to SPECT V/Q Scintigraphy: Rationale, Practicalities, and Challenges. *Semin Nucl Med*. 2010;40:397-407.

216. Gutte H, Mortensen J, Jensen CV, et al. Comparison of V/Q SPECT and planar V/Q lung scintigraphy in diagnosing acute pulmonary embolism. *Nucl Med Commun*. 2010;31:82-86.

217. Pitiot A, Malandain G, Bardinet E, Thompson PM. Piecewise Affine Registration of Biological Images. *Lect Notes Comput Sci (including Subser Lect Notes Artif Intell Lect Notes Bioinformatics)*. 2003;2717:91-101.

218. Boiangiu C-A, Dvornic A-I. Methods of Bitonal Image Conversion for Modern and Classic Documents.

219. Thirion JP. Image matching as a diffusion process: An analogy with Maxwell's demons. *Med Image Anal*. 1998;2:243-260.

220. T V, X P, A P, N A. Diffeomorphic demons: efficient non-parametric image registration. *Neuroimage*. 2009;45.

221. Vercauteren T, Pennec X, Perchant A, Ayache N. Non-parametric Diffeomorphic Image Registration with the Demons Algorithm. *Lect Notes Comput Sci (including Subser Lect Notes Artif Intell Lect Notes Bioinformatics)*. 2007;4792 LNCS:319-326.

222. Kadoya N, Nakajima Y, Saito M, et al. Multi-institutional Validation Study of Commercially Available Deformable Image Registration Software for Thoracic Images. *Int J Radiat Oncol*. 2016;96:422-431.

223. Dice LR. Measures of the Amount of Ecologic Association Between Species. *Ecology*. 1945;26:297-302.

224. Sørensen T. A method of establishing groups of equal amplitude in plant sociology based on similarity of species and its application to analyses of the vegetation on Danish commons. *K Danske Vidensk Selsk*. 1948;5:1-34.

225. Rockafellar, R. Tyrrell; Wets RJ-B. Variational Analysis.; 2005.

226. Birsan T, Tiba D. One Hundred Years Since the Introduction of the Set Distance by Dimitrie Pompeiu. *IFIP Int Fed Inf Process*. 2005;199:35-39.

227. Dubuisson M-P, Jain AK. A modified Hausdorff distance for object matching. December 2002:566-568.

228. KK B, S M, TR M, H L, ML K. Use of image registration and fusion algorithms and techniques in radiotherapy: Report of the AAPM Radiation Therapy Committee Task Group No. 132. *Med Phys*. 2017;44:e43-e76.

229. Matrosic CK, Hull J, Palmer B, Culberson W, Bednarz B. Deformable abdominal phantom for the validation of real-time image guidance and deformable dose accumulation. *J Appl Clin Med Phys*. 2019;20:122-133.

230. Heerden LE van, Visser J, Koedooder K, Rasch CR, Pieters BR, Bel A. Role of deformable image registration for delivered dose accumulation of adaptive external beam radiation therapy and brachytherapy in cervical cancer. *J Contemp Brachytherapy*. 2018;10:542.

231. Nag S, Bice W, DeWyngaert K, Prestidge B, Stock R, Yu Y. The american brachytherapy society recommendations for permanent prostate brachytherapy postimplant dosimetric analysis. *Int J Radiat Oncol*. 2000;46:221-230.

232. Jagodinsky JC, Harari PM, Morris ZS. The Promise of Combining Radiation Therapy with Immunotherapy. *Int J Radiat Oncol*. April 2020.

233. Veterinary cooperative oncology group – common terminology criteria for adverse events (VCOG-CTCAE) following chemotherapy or biological antineoplastic therapy in dogs and cats v1.1. *Vet Comp Oncol*. 2016;14:417-446.

234. Albertini MR, Yang RK, Ranheim EA, et al. Pilot trial of the hu14.18-IL2 immunocytokine in patients with completely resectable recurrent stage III or stage IV melanoma. *Cancer Immunol Immunother 2018 6710*. 2018;67:1647-1658.

235. Hank JA, Gan J, Ryu H, et al. Immunogenicity of the Hu14.18-IL2 Immunocytokine

Molecule in Adults With Melanoma and Children With Neuroblastoma. *Clin Cancer Res*. 2009;15:5923-5930.

236. SC H, SA S, RL D, et al. Potential to involve multiple effector cells with human recombinant interleukin-2 and antiganglioside monoclonal antibodies in a canine malignant melanoma immunotherapy model. *J Immunother Emphasis Tumor Immunol*. 1994;16:188-197.

237. Helfand SC, Soergel SA, MacWilliams PS, Hank JA, Sondel PM. Clinical and immunological effects of human recombinant interleukin-2 given by repetitive weekly infusion to normal dogs. *Cancer Immunol Immunother 1994 392*. 1994;39:84-92.

238. Yang RK, Kalogriopoulos NA, Rakhmilevich AL, et al. Intratumoral hu14.18–IL-2 (IC) Induces Local and Systemic Antitumor Effects That Involve Both Activated T and NK Cells As Well As Enhanced IC Retention. *J Immunol*. 2012;189:2656-2664.

239. K M, IR M, MM T, et al. Safety and feasibility of an in situ vaccination and immunomodulatory targeted radionuclide combination immuno-radiotherapy approach in a comparative (companion dog) setting. *PLoS One*. 2021;16.

240. Besemer AE, Grudzinski JJ, Weichert JP, Hall LT, Bednarz BP. Pretreatment CLR 124 positron emission tomography accurately predicts CLR 131 three-dimensional dosimetry in triple-negative breast cancer patient. *Cancer Biother Radiopharm*. October 2018:cbr.2018.2568.

241. Domouchtsidou A, Barsegian V, Mueller SP, et al. Impaired lymphocyte function in patients with hepatic malignancies after selective internal radiotherapy. *Cancer Immunol Immunother 2018 675*. 2018;67:843-853.

242. Barsegian V, Hueben C, Mueller SP, et al. Impairment of lymphocyte function following yttrium-90 DOTATOC therapy. *Cancer Immunol Immunother 2015 646*. 2015;64:755-764.

243. Denoyer D, Lobachevsky P, Jackson P, Thompson M, Martin OA, Hicks RJ. Analysis of 177Lu-DOTA-Octreotate Therapy–Induced DNA Damage in Peripheral Blood Lymphocytes of Patients with Neuroendocrine Tumors. *J Nucl Med*. 2015;56:505-511.

244. Durum SK, Gengozian N. The Comparative Radiosensitivity of T and B Lymphocytes. *Int J Radiat Biol Relat Stud Physics, Chem Med*. 2009;34:1-15.

245. Sgouros G, Jureidini IM, Scott AM, Graham MC, Larson SM, Scheinberg DA. Bone Marrow Dosimetry: Regional Variability of Marrow-Localizing Antibody. *J Nucl Med*. 1996;37:695-698.

246. Schwartz J, Humm JL, Divgi CR, Larson SM, O'Donoghue JA. Bone marrow dosimetry using 124I-PET. *J Nucl Med*. 2012;53:615-621.

247. Shah AP, Bolch WE, Rajon DA, Patton PW, Jokisch DW. A paired-image radiation transport model for skeletal dosimetry. *J Nucl Med*. 2005;46:344-353.

248. Ferrer L, Kraeber-Bodéré F, Bodet-Milin C, et al. Three methods assessing red marrow dosimetry in lymphoma patients treated with radioimmunotherapy. *Cancer*. 2010;116:1093-1100.

249. Shen S, Meredith RF, Duan J, et al. Improved prediction of myelotoxicity using a patient-specific imaging dose estimate for non-marrow-targeting 90Y-antibody therapy. *J Nucl Med*. 2002;43:1245-1253.

250. Siegel JA. Establishing a clinically meaningful predictive model of hematologic toxicity in nonmyeloablative targeted radiotherapy: Practical aspects and limitations of red marrow dosimetry. *Cancer Biother Radiopharm*. 2005;20:126-140.

251. Siegel, JA, Wessels, BW, Watson, EE, Stabin, MG, Vriesendorp, HM, Bradley, EW, Badger, CC, Brill, AB, Kwok, CS, Stickly, DR, Eckerman, KF, Fisher, DR, Buchsbaum, DJ & Order, SESiegel, JA, Wessels, BW, Watson, EE, Stabin, MG, Vriesendorp, HM, Bradley, EW, S. Bone marrow dosimetry and toxicity for radioimmunotherapy. *Antibody, Immunoconj Radiopharm*. 1990;3:213-234.

252. Lopez BP, Jordan DW, Kemp BJ, Kinahan PE, Schmidtlein CR, Mawlawi OR. PET/CT acceptance testing and quality assurance: Executive summary of AAPM Task Group 126 Report. *Med Phys*. 2021;48:e31-e35.

253. Vandenberghe S, Mikhaylova E, D'Hoe E, Mollet P, Karp JS. Recent developments in time-of-flight PET. *EJNMMI Phys 2016 31*. 2016;3:1-30.

254. Wang W, Hu Z, Gualtieri EE, et al. Systematic and distributed time-of-flight list mode PET reconstruction. *IEEE Nucl Sci Symp Conf Rec*. 2006;3:1715-1722.

255. Lubberink M, Herzog H. Quantitative imaging of 124I and 86Y with PET. *Eur J Nucl Med Mol Imaging*. 2011;38.

256. Conti M. State of the art and challenges of time-of-flight PET. *Phys Medica*. 2009;25:1-11.

257. Caribé PRRV, Koole M, D'Asseler Y, Deller TW, Van Laere K, Vandenberghe S. NEMA NU 2–2007 performance characteristics of GE Signa integrated PET/MR for different PET isotopes. *EJNMMI Phys*. 2019;6:1-13.

258. Braad PEN, Hansen SB, Thisgaard H, Høilund-Carlsen PF. PET imaging with the non-pure positron emitters: 55Co, 86Y and 124I. *Phys Med Biol*. 2015;60:3479-3497.

259. Cabanas ML, Yan C, Lalonde RJ, Heron DE, Huq MS. Which Dose Specification Should Be Used for NRG Radiation Therapy Trials: Dose-to-Medium or Dose-to-Water? *Pract Radiat Oncol*. 2020;10:e103-e110.

260. Kry SF, Lye J, Clark CH, et al. Report dose-to-medium in clinical trials where available; a consensus from the Global Harmonisation Group to maximize consistency. *Radiother Oncol*. 2021;159:106-111.